



Alexandria University
Faculty of Engineering
Computer and Systems Engineering Department
B.Sc. Graduation Project (2008/2009)

An Accurate Zero-Configuration Device-free Passive Localization System for Typical Wireless Environments

Supervised by

Prof. Dr. Mohamed Nazieh El-Derini
Dr. Moustafa Amin Youssef

Presented by

Ahmed Ibrahim Elerian
Ahmed Abdelkader Ramadan
Ahmed Essam Kosba
Mohammed Elsayed Abdelfattah

بِسْمِ اللَّهِ الرَّحْمَنِ الرَّحِيمِ

Acknowledgment

First of all, we thank Allah for all the progress we made through the project.

We would like to thank **Dr. Moustafa Youssef** for his kind supervision and guidance during the project. We would also like to thank **Prof. Dr. Mohamed Nazieh El-Derini** for his kind support.

Dedications

To my family for their continuous love, support and encouragement.

Ahmed I. El-Erian

To my parents.

Ahmed Abdelkader

To my parents and my brother who gave me all the possible support.

A Essam

To my parents and sisters who helped me to keep my dreams alive.

To my family and friends for their patience, understanding, and support.

M El-Sayed El-Sabagh

Contents

I	Introduction and Background	1
1	Introduction	2
1.1	Overview	2
1.2	Motivation	2
1.3	Problem Definition	3
1.4	Objectives	5
1.5	Methodology	6
1.6	Organization of the report	7
2	Background	8
2.1	Location Determination Systems	8
2.1.1	Fundamental approaches to localization	8
2.1.2	Device-based Active Localization	10
2.1.3	Device-free Passive Localization	10
2.2	Challenges: <i>DfP</i> Localization	11
2.3	Site Planning	13
2.3.1	AP Placement Techniques	13
2.3.2	Relation between AP positions and localization error	14
2.4	Electromagnetic Modeling	15
II	Tracking, Detection and Site Planning	16
3	Tracking	17
3.1	Problem Definition	17
3.2	Related Work	17
3.3	Proposed Algorithms	18
3.3.1	Deterministic Technique	19
3.3.2	Proababilistic Technique	19
3.4	Experimental Evaluation	20
3.4.1	Testbed and Environment	20

3.4.2	Evaluation Metrics	21
3.4.3	Performance Analysis	21
3.4.4	Conclusion	25
4	Detection	26
4.1	Problem Definition	26
4.2	Proposed Algorithms	26
4.2.1	Location-Zero Algorithm	27
4.2.2	Normalized Threshold Algorithm	27
4.3	Experimental Evaluation	28
4.3.1	Testbed and Environment	28
4.3.2	Evaluation Metrics	28
4.3.3	Performance Evaluation	30
4.3.4	Conclusion	34
5	Site Planning	35
5.1	Problem Definition	35
5.2	Hypothesis	35
5.3	Experimental Evaluation	36
5.3.1	APs and MPs Placement	36
5.3.2	Location Set Selection	36
5.3.3	Conclusion	40
III	Electromagnetic Propagation Modeling	43
6	Wave Propagation	44
6.1	Problem Definition and Modeling Concept	44
6.2	Basic Definitions	45
6.2.1	Electromagnetics Basics	45
6.2.2	Antenna Basics	46
6.3	Comparison of Ray Tracing Models	49
6.4	Rays Tessellation	50
6.5	Reception Sphere	53
6.6	Ray Tracing Algorithm	56
7	Propagation Models	58
7.1	Power Model and Path Loss	58
7.1.1	Path Power	58
7.1.2	Received Power	60
7.1.3	Path Loss	60

7.1.4	Polarization Loss	60
7.2	Electric Field Model	60
7.2.1	Initial electric field $E(0)$	61
7.2.2	Electric Field Propagation	61
7.2.3	Electric Field Reflection and Transmission for non-PEC surfaces	62
7.2.4	Polarization of the reflected and transmitted rays . . .	64
7.2.5	Amplitude of the reflected and transmitted fields . . .	64
7.2.6	Calculating of the received power (Power Density) . . .	66
8	Diffraction using the UTD	68
8.1	Why GTD/UTD	68
8.1.1	Integral Functions Method	68
8.1.2	Finite Difference Time Domain (FDTD)	69
8.1.3	Diffraction Theory	69
8.2	Wedge Diffraction	73
8.2.1	Diffraction Model	73
8.3	Human Shadowing	82
8.3.1	Geometrical Configuration	82
8.3.2	Reflection Off a Cylindrical Surface	83
8.3.3	Diffraction Off a Cylindrical Surface	87
9	Validation	90
9.1	Experiment Design	90
9.2	Validation Results	91
IV	The DFP System	93
10	The <i>DfP</i> System	94
10.1	System Architecture	94
10.1.1	High Level Components	94
10.1.2	Data Representation, Acquisition and Storage	95
10.1.3	Tracking Algorithms	96
10.1.4	Detection Algorithms	97
10.1.5	Test Architecture	98
10.1.6	RF Prediction	103
10.2	System Operation	104
10.2.1	Offline Phase	105
10.2.2	Online Phase	105

V	Conclusions and Future Work	106
11	Conclusions and Future Work	107
11.1	Conclusions	107
11.2	Future Work	108
VI	Appendices	110
A	IEEE 802.11	111
A.1	History of 802.11	111
A.2	802.11 WLANs	111
A.3	The Physical Layer	112
A.4	The MAC Layer	112
A.5	802.11x	113
A.5.1	a	113
A.5.2	b	113
A.5.3	c	113
A.5.4	d	113
A.5.5	e	113
A.5.6	f	113
A.5.7	g	114
A.5.8	h	114
A.5.9	i	114
B	Tracking Performance For Different Classifiers	115
B.1	Other Classifiers	115
B.2	Comparing All Classifiers	116
C	Spherical Coordinates	117
D	Edge Detection	119
E	Diffraction Around a Cylinder	121
F	Sampling of Signal Strength	124
F.1	Sampling Grid	124
F.2	Interpolating Across the Floor Area	125

List of Figures

1.1	Components of a typical <i>DfP</i> system.	4
3.1	Experiment 1 Layout	21
3.2	Distance Error CDF for Experiment 1 using cross-validation. .	23
3.3	90% Confidence Intervals of distance error for Experiment 1. .	23
3.4	The average distance error results of Experiment 1 for all APs and MPs combinations.	24
4.1	<i>Threshold</i> tuning for <i>MinCount</i> = 1.	31
4.2	<i>Threshold</i> tuning for <i>MinCount</i> = 2.	32
4.3	<i>Threshold</i> tuning for <i>MinCount</i> = 3.	32
4.4	<i>Threshold</i> tuning for <i>MinCount</i> = 4.	33
5.1	Layouts of the three experiments that were performed to study the site planning effect. Lines between APs and MPs represent the direct line-of-sight for the different streams.	37
5.2	Tracking performance under the three layouts shown in Figure 5.1.	38
5.3	Detection performance using Location-Zero algorithm under the three layouts shown in Figure 5.1.	39
5.4	Tracking performance under different location sets for the three layouts shown in Figure 5.1.	41
5.5	Detection performance using Location-Zero algorithm under different location sets for the three layouts shown in Figure 5.1.	42
6.1	Electromagnetic wave.	45
6.2	An example of a wavefront.	46
6.3	Linear polarization.	47
6.4	Source Ray Wavefront.	50
6.5	Icosahedron.	51
6.6	Tessellated Triangle.	52
6.7	Hexagonal Wavefront for interior vertices.	52

6.8	Abberation at the icosahedron vertices.	53
6.9	2D view of the reception sphere.	54
7.1	One possible signal path from TX to RX through different interactions; r_1 and r_2 are reflection coefficients, and t_1 is a transmission coefficient.	59
7.2	Geometry of reflection and transmission.	63
8.1	Wire grid model of a cylinder.	69
8.2	Geometrical Representation of Keller's Law of Diffraction. . .	70
8.3	Creation of an incident shadow boundary.	73
8.4	Creation of a reflected shadow boundary.	74
8.5	Different regions in the vicinity of a wedge.	74
8.6	Wedge with curved faces.	75
8.7	Cone of diffracted rays.	76
8.8	Edge-Fixed coordinate system.	77
8.9	Normal and tangential unit vectors on the o -face of a wedge .	78
8.10	Geometrical configuration of the human shadowing problem. .	82
8.11	Principal directions at the point of incidence.	86
8.12	Principal directions at the point of incidence of a cylindrical surface.	86
8.13	Diffraction by Sampling the Shadow Region in the Plane of Incidence.	87
9.1	Environment layout of the conducted experiment.	90
9.2	Signal received from AP1	91
9.3	Signal received from AP2	91
10.1	Main components of the <i>DfP</i> system.	95
10.2	Radio-map is used by all algorithms.	95
10.3	The different types of radio-map entries.	96
10.4	The implemented tracking algorithms i.e. trackers.	96
10.5	The implemented detection algorithms i.e. detectors.	97
10.6	Test Interfaces	98
10.7	Basic Test Classes	99
10.8	Sample Test Classes	100
10.9	Composite Test Classes	101
10.10	model.math associations.	103
10.11	Ray Tracer.	104
C.1	Spherical Coordinates.	117

E.1	Tangent points off a circle from an exterior point.	121
E.2	Plane of incidence is defined by O and n	122
E.3	Sampling the shadow region.	123
F.1	Sampling Grid of A Sample Floor Area.	125
F.2	Sampling, Packing, and Texture Mapping.	125
F.3	A Floor Model after Sampling.	126

List of Tables

3.1	Cross-Validation tracking results for Experiment 1	22
3.2	Results of the Kernel method under independent test sets collected for Experiment 1	25
4.1	Confusion Matrix	29
4.2	Location-Zero algorithm detection performance under cross-validation and independent test sets.	30
4.3	Normalized Threshold algorithm detection performance under cross-validation.	33
4.4	Normalized Threshold algorithm detection performance under independent test set.	33
5.1	Accuracy and F-measure the three layouts shown in Figure 5.1.	39
8.1	Comparison of electromagnetic modeling techniques.	72
9.1	Measured vs. Simulated Results	92
B.1	Cross-Validation tracking results for different classification algorithms for Experiment 1.	116

Part I

Introduction and Background

Chapter 1

Introduction

1.1 Overview

The ever increasing demand for mobile computing and connectivity together with the wide deployment of local-area wireless networks motivated a growing interest in context-aware services. In mobile computing scenarios, context-aware applications are more effective in relieving the users from the burden of introducing information that can be automatically derived from their current context e.g. the surrounding environment. The user location is of special interest as it is fundamental to many types of applications, like navigation systems and location based services.

Device-free Passive (*DfP*) localization [1] is a new concept in location determination in wireless environments where the user does not need to carry any device. *DfP* systems were shown to provide very accurate location information in a controlled wireless environment. However, many challenges are yet to be addressed before *DfP* systems can make it to the market. Our work aims at enhancing the accuracy of *DfP* systems in real environments and developing an automated solution for site planning and system configuration.

1.2 Motivation

Several location determination systems have been developed over the years, including the GPS [2] system, infrared-based [3] systems, RF-based [4] systems, Bluetooth-based [5] systems and cell phone localization [6] systems. All these systems share the requirement that the user must carry a device to perform the localization function. On the other hand, Ultra-wide band radar [7], computer vision [8] and physical contact [9] based systems do

not require a device to be attached to the user, but rely on specialized infrastructure with high installment costs, which makes them less appealing in practice.

The *DfP* concept is unique in relieving these constraints. First, it is device-free. This means that no device needs to be attached to the tracked entity. In addition, it is passive. This means that the tracked entity does not participate actively in the localization process. In other words, the system does all the work while the entity of interest does not have to be aware of that. Second, it works with already installed wireless communication networks without requiring any specialized hardware, which increases the value of the underlying network by extending its services to support the localization function besides and without affecting the original communication function.

The unique nature of *DfP* systems can be exploited in a variety of scenarios, both for the benefit of and against the entity being tracked. *DfP* can be used in security for low-cost surveillance and intrusion detection. It can also be used for home automation and entertainment applications like interactive display systems for museums and retail stores.

1.3 Problem Definition

The *DfP* concept was first introduced in [1] where the operation of the *DfP* system was described and methods for implementing its main functionalities were presented.

The *DfP* concept utilizes the fact that RF characteristics are functions of the surrounding environment. Changes in the received physical signals can be related to changes in the environment. Among these changes, we are interested in the movement of entities inside an area of interest. Humans in particular, considerably affect RF waves in the 2.4 GHz band, e.g. IEEE 802.11b/g, as it contains the resonant frequency of water which comprises a significant fraction of the human body.

Figure 1.1 gives an overview of a *DfP* system components. A *DfP* system consists of signal transmitters, for example access points (AP) of nominal WiFi deployments, monitoring points (MP), for example standard wireless sniffers, in addition to an application server (AS) for processing and initiating actions as needed. The *DfP* problem can be stated as: given an environment where wireless devices and wireless monitoring stations are installed, it is required to detect, track, and identify entities inside this environment. These entities may be any objects that can cause changes to the wireless propagation medium, such as people and furniture. We define these requirements as

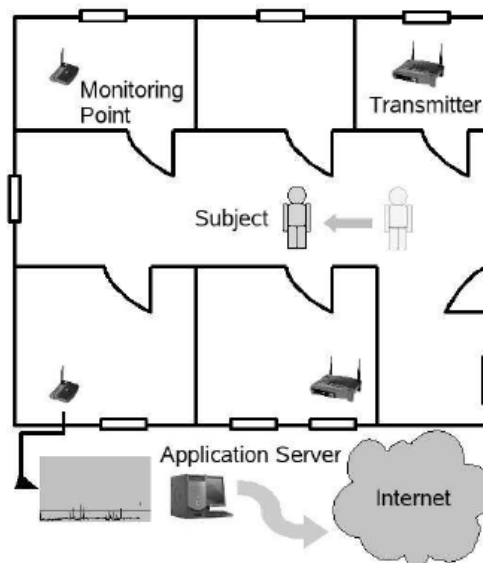


Figure 1.1: Components of a typical *DfP* system.

follows:

1. Detection

Identifying whether there are changes in an area of interest or not. This may also include the detection of the number of entities that caused the change. This may be used directly for intrusion detection or for controlling room temperature according to the number of humans inside the room.

2. Tracking

Identifying the position of entities as they move inside the area of interest. This information can be useful in responding to intruders or for controlling lights automatically as people move between rooms. It can also be used to initiate interactive services as users move around retail stores or museums.

3. Identification

Providing information about the identity of entities that caused the changes in the physical environment. This can be done at different levels of details, including the type of entity, its identity, its size, mass, shape, and composition.

1.4 Objectives

In this project, we are mainly interested in addressing a number of the inherent difficulties of *DfP* systems. It is necessary to overcome these difficulties before *DfP* systems can be utilized in practical applications with high performance demands or large scale deployments or both.

This is an overview of the objectives of this project. Each objective will be studied in subsequent chapters.

1. Enhancing Accuracy in Real Environments

Previous experiments with *DfP* systems were conducted in a highly controlled wireless environment to provide evidence of the feasibility of the new concept using simple algorithms. The challenge is to consider different algorithms for performing the localization function in real wireless environments like typical homes and offices.

2. Automatic System Configuration (Zero-Configuration)

The system needs to learn about the surrounding environment to be able to provide the localization services. Currently, *DfP* systems are configured manually, which is a time-consuming process that is impractical for large scale deployments. The challenge is to configure the system automatically using electromagnetic propagation models to predict RF behavior in the surrounding environment.

3. Site Planning

DfP systems depend deeply on the underlying wireless communication network. The exact configuration of this network has a major impact on the accuracy of the location information provided by the system. The challenge is to determine a certain configuration, i.e. the exact position of access points and monitoring points, which maximizes the system performance for a given environment.

4. Robustness

DfP systems are very suitable for intrusion detection and non-line of sight surveillance. The challenge is to handle adverse conditions, where an attacker attempts to compromise the system or when the environment is considerably changed from what the system was configured to work with.

1.5 Methodology

Location determination in wireless networks is an interdisciplinary field that requires a mixture of skills from different backgrounds. This is an outline of the different methods we incorporate in our work:

1. Machine learning

Location determination in wireless networks can be modeled as a machine learning problem. The system works in two phases, an offline training phase and an online operational phase. During the offline phase, the system learns about the relation between RF properties and the possible user locations inside the area of interest. When the system is operating in the online phase, it uses the information acquired during the offline phase together with the real time input from the monitoring points to infer the user location.

2. Electromagnetic modeling

In order to achieve automatic system configuration, the system needs to predict RF behavior inside the area of interest. We use a method that combines the theory of electromagnetic propagation with ray-tracing techniques to simulate RF propagation in 3D and retrieve the required system parameters.

3. Optimization

Selecting a system configuration that enhances the performance for a given environment is modeled as an optimization problem. Many possible system configurations need to be evaluated using an objective function to choose the best configuration. We study the underlying physical system to develop a suitable objective function then we use one of the known optimization algorithms from AI to search the solution space.

4. Scientific experimentation

Numerous data sets are required for validating the algorithms and testing the system. We have to design and conduct a number of experiments and analyze the acquired results using statistical measures.

1.6 Organization of the report

This report is divided into the following parts:

Part I: Introduction and Background - provides an overview of the project and introduces the subject of *DfP* localization and the relevant related field.

Part II: Tracking, Detection and Site Planning - discusses our work on these *DfP* functionalities. The proposed methods are explained and evaluated.

Part III: Electromagnetic Propagation Modeling - discusses our work on RF prediction. First, an elementary introduction to electromagnetic wave propagation is presented. This is followed by an overview of the different approaches to electromagnetic modeling. Then, we discuss our implementation of the RF predictor. Finally, we evaluate the quality of these predictions through a comparison to real measurements.

Part IV: The *DfP* System - describes the design and implementation of our *DfP* system.

Part V: Conclusions and Future Work - summarizes the conclusions of our work and highlights future work.

Chapter 2

Background

This chapter presents the background of this project. We present the relevant works available in the literature that helped throughout this project. We start with the rich field of location determination systems. Then we describe in more details the challenges related to the DfP concept. This is followed by a discussion of a number of site planning techniques. Finally, we introduce the exciting topic of electromagnetic modeling.

2.1 Location Determination Systems

This section provides an overview of the relevant existing work in the area of location determination. First, we distinguish between the major trends in wireless location determination. Then, we describe a variety of systems that tackled the localization problem. With the introduction of the *DfP* concept, we now refer to traditional location determination systems as device-based active localization systems. We highlight famous examples of these traditional systems then we outline a number of systems that considered the device-free passive localization problem.

2.1.1 Fundamental approaches to localization

There are three basic approaches to determining the user location using wireless signals [10]:

1. Trilateration

Requires at least three distinct estimates of the distance of a mobile

device with known locations, e.g. satellites in the case of GPS or access points in the case of WLANs.

2. Triangulation

Uses the direction or angle of arrival (DOA/AOA) of at least two distinct signals from known locations.

3. Location Fingerprinting

Refers to techniques that match the fingerprint of some characteristic of the signal that is location dependent. The fingerprints of different locations are stored and matched to measured fingerprints in real-time.

For the sake of completeness, we also mention the closest access point method. This method finds devices within the total coverage area of a single access point or base station. It is the simplest way to locate a mobile user but it is not accurate, in general. The method identifies only devices within the coverage area of a single access point, which can be quite large and for a typical indoor environment, may also include multiple rooms. This means that the location estimate granularity would be equal to the total coverage area of this base station. However, depending on the application requirements, this method might be good enough.

In a typical indoor environment, fading effects due to multipath propagation and shadowing from obstacles present a hostile propagation medium for RF waves [11]. Since most trilateration and triangulation techniques do not account for these effects they might not be very reliable. As a result, location fingerprinting is more favorable for indoor and WLAN systems. The remainder of this subsection will describe location fingerprinting in more details.

In typical WLANs, the received signal strength (RSS) is the most easily acquired signal attribute. Unfortunately, the RSS exhibits high temporal and spacial variations [11]. The big advantage of RSS-based techniques is that the existing infrastructure can be used to deploy a localization system almost without requiring any additional devices. It is far easier to obtain RSS information than multipath characteristics, the time of flight or angle of arrival, which require additional signal processing e.g. beam forming and DOA [7].

The acquired RSS information can be used in real-time to determine the distance between a transmitter and a receiver in two ways. The first method is to map the estimated path loss of the received signal to the distance it traveled from the transmitter to the receiver. With the knowledge of the RSS

from at least three transmitters, we can locate the receiver by trilateration. The second method is to capture the complex relation between RSS levels and the possible user location, i.e. RSS location fingerprints, through a *so-called* radio-map. This radio-map is constructed offline in a training phase and is used for matching the received signals to the stored fingerprints in the online operational phase.

2.1.2 Device-based Active Localization

Many location determination systems have been developed over the years. These systems include the GPS [2] system, ultrasonic-based [12] systems, infrared-based [3] systems, RF-based [4] systems, Bluetooth-based [5] systems and cell phone localization [6] systems. All these systems share the requirement that a device has to be attached to the tracked entity. In addition, some of these systems requires the device being tracked to participate actively in the localization process by running part of the localization algorithm.

2.1.3 Device-free Passive Localization

A number of systems have considered device-free passive localization, including radar based [7], computer vision based [8], physical contact based [9], and medical imaging based systems [13].

Using video cameras is a traditional method for video surveillance. Various algorithms were developed for detecting and tracking multiple objects in cluttered scenes using multiple synchronized cameras, for example [8].

Physical contact systems, like the Smart Floor system [9], track a person based on their contact with the environment i.e. system sensors. For example, pressure sensors can be used to detect the presence of a person over floor tiles.

Radar-based [7] systems are very accurate, yet very complex. In addition, as most of them operate at high frequencies, their coverage is rather limited.

Radio Tomographic Imaging [13] is a new technology that presents a linear model for using signal measurements to obtain images of moving objects. The system measures attenuation in transmitted signal rather than scattering and reflection and uses hundreds of data streams from sensor nodes. Since the system is based on LOS, its accuracy degrades as multipath components increase. A higher density of nodes is required to compensate for that.

2.2 Challenges: *DfP* Localization

DfP localization was first introduced in *MobiCom 2007* in a paper titled: *Challenges: Device-free Passive Localization* [1]. The paper also discussed several challenges related to the subject which required further research. In this section, we present the different research directions related to the *DfP* concept.

1. Identification Function

One of the main challenges that remains to be addressed is the entity identification problem. One possible solution for this challenge is to construct a *DfP-profile* for different entities that captures their characteristics and match signal measurements to one of the stored profiles. A similar idea have been proposed before for constructing human profiles using pressure sensors in The Smart Floor System [.]

2. Handling the Number of Entities

All the experiments performed so far considered a single person. When we turn our attention to handling multiple entities, we are faced by a new set of challenges. This may not be an issue for events that are spatially separated by a large distance, as the physical signal being monitored may not be affected by distant entities. On the other hand, handling changes within the same area is difficult because it requires separating the individual effects of each entity for processing.

3. Automatic Generation of the Passive Radio Map

Understanding the characteristics of RF signals and how they propagate is fundamental to the implementation of *DfP* systems. As a result, *DfP* researchers need to consider different models of RF propagation and how they reflect the actual propagation in an given environment. Predicting RF behavior inside the area of interest can reduce the manual labor required for installing a *DfP* system for that environment. This would be most needed for large scale deployments where the required amount of measurements is expected to be very large and would take a lot of time to perform manually.

4. Positioning of the APs and MPs

Another challenge is studying the effect of the positioning of APs and MPs on the accuracy of the *DfP* system for a given environment. Since the *DfP* system depends deeply on the measurements obtained from these sensors, the system can be configured to better serve the localization function by providing data that is more suitable for processing. This can lead to significant performance enhancements. The system configuration should also maintain the traditional desired performance measures of a typical wireless communication network such as coverage and delay spread.

5. Using Different Hardware

Implementing a *DfP* system requires studying the effect of changing system components hardware on the operating parameters. In addition, new APs are able to perform automatic power adjustment. It is interesting to study how this can be exploited in the design of a *DfP* system

6. Other Technologies

So far, *DfP* systems were only deployed in 802.11 environments. It is required to study the feasibility of this new technology with different RF frequency ranges. In addition, it is required to investigate the operation of *DfP* systems with other technologies such as ultrasonic and infrared.

7. Dynamic Changes in the Environment

The indoor radio channel exhibits considerable temporal and spacial variations. Also, there may be some sources of interference in the environment, such as microwave ovens, other WiFi devices, etc, that may affect the measured signal strength. Further research is needed to enable the *DfP* system to operate properly through these severe and varying conditions.

8. User Privacy

Although privacy may not fit the goals of the *DfP* system, the system can be configured to allow the user privacy under some conditions. For example, the system can only be enabled at night to detect intruders in the area of interest. This would preserve the privacy of the normal during the day time.

9. Robustness

It is vital to ensure the robustness of a *DfP* system under adverse conditions, where an attacker attempts to compromise the system. As security is one of the main target application areas of *DfP* systems, these scenarios have to be analyzed carefully and the *DfP* system has to be enhanced to maintain the desired performance under these conditions.

2.3 Site Planning

Many methods have been proposed to analyze both the indoor and outdoor signal coverage problem. This section highlights the relevant related work in optimal cellular and WLAN AP placement. Then, we describe two methods that accounted for the relation between AP positions and the performance of a given location determination technique.

2.3.1 AP Placement Techniques

A wireless AP placement technique for optimal indoor signal coverage is analyzed in [14]. The empirical Motley-Keenan indoor wave propagation model is used. In this model, the path loss depends on the type of walls, ceilings and floors. The cost function is the ratio of the points with higher path loss than a desired threshold. The optimal solutions is obtained by minimizing this cost function using genetic algorithms.

A method to deploy a large-scale indoor WLAN is proposed in [15]. In this method, the placement is constrained by allowing no coverage gaps, and no overlaps between APs operating on the same channel. First, the APs are placed by maximizing the signal coverage and minimizing the coverage gaps between. Next, a series of signal strength measurements are collected to determine the average coverage. Using these measurements, the signal coverage of each individual AP is modeled by a cylinder within which the coverage is considered optimal. Then, AP positions are adjusted using geometrical schemes to fill the area with the optimal coverage cylinders without leaving gaps. Later, other measurements are taken and the procedure is repeated until the solution is acceptable. Finally, frequency assignment is done by minimizing cochannel coverage overlap.

The DIRECT (DIviding RECTangles) search method presented in [16] aimed

at maximizing signal coverage. This method is a variation of the Nelder-Mead simplex method. In particular, this algorithm is useful when the cost function is non-differentiable because the gradient cannot be calculated.

The method introduced in [17] considers the deployment of a Wireless LAN with a good transmission rate over a 2-dimensional outdoors area e.g. a campus environment. The purpose is to design an objective function that measures the capability of a given AP configuration to provide a good signal coverage and uses a ray-tracing model for signal propagation. The objective function maximizes the average signal coverage and minimizes the number of points with the lowest signal strength. First a pruning step is applied, then by neighborhood search and simulated annealing are performed. The pruning algorithm starts with a configuration with a number of APs equal to the possible AP positions. Iteratively, the AP whose removal causes the smallest increase in the cost function is removed. The solution is obtained when the number of APs has been reduced to the desired one.

A combination of a greedy preprocessing algorithm followed by a genetic and a combinatorial scheme is described in [18] to maximize coverage. The Combination Algorithm for Total optimization (CAT) finds the optimal combinations of a specific group of APs that can be obtained given all the possible AP positions. As the number of combinations is too large they are divided into small groups and the algorithm proceeds by considering partial solutions before combining them. If the combined solution is not too large, the algorithm considers all possible combinations around that solution and the best combination is returned.

2.3.2 Relation between AP positions and localization error

Very few works considered the relation between AP positions and localization error. We present describe a method that relates localization errors with signal strength detection errors, hence suggesting localization-aware AP placement. Then, we describe a general model for user error and a method for selecting a configuration that minimizes that error.

Linear and multiple regression methods were introduced in [19] to estimate the signal strength model of an indoor wireless AP from sample data. The relationship between the standard deviation of localization error and signal strength error is analyzed for a few AP configurations. The analysis was limited to localization systems that operate by triangulation based on a

given signal propagation model.

A new approach to wireless AP placement was proposed in [20]. While other proposals focused on optimal coverage for the purposes of connectivity, the proposed method mixes coverage requirements with the enhancement of the quality of position estimates by a localization algorithm.

The paper presents a mathematical model of user localization error based on the variations in signal strength measurements. This model was designed to be independent from the actual localization technique, i.e. it only makes generic assumptions on the behavior of the localization algorithm employed.

The proposed error model is used by local search heuristic techniques, such as local search and simulated annealing. Near-optimal AP placements are computed for different optimization criteria like: positioning error minimization, signal coverage maximization or a mixture of both. These different criteria are not expected to be compatible. For example, maximizing signal coverage alone can lead to degradation of the average localization error, and vice versa.

2.4 Electromagnetic Modeling

“Propagation analysis provides a good initial estimate of the signal characteristics. The ability to accurately predict radio-propagation behavior for wireless personal communication systems is becoming crucial to system design. Since site measurements are costly, propagation models have been developed as a suitable, low-cost, and convenient alternative. Channel modeling is required to predict path loss and to characterize the impulse response of the propagating channel.” [21]

The existing models can be classified into two major classes: statistical models and deterministic models. Statistical models have the advantage of being computationally efficient for the complicated indoor environment. They are much less demanding of computational power than the deterministic models. Deterministic models include simple models like ray tracing and numerical analysis methods like finite-difference time domain (FDTD) method.

Part II

Tracking, Detection and Site Planning

Chapter 3

Tracking

In this chapter we discuss the tracking functionality of the *DfP* system and present the algorithms we use for tracking. In addition, we present an experimental study to evaluate these algorithms.

3.1 Problem Definition

Given that there is a person inside an area of interest. How to identify this person's location? More formally, given a radio map of a set of locations. What is the best algorithm to identify the tracked entity's location? Also, what are the factors that affect the accuracy of a *DfP* tracking system in a real environment? These problems are considered in the next sections.

3.2 Related Work

In WLAN device-based active localization, e.g. [4, 22] the system usually works in two phases: an offline training phase and an online operational phase. In the offline phase, the system learns about the relation between RF characteristics and the possible user locations. Then, during the online phase, the system infers the user location from the measurements of the received signals collected by the client device. Received Signal Strength Indication (RSSI) is the most commonly used signal characteristic as it is much easier to estimate by client devices than Time of Arrival (ToA) or Angle of Arrival (AoA) which require specialized hardware.

In a typical indoor environment, fading effects due to multipath propagation and shadowing from obstacles present a hostile propagation medium for RF waves [11]. Therefore, most WLAN based systems use a radio map to capture the relation between RSSI readings and user location. During the

offline phase, the system constructs an active radio map that stores information about the RSSI from each AP at a selected set of locations. Active radio maps are constructed either manually by taking RSSI samples from each AP at each location or automatically using signal propagation models to predict RSSI values at each location without taking any samples. This radio map is searched in the online phase to find the location that best matches the physical signals received by the client device.

During the online phase, there are two basic classes of techniques to perform this matching operation: deterministic techniques and probabilistic techniques. Deterministic techniques represent the RSSI by a scalar value, most commonly, the mean value, and use distance based methods to find the closest match. The *RADAR* [22] system for example, uses nearest neighbor search to estimate the user location. On the other hand, probabilistic techniques use the training information to estimate RSSI distributions at each location and use probabilistic methods to find the match with maximum likelihood. The *Horus* [4] system for example, uses a Bayesian inversion based search to infer the user location.

The fundamental difference between the *DfP* system and active localization systems is that the user carries no devices and all measurements are collected at monitoring points and forwarded to a centralized application server (AS) for processing. Therefore, the passive radio map is constructed during the offline phase by recording the effect of a person on the RSSI measurements for each stream, i.e. AP and MP pair, when a user is located at each possible location within the area of interest. Similarly, in the online phase, each MP periodically sends RSSI of each AP to the AS where the matching operation is performed.

3.3 Proposed Algorithms

Given an area of interest that has L locations and a set of n APs and m MPs, a person stands at each of the L locations for a period of time and RSSI values from each stream are processed and stored in a radio map. What the radio map stores exactly depends on the localization algorithm being used as explained in the next subsection.

Let k the number of streams equal $m \times n$. The AS periodically receives a k -dimensional signal strength vector \bar{s} , where \bar{s}_{ij} denotes the signal strength received at MP i from AP j . We propose deterministic and probabilistic techniques for estimating the user location:

3.3.1 Deterministic Technique

We consider the Nearest Neighbor in Signal Space (NNSS) algorithm. For this algorithm, the radio map stores the estimated mean for each stream readings at each location. The algorithm selects the radio map location l that minimizes the Euclidean distance between the received signal strength vector \bar{s} and the mean signal strength vector s'_l stored for that location.

$$\arg \min_l D(\bar{s}, s'_l) = \arg \min_l \sum_{i=1}^m \sum_{j=1}^n (\bar{s}_{ij} - s'_{l_{ij}})^2 \quad (3.1)$$

3.3.2 Probabilistic Technique

We consider a Bayesian inversion based inference algorithm. The algorithm selects the radio map location l that maximizes the probability $P(l/\bar{s})$ expressed as:

$$\begin{aligned} \arg \max_l P(l/\bar{s}) &= \arg \max_l P(\bar{s}/l) \cdot \frac{P(l)}{P(\bar{s})} \\ &= \arg \max_l P(\bar{s}/l) \cdot P(l) \end{aligned} \quad (3.2)$$

For a uniform user profile, i.e. all locations are equiprobable, Equation 3.2 reduces to:

$$\arg \max_l P(l/\bar{s}) = \arg \max_l P(\bar{s}/l) \quad (3.3)$$

Assuming all streams are independent:

$$P(\bar{s}/l) = \prod_{i=1}^m \prod_{j=1}^n P(\bar{s}_{ij}/l) \quad (3.4)$$

We consider two methods for estimating $P(\bar{s}_{ij}/l)$:

- A Parametric Approach: Here, we assume that RSSI values for each stream at each location follow a Gaussian Distribution. The radio map stores the estimated mean and variance parameters for each of these distributions.
- A Non-parametric Approach: We consider two methods for the non-parametric approach: a histogram method where the radio map stores the histograms of each stream at each location and a kernel method where the radio map stores an estimate for the density function of

RSSI values. Formally, given a random sample X_1, X_2, \dots, X_n from a density function f , the estimated density function is given by [23]:

$$\hat{f}(x) = \frac{1}{nh} \sum_{i=1}^n K\left(\frac{x - X_i}{h}\right) \quad (3.5)$$

where h is the smoothing parameter or the bandwidth and K is a kernel function that satisfies:

$$K(x) \geq 0 \text{ and } \int_{-\infty}^{\infty} K(x)dx = 1$$

We chose the Gaussian kernel because of its wide use:

$$K(x) = \frac{1}{\sqrt{2\pi}} e^{-\frac{1}{2}x^2} \quad (3.6)$$

and used Silverman's rule of thumb to estimate the optimal bandwidth:

$$\hat{h}_{rot} = 1.06\hat{\sigma}n^{-0.2} \quad (3.7)$$

where $\hat{\sigma}$ is an estimate for the standard deviation. This rule works fairly well for unimodal densities [23].

In the next section, we study the performance of the system using the above algorithms.

3.4 Experimental Evaluation

In this section, we describe the environment in which we conducted our experiments. We also present the metrics we used to evaluate the tracking accuracy of the system. Finally, we analyze the results of the experiment.

3.4.1 Testbed and Environment

Our experiments were conducted in a real 802.11b home environment that has two access points and two monitoring points. We used two Cisco Aironet 1130AG series access points and two HP laptops running Windows XP Professional each equipped with a D-Link AirPlus G+ DWL-650+ Wireless NIC. The experiment considered a single room covered with typical furniture. The experiment had six locations spaced one meter apart. Figure 3.1 shows the layout of the first experiment.

To construct the passive radio map, a person stood at each location and each MP recorded 300 samples taking one sample each second. The person kept standing in the same orientation for all locations. Without loss of generality, we assume a uniform user profile throughout the experiment.

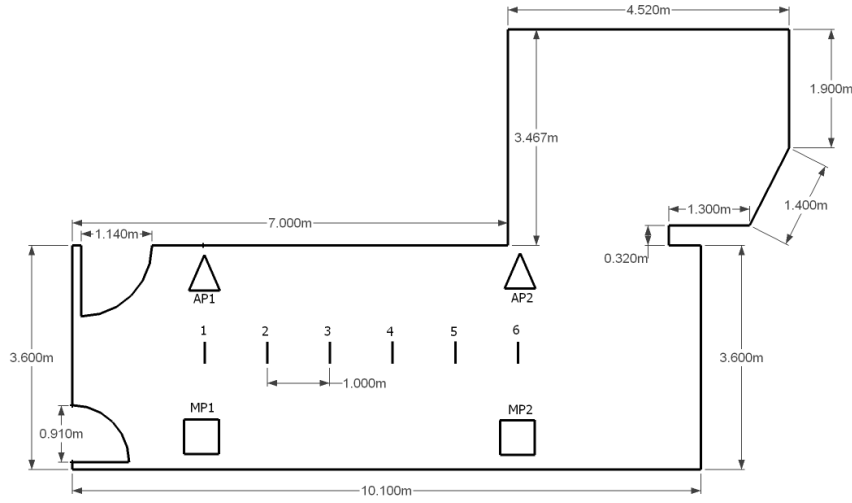


Figure 3.1: Experiment 1 Layout

3.4.2 Evaluation Metrics

We used two metrics for tracking analysis: the average distance error and the probability of error.

Average Distance Error

This metric represents the average distance error between the estimated and true user locations over all test cases.

Probability of Error

This metric represents the probability that the location estimated by the *DfP* tracking system does not match the true location. This is directly related to the number of times the system identified the correct location exactly.

3.4.3 Performance Analysis

We tested the tracking performance of our system using two techniques: cross-validation and independent test sets.

Cross-Validation

In order to perform our analysis, we used 10-times 10-fold cross-validation: The training data set is divided randomly into ten subsets. Then, each single

Algorithm	Average Distance Error	Error Probability
Gaussian Distribution	0.201m	0.0835
Histogram	0.176m	0.0727
Gaussian Kernel	0.175m	0.0723
Deterministic	0.214m	0.0874

Table 3.1: Cross-Validation tracking results for Experiment 1

subset is selected to act as the testing data, and the other nine subsets are used for training the system. This process is repeated ten times. Finally, the results of all tests are averaged. This approach was recommended in [24] and [25].

Accuracy: Figure 3.2 shows the distance error CDF of the four algorithms using cross-validation. Table 3.1 summarizes the results. The results show that probabilistic techniques perform better than the deterministic one. Figure 3.3 gives the 90% confidence intervals for the average distance error of the four algorithms. The figure shows that the Gaussian kernel and histogram methods are almost equivalent and they both are better than the Gaussian distribution method and the deterministic algorithm. The figure also shows that the confidence intervals of the Gaussian distribution and the deterministic algorithm are overlapping. A paired- t significance test shows that the Gaussian distribution method is statistically significantly better than the deterministic algorithm. Therefore, we can conclude that probabilistic algorithms perform better than the deterministic one. In addition, the non-parametric techniques perform better than the parametric one. This can be explained as the non-parametric estimation attempts to find an estimate for the density function of the signal distribution, whereas the parametric technique assumes that the signal strength follows a specific distribution. This can lead to higher errors especially, if the original signal distribution deviates from the assumed one.

Number of streams: To study the effect of the number of streams on the accuracy of the system, we tested all possible combinations of APs and MPs. Figure 3.4 shows the average distance error for these combinations. It can be noted that as the number of streams is increased (either by the addition of either MPs or APs), the system performs better. Specific selection of APs and MPs positioning directly affects the system performance, as we study in more details in Chapter 5.

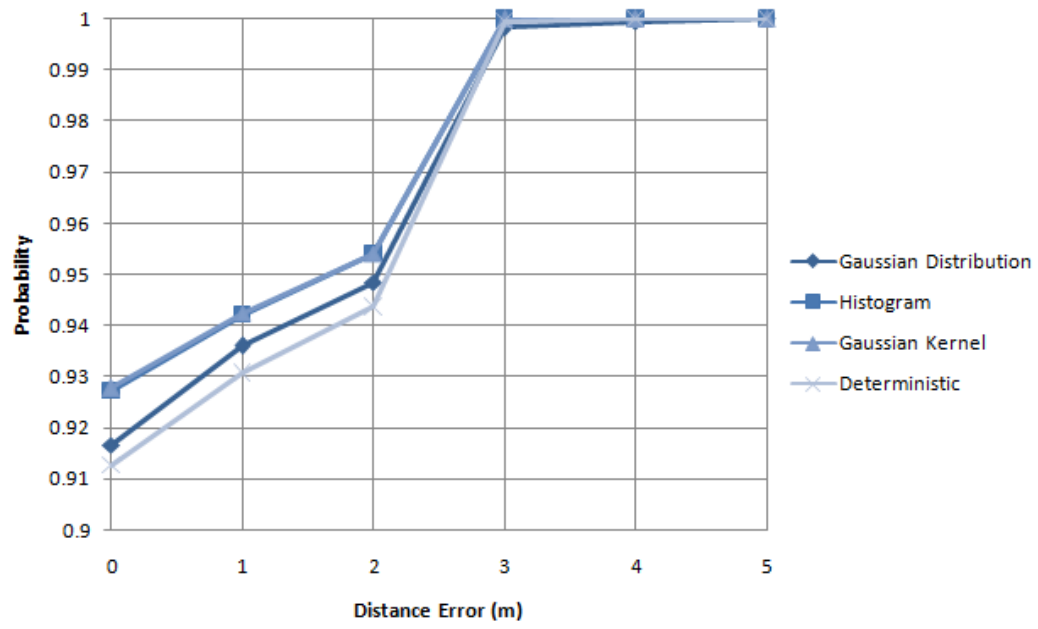


Figure 3.2: Distance Error CDF for Experiment 1 using cross-validation.

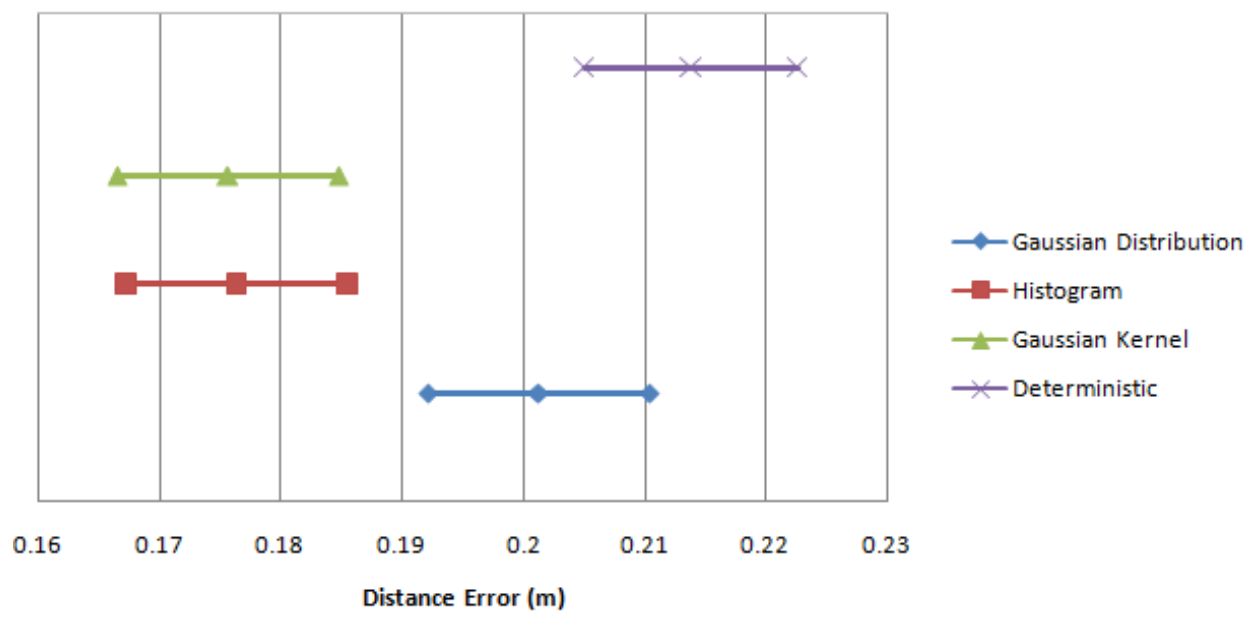


Figure 3.3: 90% Confidence Intervals of distance error for Experiment 1.

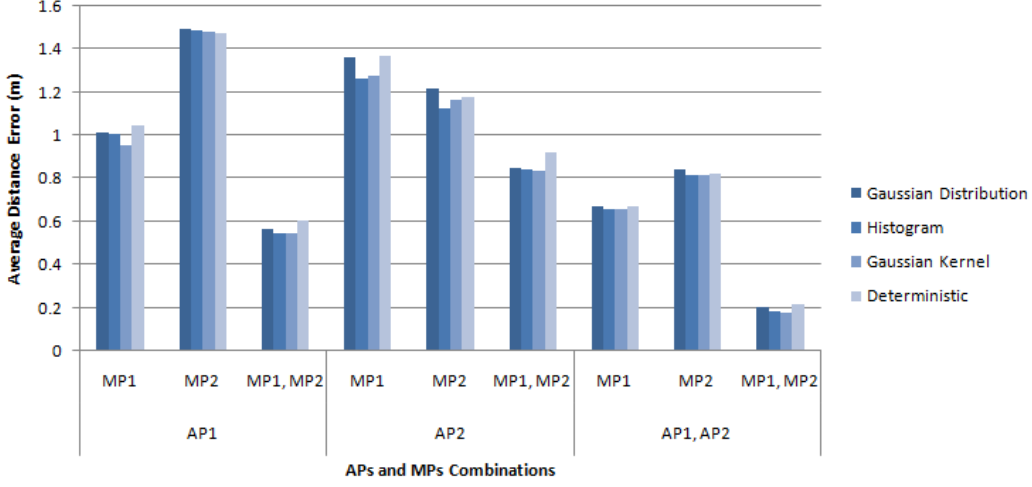


Figure 3.4: The average distance error results of Experiment 1 for all APs and MPs combinations.

Independent Test Sets

To better evaluate the accuracy of the system, we tested the system using independent test sets that consider the time factor and user orientation. Table 3.2 shows the data sets collected and the results using the Gaussian Kernel method. We also compare the results to that of a random location selection method that returns one of the radio map locations randomly as a baseline for comparison. Each data set contains 60 samples per location taken with a rate of one sample per second. The goal of this study is to identify the factors that affect the practical accuracy of the system.

The results show that, as expected, the cross-validation results overestimate the actual accuracy of a system, since they are extracted from the same training data. Changing the user orientation or the time the system is used reduces the accuracy of the system. This is expected as the environment may have changed significantly. In both cases, the system accuracy is significantly better than that of a random selection method (more than 3.3 times better in the worst case).

Compared to the results in a highly controlled environment [1], the performance of the *DfP* system degrades due to the noisy channel. However, the proposed techniques' performance, with a worst case average distance error of 0.586m is still suitable for accurate tracking of the intruders.

Test set	Time	User state	Average distance error	Probability of error
Cross-Validation	Same time	Same orientation	0.175m	0.0723
Set 1	Different time	Same orientation	0.358m	0.252
Set 2	Different time	Different orientation	0.586m	0.328
Random Location Selector	N/A	N/A	1.94m	0.833

Table 3.2: Results of the Kernel method under independent test sets collected for Experiment 1

3.4.4 Conclusion

Through the experimental study, the results showed that the probabilistic techniques performed better than the deterministic one. They also showed that the non-parametric probabilistic techniques performed better than the parametric one. We have identified some of the main challenges against the accuracy of *DfP* systems in real environments like temporal variation and user orientation. A possible solution to temporal variation may be to construct a radio map for each different time of a day. Another solution is to estimate the shift in signal strength distribution. We will consider finding solutions to these problems in future work. Another important challenge is site planning. In Chapter 5 we will discuss how the positioning of APs and MPs affects the accuracy of a *DfP* system.

Chapter 4

Detection

In Chapter 3 we considered the problem of tracking a single person inside an area of interest given that there is someone inside that area. In this chapter, we develop and evaluate two algorithms for *DfP* detection inside an area of interest.

4.1 Problem Definition

Given an area of interest, the problem is how to detect that a single person is in that area. Another issue is how we should define the nature of the problem. Will it be better to consider it as a classification problem? Or, will it be more accurate to put some constraints on the results returned by the tracking algorithm? In the next sections, we present and evaluate two algorithms for the described approaches.

4.2 Proposed Algorithms

In this section, we present the two algorithms we use for detection inside a *DfP* environment. As described above, one approach is to consider the problem as a classification problem. This approach is used in the first algorithm. Another approach is to put some constraints on the location returned by the tracking system. This approach is used in the second algorithm. We use the tracking algorithms described in Section 3.3 to aid in performing the detection functionality.

4.2.1 Location-Zero Algorithm

In this algorithm, we consider the silence state (when there is no one in the area) as a location in the radio map. We denote this location as Location-Zero. This location has a prior probability P_0 that can be set according to the nature of the application. For example, the prior probability of silence in a smart home application is lower than the one in an intrusion detection system.

To use this algorithm, in the offline phase, samples are recorded when there is no one in the area of interest. In the online phase, we apply any of the probabilistic algorithms described in Section 3.3. If the output is Location-Zero, then nothing is detected. In Section 4.3 we will evaluate the algorithm using the Histogram non-parametric probabilistic approach.

Drawbacks

There are two main drawbacks for this algorithm. The first is the issue of setting the values of the prior probabilities so that they suit an application. The second is when the number of locations gets higher, the system may be biased to the silence state because of the prior probabilities.

4.2.2 Normalized Threshold Algorithm

To avoid the problem of prior probabilities described in the previous section, we develop an algorithm that does not consider the silence state as a location in the radio map. This algorithm acts as a filter or a check point before raising an alarm that a person is in a specific location.

The algorithm is based on the intuition that the location returned by the tracking algorithm must be abnormal with respect to other locations. The algorithm input is the probabilities $P(\bar{s}/l)$ obtained in Section 3.3 besides two parameters *MinCount* and *Threshold*. The algorithm works as follows:

- Select the location l_{max} that maximizes the probability product as done in Section 3.3.
- Before raising the alarm, do the following check:
 - For each stream \bar{s}_{ij} , normalize the probabilities $P(\bar{s}_{ij}/l_k)$, where k ranges from 1 to the number of locations.
 - Let C the number of streams \bar{s}_{ij} such that $P(\bar{s}_{ij}/l_{max}) \geq Threshold$.
 - If $(C \geq MinCount)$ then raise alarm, else ignore.

The algorithm requires the selection of *MinCount* and *Threshold* values. This is done through a tuning phase that is performed before operation. The tuning phase aims at obtaining the least False Positives (FP) and False Negatives (FN) rates such that their values are equal. An example of a tuning process is presented in Section 4.3. It should be stated that the tuning phase process is considered one of the drawbacks of the algorithm because of its overhead.

Drawbacks

There are two main drawbacks for this algorithm. The first is the overhead of the tuning phase. The second is that the temporal variation affects the accuracy of the detection system especially when the *MinCount* value is small. This will be shown in detail in the next section.

4.3 Experimental Evaluation

In this section, we describe the environment in which we conducted our experiments. We also present the metrics we used to evaluate the detection performance of the system. Finally, we analyze the results of the experiment.

4.3.1 Testbed and Environment

We use the same testbed and environment described in Section 3.4.1. The layout is shown in Figure 3.1. The passive radio map is constructed the same way as done for tracking except that another set of samples is collected when there is no one in the area to test the detection capability.

4.3.2 Evaluation Metrics

We used many metrics to evaluate the detection performance of our *DfP* system. To calculate the metrics, we construct a confusion matrix that shows the actual and predicted classifications. Table 4.1 shows the confusion matrix. We refer the case in which there is someone in the area as *Positive* and otherwise as *Negative*.

One of the main assumptions in our analysis is that the probability of the positive state equals the probability of negative state. The reason behind this assumption is that we wanted to provide a *general* analysis. This assumption can be appropriate for many applications like smart home. However, in an intrusion-detection system, the assumption may not be appropriate enough

	Predicted Positive	Predicted Negative
Actual Positive	tp	fn
Actual Negative	fp	tn

Table 4.1: Confusion Matrix

as the values of the prior probabilities in the case of intrusion-detection are site specific.

The metrics we use for evaluating the detection performance are:

False Positives and False Negatives Rates

False Positives (FP) refers to the number of cases in which the system raises alarm when there is no one inside the area of interest. False Negatives (FN) refers to the number of cases in which the system does not raise alarm when there is someone inside the area of interest. The FP and FN rates can be obtained by:

$$\text{FP Rate} = \frac{fp}{tn + fp} \quad (4.1)$$

$$\text{FN Rate} = \frac{fn}{tp + fn} \quad (4.2)$$

Accuracy

This metric represents the proportion of the number of successful predictions of the system. It can be obtained by the following equation:

$$\text{Accuracy} = \frac{tp + tn}{tp + fn + tn + fp} \quad (4.3)$$

F-measure

This metric is used to measure the effectiveness of the detection system. It is calculated using *precision* and *recall* using the following equations:

$$\text{precision} = \frac{tp}{tp + fp} \quad (4.4)$$

$$\text{recall} = \frac{tp}{tp + fn} \quad (4.5)$$

$$F = \frac{2 \cdot \text{precision} \cdot \text{recall}}{\text{precision} + \text{recall}} \quad (4.6)$$

	Cross-Validation	Independent Test Set
FP Rate	2.9%	31.66%
FN Rate	2.8%	8.33%
Accuracy	97%	80 %
Precision	0.97	0.743
Recall	0.97	0.917
F-measure	0.97	0.82

Table 4.2: Location-Zero algorithm detection performance under cross-validation and independent test sets.

4.3.3 Performance Evaluation

The detection performance is evaluated with the same approaches used in Section 3.4.3. We will evaluate both the Location-Zero and Normalized Threshold algorithms using 10-times repeated 10-fold cross-validation and independent test sets. The results are obtained using the Histogram tracking algorithm described in Section 3.3.

Location-Zero Algorithm Performance

Table 4.2 shows the performance of the Location-Zero algorithm under cross-validation and independent test sets. The results show that in the optimal cases (cross-validation case), the system accuracy is 97% and f-measure is 0.97 which is high. Considering the independent test set results, it can be observed that the system performance degraded especially the FP rate and precision. However, the system accuracy is still higher than a random detection algorithm with an accuracy of 0.5.

Normalized Threshold Algorithm Performance

As stated in Section 4.2.2, the Normalized Threshold algorithm must have a parameter tuning phase before operation. We will describe our method for tuning the parameters *MinCount* and *Threshold*, then we will evaluate the performance of the algorithm using the obtained parameters.

Parameter Tuning: The parameter tuning method we propose aims at obtaining the least FP and FN rates such that FP rate equals FN rate. Figures 4.1 to 4.4 shows the parameters tuning phase done in our experiments. The parameter *MinCount* in our experiment is an integer that ranges from 1 to 4 (the number of streams) whereas the threshold can have any real value on the standard normal axis. The parameters are tuned using the training data

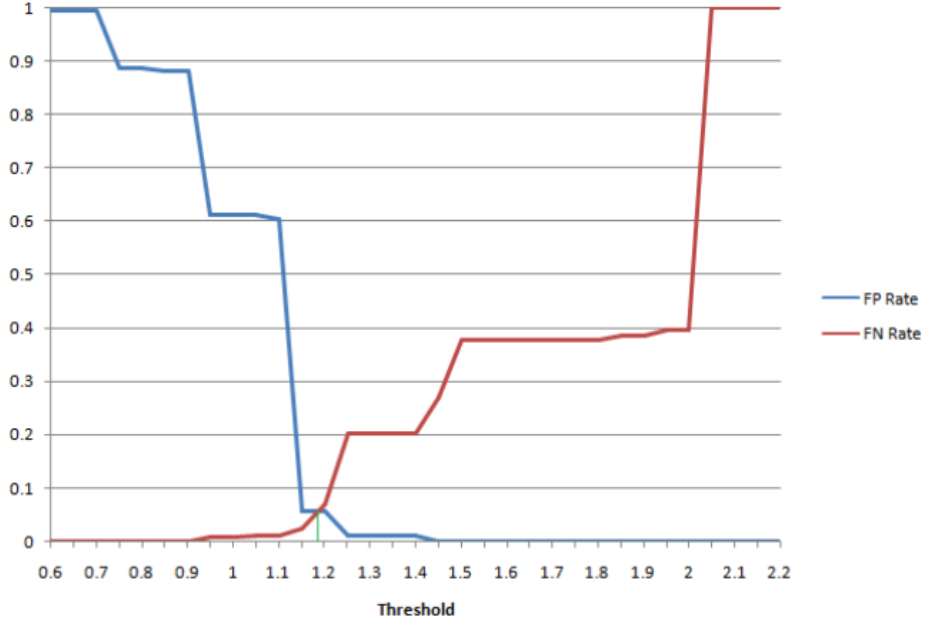


Figure 4.1: *Threshold* tuning for *MinCount* = 1.

acquired in the offline phase. As stated before, the Normalized Threshold algorithm avoids considering the silence state as a class in the radio map.

For example let us consider when *MinCount* equals 1, the threshold selected is the value at which the FP and FN rates intersect. This is to try as much as possible not to provide fair results between sensitivity and specificity. Further observation of the figures shows that as the *Threshold* parameter increases, the FP rate decreases and the FN rate increases. That is because when the *Threshold* parameter increases, it puts more constraints against the system to raise an alarm. In addition, when the *MinCount* increases, it can be observed that the *Threshold* of the intersection point decreases.

Evaluation: We evaluate the performance of the Normalized Threshold algorithm using the same procedure described before. Table 4.3 shows the cross-validation results for the Normalized Threshold algorithm using the parameters obtained in the tuning phase. In addition, the best results are obtained when *MinCount* equals 4 and *Threshold* equals -0.687. Table 4.4 shows the results under an independent test set. It can be shown that the system performance is much affected especially when *MinCount* is 1. Note that the best independent test results are obtained *MinCount* equals 4 and *Threshold* equals -0.687.

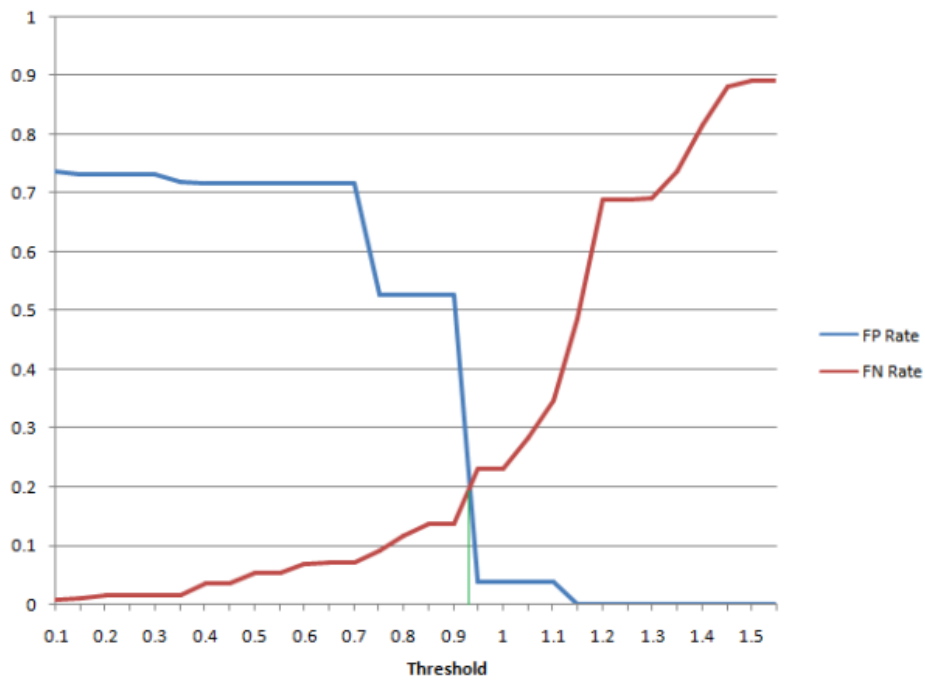


Figure 4.2: *Threshold* tuning for $MinCount = 2$.

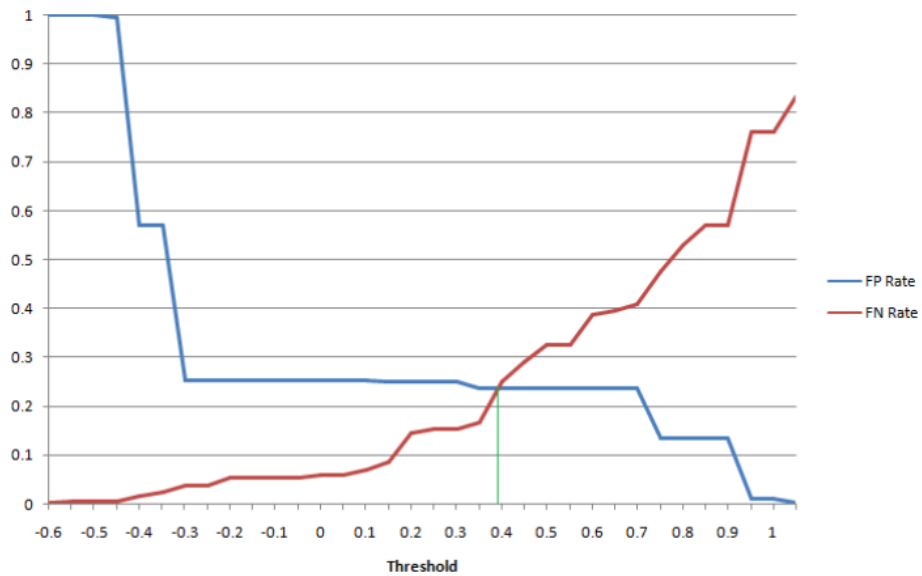
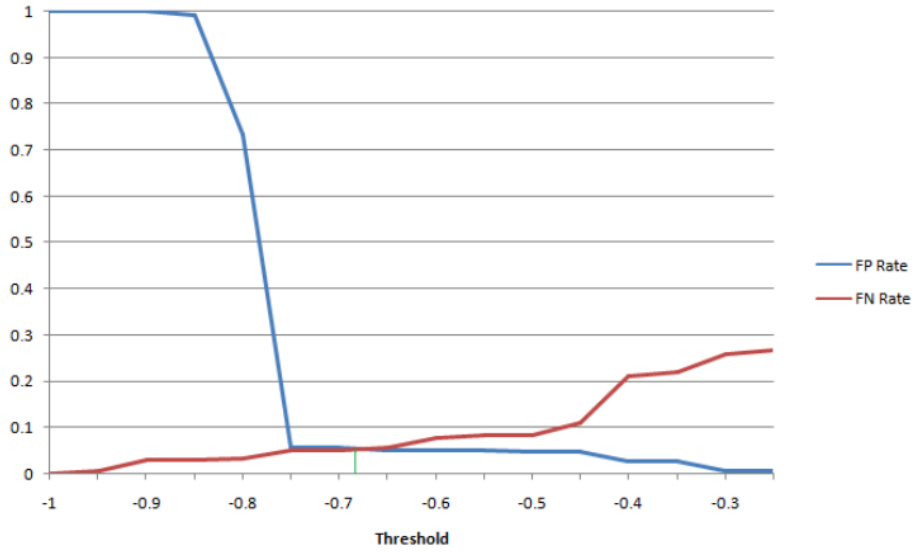


Figure 4.3: *Threshold* tuning for $MinCount = 3$.

Figure 4.4: *Threshold* tuning for $MinCount = 4$.

$(MinCount, Threshold)$	(1,1.175)	(2,0.936)	(3,0.398)	(4,-0.687)
FP Rate	8.3%	27%	26%	6%
FN Rate	4.5%	20%	22%	6.3%
Accuracy	93.6%	76.5%	76%	93.85%
Precision	0.92	0.75	0.75	0.94
Recall	0.955	0.8	0.78	0.937
F-measure	0.937	0.77	0.76	0.9385

Table 4.3: Normalized Threshold algorithm detection performance under cross-validation.

$(MinCount, Threshold)$	(1,1.175)	(2,0.936)	(3,0.398)	(4,-0.687)
FP Rate	75%	26%	8.3%	25%
FN Rate	13.3%	45%	62.5%	13.3%
Accuracy	56%	64%	64.6%	81%
Precision	0.53	0.72	0.82	0.776
Recall	0.867	0.55	0.375	0.867
F-measure	0.66	0.62	0.514	0.82

Table 4.4: Normalized Threshold algorithm detection performance under independent test set.

4.3.4 Conclusion

Comparing the results obtained by the Location-Zero algorithm with the best results obtained by the Normalized Threshold algorithm, it can be shown that Location-Zero algorithm performed better in the cross-validation case, however in the case of an independent test set, both algorithms achieved about 80% accuracy. The only difference is in the rates of FP and FN. The FP rate is higher in the Location-Zero algorithm whereas the FN rate is higher in the Normalized Threshold algorithm. However, the two rates are closer to each other when using the Normalized Threshold algorithm.

Chapter 5

Site Planning

In this chapter, we study the effect of site planning on the *DfP* system performance. First, we define the problem and present a hypothesis about APs and MPs placement in *DfP* environments to get higher performance, then, we validate the hypothesis through an experimental study.

5.1 Problem Definition

The problem of site planning involves two main aspects: The first is how to place the APs and MPs to enhance the performance of the *DfP* system. The second is how to select radio map locations for a given placement so as to get the best accuracy of the system. The next section presents a hypothesis about site planning in *DfP* environments.

5.2 Hypothesis

DfP systems depend mainly on the effect of human presense on signal strength. Therefore, in order to improve the accuracy of a *DfP* system, the human effect on the signal strength received at the monitoring points should be maximized. This can be achieved by selecting layouts in which the lines of sight between the APs and MPs are affected directly. In addition, radio map locations should be selected to vary the human effect on the monitoring streams to better discriminate between locations.

Our hypothesis utilizes the fact that the system functionalities are implemented by classification algorithms. Therefore, the better we provide discriminating features, the better the classifiers will be. In the *DfP* system, the classes are represented by locations and features are represented by streams. Therefore, each location must provide some unique effect on the

streams so as to be able to find a good mechanism to identify the tracked entity's location.

5.3 Experimental Evaluation

In this section, we validate the above hypothesis through experiments. We show how site planning affects the accuracy of both tracking and detection: First, We will study the effect of different placements for APs and MPs, then we will study the effect of radio map location set selection.

5.3.1 APs and MPs Placement

In addition to the layout tested in the previous chapters, we performed two additional experiments to study the effect of APs and MPs placement on the accuracy of the system. Each experiment had a different placement of two access points and two monitoring points. Figure 5.1 shows the three layouts we considered. We used 10-times 10-fold cross-validation to perform our analysis.

Effect on Tracking

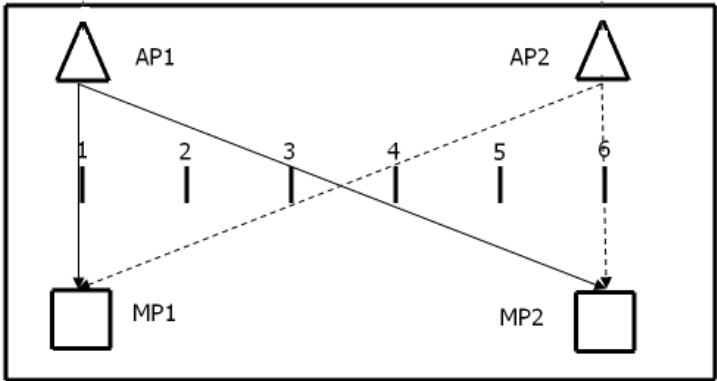
Figure 5.2 shows the average distance error and error probability of the *DfP* system for the three layouts shown in Figure 5.1. It can be noted that Layout 1 has the least error values. As shown in Figure 5.1(a), four locations in Layout 1 intersect with the lines of sight of the streams, whereas in the other two layouts two locations only intersect with the lines of sight. Therefore, Layout 1 is more capable of discriminating locations more than the two other layouts.

Effect on Detection

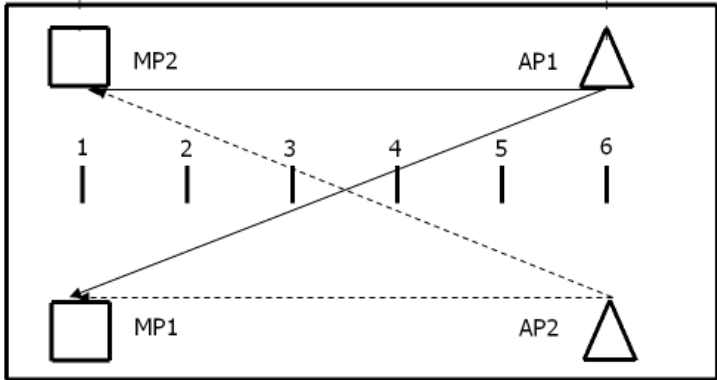
Figure 5.3 shows the FP rate and FN rate of the *DfP* system for the three layouts using the Location-Zero algorithm. It can be observed that the FN rate is much affected by the layout change and Layout 1 has the least FN rate. Table 5.1 shows that Layout 1 has the best accuracy and F-measure.

5.3.2 Location Set Selection

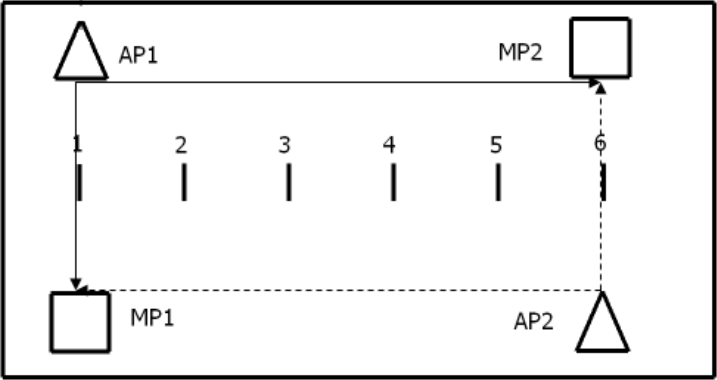
Further analysis of the different layouts shown in Figure 5.1 showed that radio map location set selection affects directly the performance of the *DfP* system.



(a) Layout 1

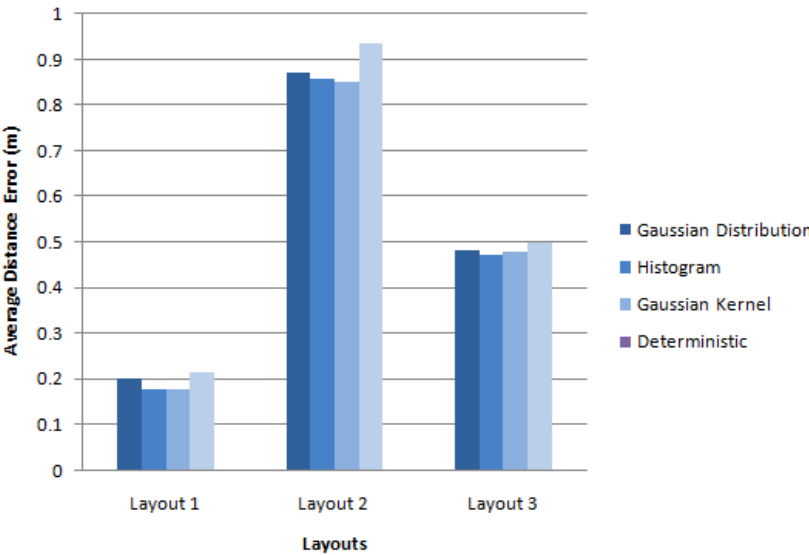


(b) Layout 2

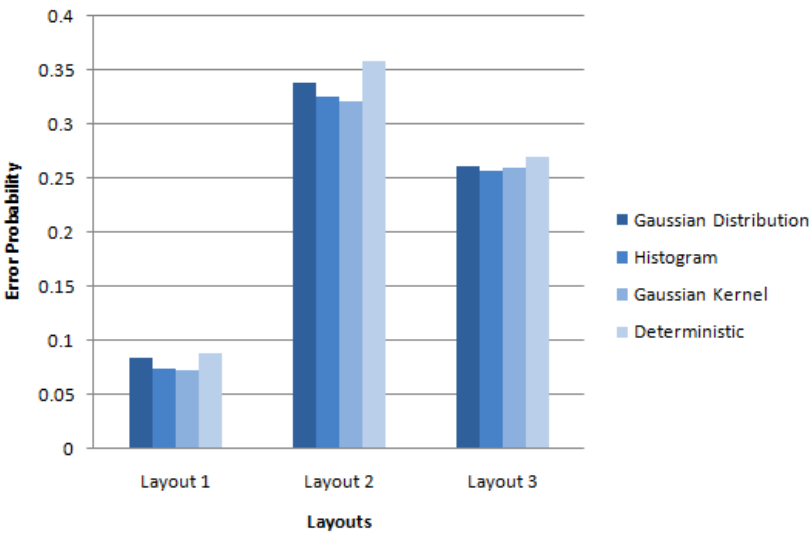


(c) Layout 3

Figure 5.1: Layouts of the three experiments that were performed to study the site planning effect. Lines between APs and MPs represent the direct line-of-sight for the different streams.



(a) Average Distance Error



(b) Error Probability

Figure 5.2: Tracking performance under the three layouts shown in Figure 5.1.

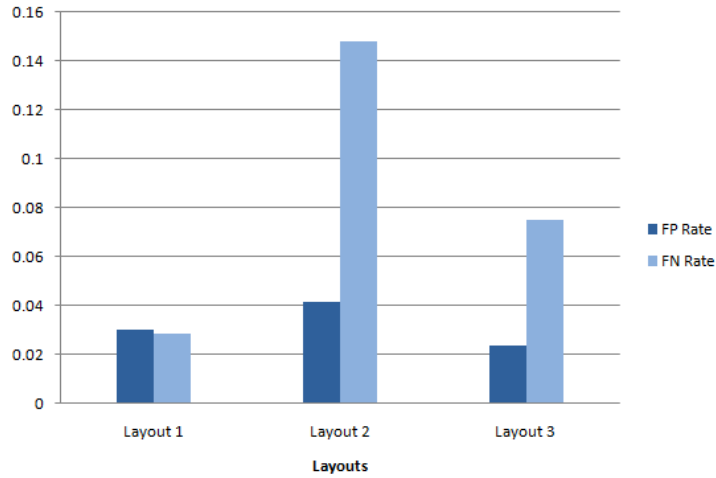


Figure 5.3: Detection performance using Location-Zero algorithm under the three layouts shown in Figure 5.1.

Layout	Accuracy	F-measure
Layout 1	0.97	0.97
Layout 2	0.91	0.90
Layout 3	0.95	0.95

Table 5.1: Accuracy and F-measure the three layouts shown in Figure 5.1.

In this section, we present a comparison between the effects of different radio map location sets on tracking and detection for the three layouts.

Effect on Tracking

Figure 5.4 shows the tracking performance of the system under different radio map location sets for the different three layouts. Considering Layout 1 for example, Figure 5.1(a) shows the locations that affect directly the lines of sight which are (1, 3, 4, 6). Figure 5.4(a) compares between the cross-validation average distance errors if the radio map location set selected was {1, 2, 3, 4, 5, 6}, {2, 5} and {1, 3, 4, 6}. It can be noted that the system performs better when the locations are selected to affect the lines of sight directly. The same can be applied to Layouts 2 and 3.

Effect on Detection

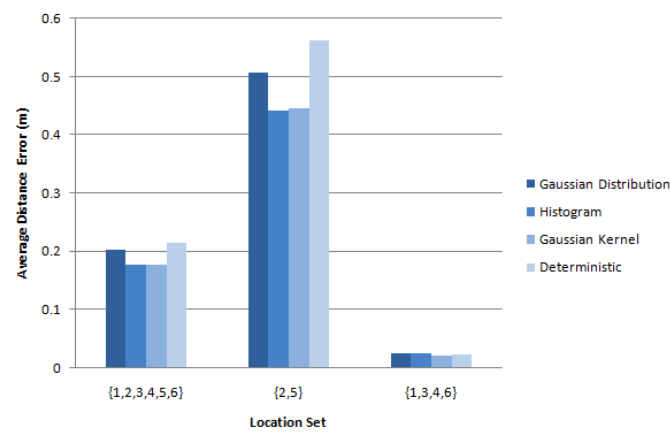
Figure 5.5 shows the detection performance of the system under different radio map location sets for the different three layouts. Actually, some results

may not be consistent with the assumed hypothesis. In future work, we will investigate the relation between detection and location sets.

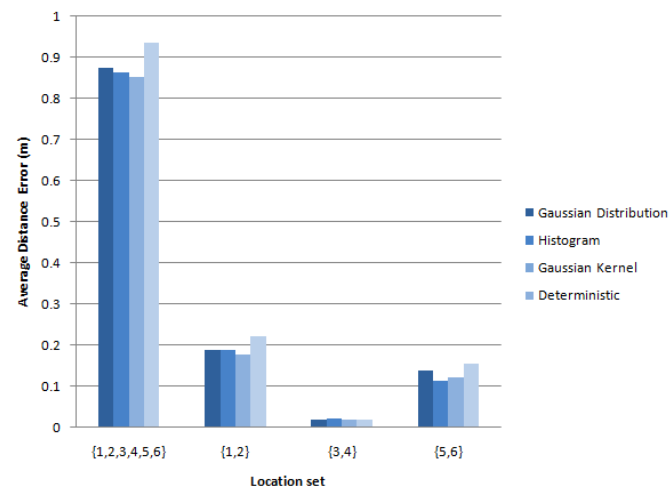
5.3.3 Conclusion

From the tracking results, it can be observed that the choice of the tracking algorithm is not as much effective as layout selection or location set selection for a given site plan. This has to be confirmed however for larger areas of interest.

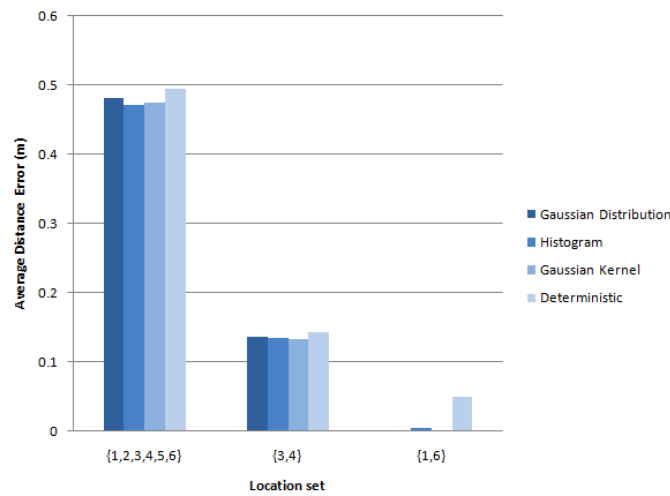
For detection, the hypothesis holds when testing different layouts. However, when testing different location sets, some obtained results were found to need further analysis because some of them may be inconsistent with the hypothesis.



(a) Layout 1

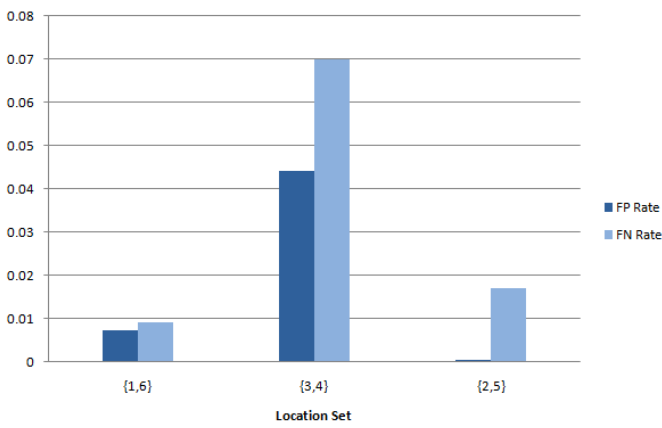


(b) Layout 2

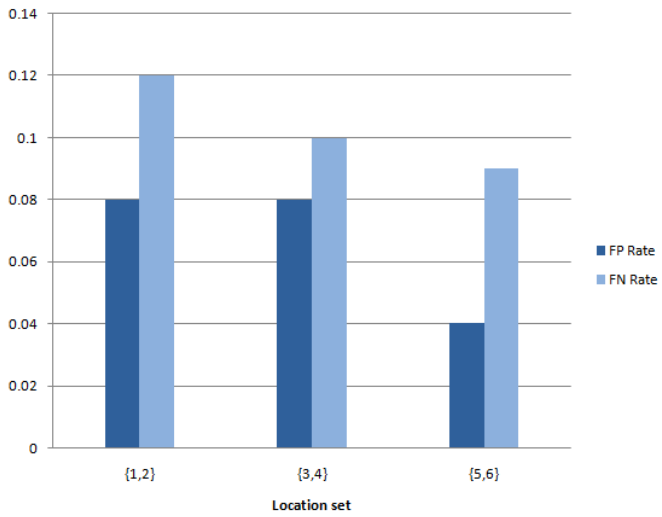


(c) Layout 3

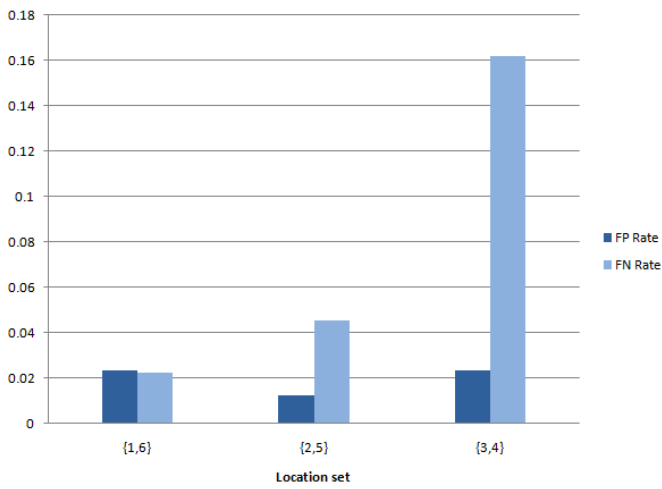
Figure 5.4: Tracking performance under different location sets for the three layouts shown in Figure 5.1.



(a) Layout 1



(b) Layout 2



(c) Layout 3

Figure 5.5: Detection performance using Location-Zero algorithm under different location sets for the three layouts shown in Figure 5.1.

Part III

Electromagnetic Propagation Modeling

Chapter 6

Wave Propagation

6.1 Problem Definition and Modeling Concept

The DfP localization process requires an offline phase, where signal strength is measured at different locations in the environment to generate what is called a radio map. The process of measurements is expensive and error prone. Furthermore, changes in the layout of the access and monitoring points would require the repetition of these measurements.

Finally, the DfP at the current state supports the detection and tracking of a single person in the environment. Supporting the detection or tracking of two persons in the environment requires the square of the number of measurements required for a single person, which is obviously not scalable. An automation of this phase would facilitate the installation of the DfP system greatly. Automating the construction of the radio map requires the prediction of radio propagation in the environment where the DfP system is installed.

However, a typical indoor environment consists of many walls, ceiling, floor and many other objects making it a very complicated environment for modeling. These objects block the direct path (LOS) of wave propagation between transmitters and receivers. The signal undergoes reflection, transmission, scattering and diffraction before reaching the receiver. Multiple signals can reach a receiver through different paths and the total received signal is the summation of all the multipath components received. The amplitude of each component depends on the path it took to reach the receiver. Thus the determination of these paths is essential for the accurate prediction of wave propagation in indoor environments.

Ray tracing is a deterministic technique that can provide an approxi-

mate solution to indoor propagation prediction. Ray tracing models electric fields transmitted from a source by rays that interact with the environment through reflection, transmission and diffraction. Ray tracing has proven to be particularly suitable for modeling the multipath channel encountered in the indoor environment, and thus can provide accurate results for indoor wave propagation prediction.

The inputs to the ray tracing algorithm are a 3D model that represents the indoor environment, a set of sources, and a set of receivers. The output is the signal strength at the monitoring locations. In addition, our tool can predict the signal strength over the entire environment.

6.2 Basic Definitions

6.2.1 Electromagnetics Basics

Electromagnetic Wave [26]:

An electromagnetic wave consists of electric and magnetic field components which oscillate in phase perpendicular to each other and perpendicular to the direction of energy propagation.

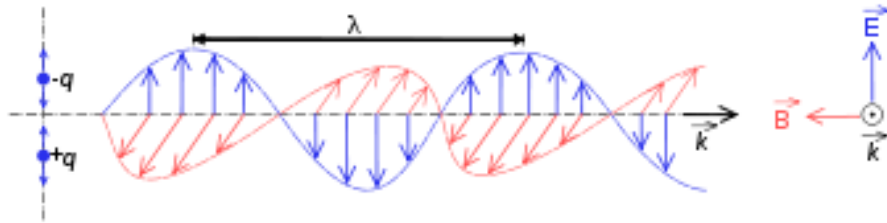


Figure 6.1: Electromagnetic wave.

Wavefront [27]:

A wavefront is the locus of points having the same phase in an electromagnetic wave.

Spherical Wave [27]:

It is the wave with constant phase surfaces (wavefronts) that are concentric spheres.

Phase shift [26]:

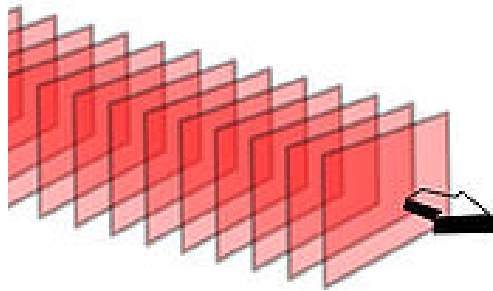


Figure 6.2: An example of a wavefront.

It is the change in the phase of the electric field from some reference point.

Polarization of electromagnetic wave [26]:

It is that property of an electromagnetic wave describing the time varying direction and relative magnitude of the electric field vector, specifically, the figure traced as a function of time by the extremity of the vector at a fixed location in space and the sense in which it is traced as observed along the direction of propagation.

Linear Polarization [26]:

An electromagnetic wave is linearly polarized at a given point in space if the electric field (or magnetic field) vector at that point is always oriented along the same straight line at every instant of time. This is accomplished if the field vector (electric or magnetic) possesses:

1. Only one component, or
2. Two orthogonal linear components that are in time phase or 180 out of phase.”

dBm–dBmW: dB(1 mW) — power measurement relative to 1 milliWatt.

6.2.2 Antenna Basics

Antenna An antenna is a means for radiating or receiving radio waves.

Field Regions [26]

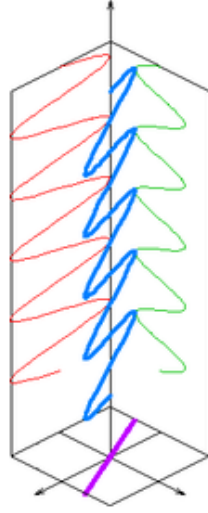


Figure 6.3: Linear polarization.

1. Reactive near-field region

It is the portion of the near-field region immediately surrounding the antenna wherein the reactive field predominates. The outer boundary for this region is $R < 0.62\sqrt{\frac{D^3}{\lambda}}$, where D is the largest dimension of the antenna.

2. Radiating near-field (Fresnel) region

It is the region of the field of an antenna between the reactive near-field region and the far-field region wherein radiation fields predominate and wherein the angular field distribution is dependent upon the distance from the antenna. If the antenna has a maximum dimension that is not large compared to the wavelength, this region may not exist. The boundaries for this region are taken as $0.62\sqrt{\frac{D^3}{\lambda}} = R < \frac{2D^2}{\lambda}$, where D is the largest dimension of the antenna.

3. Far-field (Fraunhofer) region

It is the regions of the field of an antenna where the angular field distribution is essentially independent of the distance from the antenna. The lower bound for this region is taken at $R > \frac{2D^2}{\lambda}$.

Radiation Pattern [26]

An antenna radiation pattern is a mathematical function or graphical representation of the radiation properties of the antenna as a function of space coordinates. In most cases, the radiation pattern is determined in the far-field region. Radiation properties include power flux density, radiation intensity, field strength, directivity, phase or polarization.

Directivity (Directive Gain) [26]

The directivity of a non-isotropic source is equal to the ratio of its radiation intensity in a given direction over that of an isotropic source.

Isotropic Radiator [26]

It is a hypothetical lossless antenna having equal radiation in all directions. Although it is ideal and not physically realizable, it is often taken as a reference for expressing the directive properties of actual antennas.

Directional Antenna [26]

A directional antenna is one having the property of radiating or receiving electromagnetic waves more effectively in some directions than in others.

Omnidirectional Antenna

An omnidirectional antenna is an antenna which radiates power uniformly in one plane with a directive pattern shape in a perpendicular plane. This pattern is often described as ‘donut’ shaped.

Absolute Gain [26]

Absolute gain of an antenna in a given direction is defined as the ratio of the intensity in a given direction to the radiation intensity that would be obtained if the power accepted by the antenna were radiated isotropically. The radiation intensity corresponding to the isotropically radiated power is equal to the power accepted by the antenna divided by 4π .

Relative Gain [26]

It is the ratio of the power gain in a given direction to the power gain of a reference antenna in its referenced direction. When the direction is not stated, the power gain is usually taken in the direction of maximum radiation.

Antenna Polarization [26]

It is the polarization of the wave transmitted by the antenna.

Reciprocity of an antenna [26]

The radiation pattern of an antenna is the same whether it is used as a transmitting antenna or receiving antenna. Reciprocity allows the calculation of an antenna pattern in either the transmission or the reception case.

dBi - dB(isotropic) [28]

Unit of measurement of the forward gain of an antenna compared with the hypothetical isotropic antenna, which uniformly distributes energy in all directions.

Radiation patterns of simple antennas**1. Isotropic antenna**

The isotropic antenna radiates waves equally in all directions. The radiation pattern of an isotropic antenna is spherical in shape.

The gain function is:

$$G(\theta, \varphi) = 1 \quad (6.1)$$

2. Half wave dipole[29]

The radiation pattern of a half wave dipole is omnidirectional. The gain is a function of the elevation angle θ .

$$G(\theta, \varphi) = \frac{\cos\left(\frac{\pi}{2}\cos\theta\right)}{\sin\theta} \quad (6.2)$$

6.3 Comparison of Ray Tracing Models**Image Method**

[21]

This method generates the images of a source at all planes. These images then serve as secondary sources for the subsequent points of reflections. If there are N reflecting planes, then there are N first-order images of a source, $N(N-1)$ two-reflection images, $N(N-1)(N-1)$ three-reflection images, and so on. To determine whether

an image of the source is visible at the destination is to trace the intersection of the reflected ray at all necessary planes of interest.

The image method is efficient, but it can only handle simple environments.

Brute Force Method

[21]

This method considers a bundle of transmitted rays that may or may not reach the receiver. The number of rays considered and the distance from the transmitter to the receiver location determine the available spatial resolution, and hence, the accuracy of the model.

This method requires more computing power than the image method but it is able to handle complex environments.

6.4 Rays Tessellation

Transmitters are modeled as point sources whose wave-fronts are spherical in shape [30]. It is necessary to consider all possible angles of departure at the transmitter in order to be able to determine all possible rays leaving the transmitter and arriving at the receiver. Therefore, each wavefront is divided into a set of ray tubes that cover the entire spherical wave-front. Each ray tube should occupy the same solid angle $d\Omega$ and cover an identical part of the wavefront.

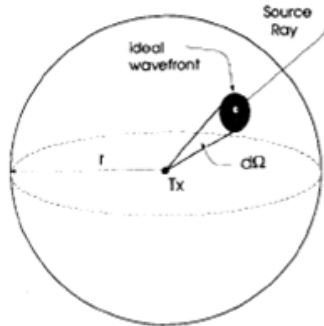


Figure 6.4: Source Ray Wavefront.

Furthermore, the ray launching technique must exhibit two forms of uniformity [30]:

1. Large-Scale Uniformity - The launch points must distribute evenly around the spherical wave-front so that all regions of space are illuminated equally by rays. Large-scale uniformity delivers unbiased ray coverage in three dimensions.
2. Small-Scale Uniformity - The local pattern of rays impinging on a wave-front should be a predictable, uniform pattern. This corresponds to equal angles between a ray and its neighbors, which assists the interpretation of wave-front information.

These conditions can be satisfied only by launching rays from the vertices of a regular polyhedron. A regular polyhedron is a polyhedron whose faces are congruent regular polygons which are assembled in the same way around each vertex (Regular Polyhedron). However, no regular polyhedron has more than twenty vertices, which means that only a small number of rays can be launched using this technique.

The most popular method uses the theory of geodesic domes. An icosahedron is inscribed inside a unit sphere (Seidel & Rappaport, 1994). An icosahedron is a convex regular polyhedron composed of twenty triangular faces, with five meeting at each of the twelve vertices. It has 30 edges and 12 vertices (Icosahedron). If rays are launched at each of the 12 vertices, each ray wave-front would be an identically shaped pentagon separated by 63° from each of its five nearest neighbors.

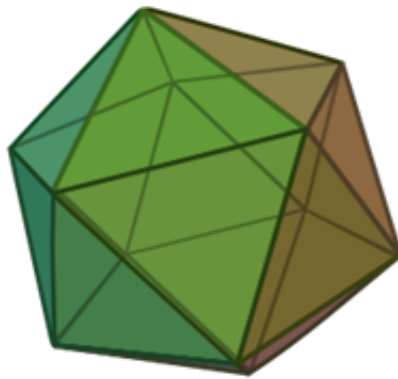


Figure 6.5: Icosahedron.

Figure 2 Icosahedron

To provide higher angular resolution, each triangle edge is tessellated into N segments, where N is called the tessellation frequency. Parallel lines to edges are then drawn dividing each face into smaller equilateral triangles. Rays are launched to pass through the vertices of these triangles.

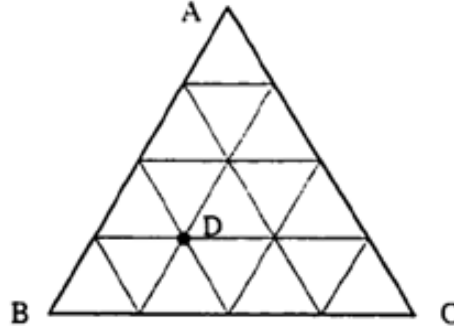


Figure 6.6: Tessellated Triangle.

Any vertex D inside triangle ABC can be represented by [31]:

$$\overline{OD} = \overline{OB} + i * \frac{\overline{AB}}{N} + j * \frac{\overline{BC}}{N} \quad \forall i, j = 0 \dots N \quad (6.3)$$

The number of launched rays equals $10N^2 + 2$. This method of launching rays provides wave-fronts that completely subdivide the surface of the unit sphere with nearly equal shape and area. Each ray that passes through the interior and edge vertices will have exactly six neighbors and therefore will have a hexagonal wave-front (Regular triangles, squares, and hexagons can completely cover an area with equal size and shape objects without leaving gaps.)

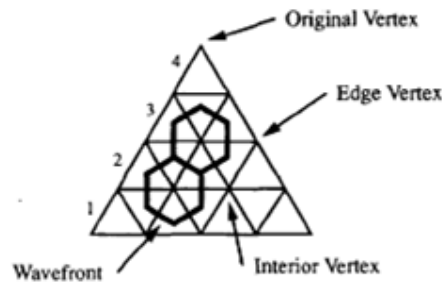


Figure 6.7: Hexagonal Wavefront for interior vertices.

Despite the simplicity of this method, there are some discrepancies in the angular separation among the launched rays [30].

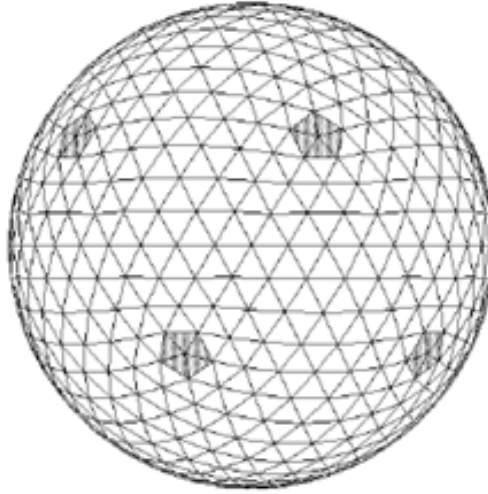


Figure 6.8: Abberation at the icosahedron vertices.

Each ray emanating from the vertices of the icosahedrons will have five neighbors and thus will have a pentagonal wave-front. While, as mentioned before, other rays will have a hexagonal wave-front. This also causes the angular separation to be different among rays. However, this type of aberration becomes insignificant for highly tessellated frequencies.

Another aberration occurs in the angular separation between rays. There is an average discrepancy of twenty percent between the smallest and largest angular separations on the sphere regardless of the tessellation frequency.

Despite aberrations, an average value for angular separation (α) is a useful parameter in a simulation. A very good approximation for the angular separation that takes the tessellation frequency N into account is [30]:

$$\alpha = \frac{69.0^\circ}{N} \quad (6.4)$$

6.5 Reception Sphere

Receivers are also modeled as points. Each ray tube occupies a solid angle that represents the field in that direction. A ray is considered received if the point receiver location is included within this solid angle.

A common method to identify the received ray is the reception sphere model [32]. This method assumes uniform ray launching from a geodesic sphere, which implies a constant angular separation between rays. The reception sphere model surrounds a receiver point with a sphere of varying size.

If the ray from the transmitter passes through the reception sphere, then, equivalently, the point receiver intercepts the transmitted solid angle.

Rays spread out as they leave the source and the reception sphere effectively accounts for this divergence. The size of the reception sphere increases in correspondence to this divergence. The radius of the sphere depends on the characteristics of the ray under test, specifically the projection of the receiver on the ray and the total unfolded distance travelled by the ray.

In addition, the size of the reception sphere should guarantee the recipient of at most one ray from each wave-front. If it is too large, more than one ray from the same wave-front is received. An undersized reception sphere can miss a wave-front altogether.

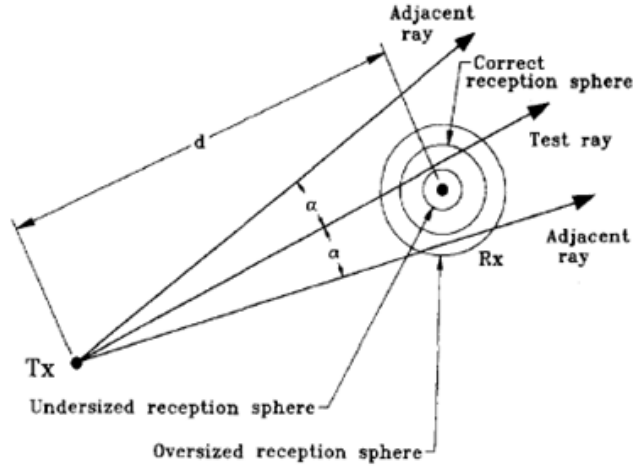


Figure 6.9: 2D view of the reception sphere.

In order to make sure that a point is not missed, the ray wave-front is considered a circle circumscribed about the hexagonal wave-front shape. Radius of the circle that circumscribes a regular hexagon is the same as the hexagon side length (r). Radius of the circle inscribed in a regular hexagon (a) is (Hexagon).

$$a = \frac{1}{2}\sqrt{3}r \quad (6.5)$$

α is the angular distance between the centers of two adjacent hexagonal wave-fronts.

$\frac{\alpha}{2}$ is the angular distance between a hexagon center and its inscribed circle.

l is the distance between the source point and a hexagon center.

Using simple trigonometry, we equate:

$$\frac{\alpha}{2} = \frac{a}{l} \quad (6.6)$$

$$\frac{\alpha}{2} = \frac{\sqrt{3}r}{2l} \quad (6.7)$$

$$r = \frac{\alpha * l}{\sqrt{3}} \quad (6.8)$$

This equation is valid for small values of α , which is the case for large tessellation frequencies.

As observed, the circumscribed radius was used instead of the inscribed radius, so that the circles cover the entire wave-fronts. It should also be noted that the reception sphere is different for each ray path.

Finally, a reception sphere is constructed about the receiver with a radius equals to that of the circumscribed radius (r).

For ray separation α sufficiently small, the ray intercepting the sphere will be an accurate measure of the ray that would pass directly through the receiving point.

The main advantage of this technique is the simplicity of its implementation (simple ray-sphere intersections.)

A problem with that model is the double count problem [30]. The cause of the problem is that there is an overlap between the circumscribed circles of neighboring wave-fronts. This may cause the recipient of two rays of the same wave-front registering additional power at the receiver. For the ideal case, the double counting occurs with a probability of 20.9% of the time. This probability is independent of the tessellation frequency. A simple solution to the double count problem is the elimination of overlapped rays during the sampling phase.

Another disadvantage of the reception sphere model is the need of a constant angular separation between rays.

The implementation of the reception sphere is as follows:

1. Finding the location of the projection of the receiver location on the ray path.
2. Calculating the length of the total unfolded distance traveled by the ray until the point of projection calculated in (1).
3. Calculating the perpendicular distance between the ray and the receiver location (d), which is the distance between the receiver location and the point of projection calculated in (1).

4. Calculating the reception sphere radius (r) using the length calculated in (2).
5. If $d \leq r$ then the ray is received by the receiver.

6.6 Ray Tracing Algorithm

The ray tracing algorithm can be divided into the following stages:

1. Launching rays from sources using geodesic spheres.
2. Finding intersections.

The ray tracing algorithm utilizes the underlying triangulated representation of the environment to efficiently test for intersection and find interaction points between traced rays and the environment. Interaction events are any of reflection, transmission, or diffraction. Intersection points are calculated through the jME intersection routines, yet some processing is necessary to capture the right triangle where the intersection really occurred. After finding the exact point where the intersection occurred, an event is triggered.

3. Generation of new rays.

Triggered events are processed and new rays are produced by computing reflected, transmitted, and diffracted rays if needed.

4. Electromagnetic-specific calculations which will be discussed in next chapter.
5. Reception of rays at receivers using reception spheres.

A pseudo code for the algorithm follows:

```

    create the triangulated representation of the environment (done by the jME)
extract all edges
detect wedges and corners
place human bodies
surround wedges, corners, and human bodies by bounding capsules for later detection
for each transmitter TX
begin
    create the set of launched rays and store them in the queue Q.
    for I = 1 to tracing_depth

```

```

begin
  While (Q) is not empty
  begin
    pop a ray from Q
    find next interaction event between the ray and the environment
    process the event
    update field and apply the UTD model accordingly
    if ray is receivable by a receiver
    begin
      receive the ray
      update received signal strength
    end
  end
end
end
start the sampling process to cover the whole floor

```

Human bodies in the LOS between a transmitter and a receiver are handled separately. A purposeful launching of tangential rays is invoked where the incident rays are all diffracted around the cylindrical body, and the UTD for cylindrical diffraction is applied. Human bodies in the NLOS are handled in the tracing process accordingly.

Loosely speaking, diffracted rays need some special handling in order to apply the UTD diffraction model. UTD assume the existence of an observation point, which requires triggering a future event in the tracing process. In our implemented, diffracted rays are flagged as so, and they receive the appropriate treatment in the next tracing iteration.

The implementation also counts for ceilings and the mathematical model adapts the existence of a virtual ceiling in the model. Rays interacting with the ceiling only diffract or reflect, but do not transmit through the ceiling.

To avoid missing a LOS interaction between sources and receivers, as a source can only transmit a limited number of rays, all receivers are checked for LOS interaction with each source at the beginning of the source's tracing iteration.

A ray is removed from tracing, if one of the two conditions occurs:

1. The depth of the ray reaches a defined maximum value.
2. The power of the ray drops below a defined minimum value.

Chapter 7

Propagation Models

7.1 Power Model and Path Loss

In order to predict the received signal strength from a transmitter that emits waves of wavelength λ , it is required to estimate electromagnetic waves propagation characteristics through the environment. There are several methods for propagation modeling; in this section, we will focus and discuss the two implemented methods, namely the Path Loss and the Electric Field methods.

7.1.1 Path Power

Many propagation paths exist from a transmitter to a receiver due to reflection, transmission, scattering, and diffraction effects. Each path contributes either positively or negatively to the received signal by a receiver. A single path may add to or subtract from the received power P_r depending on the phase shift of that path at the receiver.

In the geometric optics model, a propagation path consists of a chain that starts at the transmitter and ends at the receiver. The chain consists of a set of vertices that lie on obstacles in the environment of simulation. Let d be the total unfolded distance of that chain (length of the path labeled ‘abcdef’ in Figure 1), then the power transmitted over that path to the receiver is calculated by using Friis’s formula [33]:

$$P_r = P_t * G_r * G_t * \Gamma * \left(\frac{\lambda}{4\pi d} \right)^2 \quad (7.1)$$

Where P_t is the power input to the transmitter, G_r and G_t are the receiver and transmitter antenna gains, and Γ is the aggregation of reflections and transmissions coefficients along the chain path. Antenna gain defines power

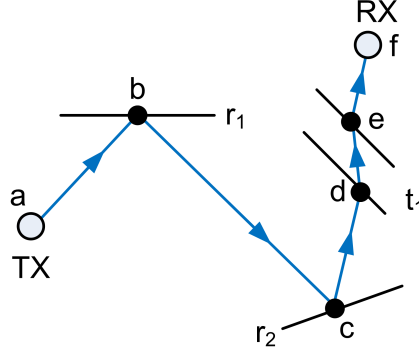


Figure 7.1: One possible signal path from TX to RX through different interactions; r_1 and r_2 are reflection coefficients, and t_1 is a transmission coefficient.

output variation in different directions across the wave front. For a receiver, it defines the receiver sensitivity to arriving signals across the wave front. When the transmitter and receivers are isotropic, $G_r = G_t = 1$.

To put things into perspective, a chain of n reflections and m transmissions results in a Γ value of:

$$\Gamma = r_1 * r_2 * \dots * r_n * t_1 * t_2 * t_3 * \dots * t_m \quad (7.2)$$

Where $r_{1...n}$ and $t_{1...m}$ are the GO reflection and transmission coefficients along the chain.

Reflection coefficients are calculated from Fresnel's equations as [34]:

$$r_{\perp} = \frac{n_1 \cos \theta^i - n_2 \cos \theta^t}{n_1 \cos \theta^i + n_2 \cos \theta^t} \quad (7.3)$$

$$r_{\parallel} = \frac{n_1 \cos \theta^t - n_2 \cos \theta^i}{n_1 \cos \theta^t + n_2 \cos \theta^i} \quad (7.4)$$

Transmission coefficients are calculated from [34]:

$$t_{\perp} = 1 - r_{\perp} \quad (7.5)$$

$$t_{\parallel} = 1 - r_{\parallel} \quad (7.6)$$

For reflections and transmissions with the floor or ceiling, the parallel coefficients are used, and the perpendicular reflection and transmission coefficients are used when the ray intersects a vertically oriented wall [32].

7.1.2 Received Power

All paths contribute to the received power at the receiver. The contribution positivity depends on the signal's phase at the receiver. Let p_i be path i 's power at the receiver, then the total power received is calculated from [35]:

$$P_r = \sum p_i e^{j\left(\frac{2\pi d_i}{\lambda} + \sum \varphi(k)\right)}$$

Where:

d_i is the unfolded length of path i , $\varphi(k)$ is the phase shift (either 0 or π) that occurred at event k (either reflection or transmission), where $k=0 \dots \#$ of events.

7.1.3 Path Loss

Path Loss (PL) is a measure of the average RF attenuation suffered by a transmitted signal when it arrives at the receiver; it is defined by [36, 32]:

$$PL(dB) = 10 * \log_{10} \frac{P_t}{P_r} \quad (7.7)$$

Hence, the final received power level, in dB, at the receiver is calculated from [32]:

$$P_r(dB) = P_t(dB) - PL \quad (7.8)$$

7.1.4 Polarization Loss

A receiver antenna has an associated electric field E with polarization vector V . Polarization of arriving signals at the receiver infrequently match V , which causes some more attenuation termed *polarization loss*. Polarization loss can be neglected, as it ranges from -1 to -3 dBm [26].

7.2 Electric Field Model

The electric field model uses GO to predict the electric fields at different observation points. It takes into account electric field properties like phase shift and polarization which causes the prediction to be more accurate. The GO studies direct and reflected electric fields only. A derivation of an expression for the reflected electric field for a non perfect electrically conducting (PEC) surface is provided. A typical 3D environment consists of non-PEC surface, which makes it more suitable.

7.2.1 Initial electric field $E(0)$

Assumption: All antennas are vertically polarized with spherical wave-fronts.

Given an antenna with transmitting power P_t and gain $G(\theta, \varphi)$, the power density P_d for a ray emitted at an zenith angle θ and azimuth angle φ at distance r from the antenna: (Power Density)

$$P_d(\theta, \varphi, r) = \frac{P_t G(\theta, \varphi)}{4\pi r^2} \quad (7.9)$$

Since [37]

$$E(\theta, \varphi, r) = \sqrt{P_d(\theta, \varphi, r) * Z_0} \quad (7.10)$$

And

$$Z_0 = 120\pi \quad (7.11)$$

Therefore,

$$E(\theta, \varphi, r) = \frac{\sqrt{30 P_t G(\theta, \varphi)}}{r} \quad (7.12)$$

The amplitude of the initial electric field is calculated at $r = 1$ m.

Since all antennas are assumed to be vertically polarized, the electric fields of the transmitted rays are polarized in the vertical plane in the $\hat{\theta}$ direction.

The phase shift of the electric field of the emitted ray is initialized to zero.

The electric field is studied in the far region of the antenna. The radii of curvature of the transmitted ray tubes should be initialized to the start of the antenna's far region. Assuming that the far region start at a distance equals the wavelength of the transmitted wave, the radii of curvature are initialized to this wavelength.

7.2.2 Electric Field Propagation

The expression describing the propagation of the electric field for a general ray tube is [27]:

$$E(s) = E(0) \sqrt{\left| \frac{\rho_1 \rho_2}{(\rho_1 + s)(\rho_2 + s)} \right|} e^{-jks} \quad (7.13)$$

Where:

$E(0)$ gives the field amplitude, phase and polarization at the reference point $s = 0$.

s is the distance along the ray path from the reference point $s = 0$.

e^{-jks} gives the phase shift along the ray path.

k is the wave number $= \frac{2\pi}{\lambda}$

$A(s) = \sqrt{\left| \frac{\rho_1 \rho_2}{(\rho_1 + s)(\rho_2 + s)} \right|}$ is the spreading factor which governs the amplitude variation of the GO field along the ray path,

ρ_1 and ρ_2 are the principal radii of curvature of the wave-front at the reference point $s = 0$.

For the spherical wave ray tube $\rho_1 = \rho_2 = \rho$ and the spreading factor $A(s)$ becomes:

$$A(s) = \frac{\rho}{(\rho + s)} \quad (7.14)$$

And the electric field becomes:

$$E(s) = E(0) \frac{\rho}{(\rho + s)} e^{-jks} \quad (7.15)$$

Where $E(0)$ is the electric field at the reference point. The radii of curvature at distance s equals:

$$\rho_s = \rho + s \quad (7.16)$$

And the polarization vector remains the same as the reference point.

7.2.3 Electric Field Reflection and Transmission for non-PEC surfaces

Since the surfaces are non PEC, a fraction of the electric field incident on the surface reflects off the surface and the rest transmits through the surface. The ratio of these fractions depends on the characteristics of both mediums as well as the angle of incidence of the incident ray.

Consider a ray tube propagates in free space from some source. The ray tube impacts a smooth surface at a point Qr. This ray tube has a ray

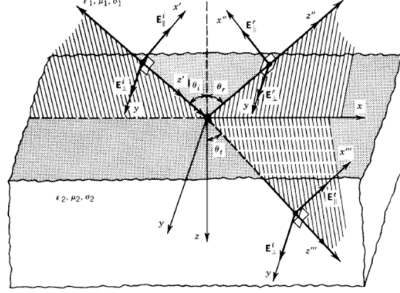


Figure 7.2: Geometry of reflection and transmission.

coordinate s_i measured along the central ray and is completely described by its central ray vector \hat{s}^i , principal radii of curvature ρ_{i1} and ρ_{i2} at the selected reference point Q_s , and a knowledge of the initial electric field $E_i(Q_s)$ at the reference point Q_s .

Ray-fixed coordinate system

As mentioned before [27], \hat{s}^i is the incident ray that strikes the reflecting surface at Q_r . Let \hat{n} be the unit normal to the reflecting surface at Q_r , \hat{s}^r be the reflected ray at Q_r , and \hat{s}^t be the transmitted ray at Q_r . Both \hat{s}^i and \hat{n} define the plane of incidence. Similarly, both \hat{s}^r and \hat{n} define the plane of reflection, and both \hat{s}^t and \hat{n} define the plane of transmission.

The incident electric field E_i at Q_r can be resolved into two components parallel (\hat{e}_{\parallel}^i) and perpendicular (\hat{e}_{\perp}^i) to the plane of incidence. Similarly, the reflected electric field E_r at Q_r can be resolved into two components parallel (\hat{e}_{\parallel}^r) and perpendicular (\hat{e}_{\perp}^r) to the plane of reflection. The transmitted electric field E_t at Q_r can be resolved into two components parallel (\hat{e}_{\parallel}^t) and perpendicular (\hat{e}_{\perp}^t) to the plane of transmission.

Using the diagram, we can prove the following geometrical relations:

$$\hat{e}_{\perp}^i = -\hat{n} \times \hat{s}^i \quad (7.17)$$

$$\hat{e}_{\parallel}^i = \frac{\hat{s}^i \times (\hat{n} \times \hat{s}^i)}{|\hat{s}^i \times (\hat{n} \times \hat{s}^i)|} \quad (7.18)$$

$$\hat{e}_{\perp}^r = -\hat{n} \times \hat{s}^r \quad (7.19)$$

$$\hat{e}_{\parallel}^r = \frac{\hat{s}^r \times (\hat{n} \times \hat{s}^r)}{|\hat{s}^r \times (\hat{n} \times \hat{s}^r)|} \quad (7.20)$$

$$\hat{e}_{\perp}^t = -\hat{n} \times \hat{s}^t \quad (7.21)$$

$$\hat{e}_{\parallel}^t = \frac{\hat{s}^t \times (\hat{n} \times \hat{s}^t)}{|\hat{s}^t \times (\hat{n} \times \hat{s}^t)|} \quad (7.22)$$

This system is called a local ray-fixed coordinate system because it links the incident ray direction \hat{s}^i , the reflected ray direction \hat{s}^r , the transmitted ray direction \hat{s}^t , and the unit normal at Qr.

The trajectories of the reflected and transmitted ray tubes are:

$$\hat{s}^r = \hat{s}^i - 2(\hat{n} \cdot \hat{s}^i)\hat{n} \quad (7.23)$$

$$\hat{s}^t = \cos\left(\sin^{-1}\frac{n_1\sin\theta^i}{n_2}\right)\hat{n} + \left(\frac{n_1\sin\theta^i}{n_2}\right)\left(\frac{\hat{s} - \cos\theta^i\hat{n}}{\sin\theta^i}\right) \quad (7.24)$$

7.2.4 Polarization of the reflected and transmitted rays

Using the ray-fixed coordinate system, the incident, the reflected and the transmitted electric fields are resolved into two components parallel and perpendicular to the plane of incidence [27].

$$E^i = (E^i \cdot \hat{e}_{\parallel}^i)\hat{e}_{\parallel}^i + (E^i \cdot \hat{e}_{\perp}^i)\hat{e}_{\perp}^i = E_{\parallel}^i\hat{e}_{\parallel}^i + E_{\perp}^i\hat{e}_{\perp}^i \quad (7.25)$$

$$E^r = (E^r \cdot \hat{e}_{\parallel}^r)\hat{e}_{\parallel}^r + (E^r \cdot \hat{e}_{\perp}^r)\hat{e}_{\perp}^r = E_{\parallel}^r\hat{e}_{\parallel}^r + E_{\perp}^r\hat{e}_{\perp}^r \quad (7.26)$$

$$E^t = (E^t \cdot \hat{e}_{\parallel}^t)\hat{e}_{\parallel}^t + (E^t \cdot \hat{e}_{\perp}^t)\hat{e}_{\perp}^t = E_{\parallel}^t\hat{e}_{\parallel}^t + E_{\perp}^t\hat{e}_{\perp}^t \quad (7.27)$$

7.2.5 Amplitude of the reflected and transmitted fields

The ratio of the amplitude of the reflected and the transmitted electric fields is given by Fresnel reflection (Γ) and transmission (T) coefficients [34]. Fresnel coefficients depend on the polarization of the incident field. For a field polarized in the perpendicular direction to the plane of incidence, Fresnel coefficients are:

$$\Gamma_{\perp} = \frac{E_{\perp}^r}{E_{\perp}^i} = \frac{n_2 \cos \theta^i - n_1 \cos \theta^t}{n_2 \cos \theta^i + n_1 \cos \theta^t} \quad (7.28)$$

$$T_{\perp} = \frac{E_{\perp}^t}{E_{\perp}^i} = \frac{2n_2 \cos \theta^i}{n_2 \cos \theta^i + n_1 \cos \theta^t} \quad (7.29)$$

While for a field polarized in the parallel direction to the plane of incidence, Fresnel coefficients are :

$$\Gamma_{\parallel} = \frac{E_{\parallel}^r}{E_{\parallel}^i} = \frac{-n_1 \cos \theta^i + n_2 \cos \theta^t}{n_1 \cos \theta^i + n_2 \cos \theta^t} \quad (7.30)$$

$$T_{\perp} = \frac{E_{\perp}^t}{E_{\perp}^i} = \frac{2n_2 \cos \theta^i}{n_1 \cos \theta^i + n_2 \cos \theta^t} \quad (7.31)$$

Where:

n_1 is the absolute refractive index of the first medium.

n_2 is the absolute refractive index of the second medium.

θ^i is the angle of incidence.

θ^t is the angle of transmission obtained from Snell's Law.

The reflected field can be expressed in terms of the incident field and Fresnel reflection coefficients as:

$$E^r = (E^i \cdot \hat{e}_{\parallel}^i) \Gamma_{\parallel} \hat{e}_{\parallel}^r + (E^i \cdot \hat{e}_{\perp}^i) \Gamma_{\perp} \hat{e}_{\perp}^r = E_{\parallel}^i \Gamma_{\parallel} \hat{e}_{\parallel}^r + E_{\perp}^i \Gamma_{\perp} \hat{e}_{\perp}^r \quad (7.32)$$

Similarly, the transmitted field can be expressed in terms of the incident field and Fresnel transmission coefficients as:

$$E^t = (E^i \cdot \hat{e}_{\parallel}^i) T_{\parallel} \hat{e}_{\parallel}^t + (E^i \cdot \hat{e}_{\perp}^i) T_{\perp} \hat{e}_{\perp}^t = E_{\parallel}^i T_{\parallel} \hat{e}_{\parallel}^t + E_{\perp}^i T_{\perp} \hat{e}_{\perp}^t \quad (7.33)$$

A negative reflection coefficient means an increase in the phase shift by 180 degree.

By the summation of the two components using vector sum, the amplitude and the polarization of the resultant reflected or transmitted field are obtained.

Total reflection

The ray incident on a surface of lower optical density (i.e. $n_2 < n_1$) may suffer from total reflection. This condition occurs when the angle of incidence is greater than the critical angle θ_c where

$$\theta_c = \sin^{-1} \frac{n_2}{n_1} \quad (7.34)$$

Principal radii of curvature of the reflected ray tube

The incident ray tube is spherical, $\rho_1^i = \rho_2^i = \rho$, and all surfaces are assumed planar. The radii of curvature of the reflected ray then reduce to [27]:

$$\rho_1^r = \rho_2^r = \rho$$

7.2.6 Calculating of the received power (Power Density)

Using the reception sphere method described before, the received rays are obtained. Assume that the reception antenna has gain $G(\theta, \varphi)$ for a ray received at an zenith angle θ and an azimuth angle φ . The electric fields of all rays are accumulated as follows

Let X , Y , and Z be complex numbers, and E be the electric field of a ray having P as polarization vector and δ as phase shift.

Then,

$$X = \sum_i |E_i| (\cos \delta_i + j \sin \delta_i) (P_i.x) \sqrt{G(\theta_i, \varphi_i)} \quad (7.35)$$

$$Y = \sum_i |E_i| (\cos \delta_i + j \sin \delta_i) (P_i.y) \sqrt{G(\theta_i, \varphi_i)} \quad (7.36)$$

$$Z = \sum_i |E_i| (\cos \delta_i + j \sin \delta_i) (P_i.z) \sqrt{G(\theta_i, \varphi_i)} \quad (7.37)$$

The magnitude of the total received field is calculated from:

$$M = \sqrt{X^2 + Y^2 + Z^2} \quad (7.38)$$

This magnitude takes into consideration the polarization effect as well as the phase shift between different electric fields.

Power density P_d equals:

$$P_d = \frac{M^2}{Z_0} = \frac{M^2}{120\pi} \quad (7.39)$$

Antenna effective area equals:

$$A_e = \frac{\lambda^2}{4\pi} \quad (7.40)$$

The total power received is:

$$P_r = P_d * A_e \quad (7.41)$$

The gain of the receiving antenna is included in the total electric magnitude equation instead of the effective area equation to represent the effect of different arrival angles (θ, φ) while preserving the effect of polarization.

Chapter 8

Diffraction using the UTD

8.1 Why GTD/UTD

In this section, we address different methods of modeling electromagnetics interaction with structures in the environment where an antenna is installed. The section looks at three different models, and emphasizes the pros and cons of each.

The most three common ways of modeling antenna interaction are [28]:

1. Integral functions,
2. Finite Difference Time Domain (FDTD), and
3. Diffraction Theory.

8.1.1 Integral Functions Method

Integral functions method, also known as “Method of Moments”, models a structure as a set of conducting wires or flat patches. As the word integral sounds, it’s mainly a surface model. That’s a conducting structure surface is only modeled, not the whole volume of the structure. That makes it apparent that a separate volume model may be necessary if the presence of a dielectric has to be included.

Integral functions method calculates the current on each segment (wire or patch) in the model. The method is too efficient at determining far-field and near-field radiation patterns and impedance. However, there are major limitations caused by the amount of memory storage required at the long runtimes. That’s caused by the requirement that each segment length must be less than 0.25 of the antenna wave length [38]. Also, the size of a structure

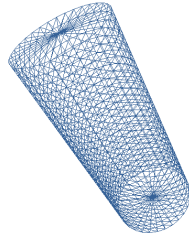


Figure 8.1: Wire grid model of a cylinder.

matrix grows exponentially with the dimensions of the structure, and thus increases the cost of matrices manipulation.

For example, a wireframe model of a P-3/CP-140 aircraft had 327 segments for 2-30 MHz. This corresponds to a segment length of 0.2λ . A model for a BAC-111 aircraft at HF had 7736 segments and took 30,000 seconds to run on a CRAY-2 computer. A PENTIRUM 200 MHz pc with 128 Mbytes of memory handles up to 4000 segments with a runtime of 1.5 hours [39]. Figure 8.1 shows an example of a wire grid model.

8.1.2 Finite Difference Time Domain (FDTD)

FDTD is a volume method where a structure volume is divided into cells whose shapes, in general, are cuboids [40]. The advantage of FDTD is that each cell can has its own properties so that imperfect conductors and dielectrics can be modeled. There is no matrix manipulation and the method works by advancing time steps [40]. Yet, the method is known for long runtimes and excessive memory usage. For example, a volume of $120 \times 120 \times 120$ cells requires 128 Mbytes of memory, and the runtime extends to several hours [40].

8.1.3 Diffraction Theory

The Geometrical Theory of Diffraction (GTD) is a ray-tracing method that was developed by Keller in 1950s as an extension to geometrical optics. Keller added diffracted rays and he succeeded to correct the deficiency in the GO that predicts zero fields in the shadow regions. Keller's GTD, however, still had shortcomings. It suffered from singular fields in certain regions, specifically the transition regions surrounding the shadow boundaries of a structure, the so-called nonuniformity.

GTD implies the following assumptions:

1. All dimensions are greater than 1 wavelength.

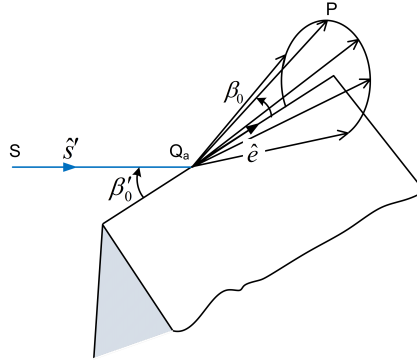


Figure 8.2: Geometrical Representation of Keller's Law of Diffraction.

2. All objects are in the far-field (solved by the Uniform Theory of Diffraction).
3. Currents are not used, so it is impossible to obtain impedance data.

Keller stated that diffracted rays exist and that they are produced when GO rays illuminate wedges, corners and vertices of boundary surfaces. Keller also formulated a law of diffraction that determines the location of a diffraction point and the direction and field of a diffracted ray in a manner analogous to how the law of reflection determines the location of a reflection point and the direction of propagation of a GO reflected ray. Keller noted that whenever an incident field illuminated an edge, the diffracted rays propagate along parallel cones with the edge as their common axis. Keller then stated the *law of diffraction* as follows [27]:

A diffracted ray and the corresponding incident ray make equal angles with the edge at the point of diffraction, provided they are in the same medium. They lie on opposite sides of the plane normal to the edge at the point of diffraction.

Unlike Integral and FTDT methods, where the same method is applied to the entire structure, in GTD there are different diffraction coefficients for different types of geometric objects. The coefficients are all derived from Keller's theory.

Advantages of GTD/UTD include, but not limited to, the following:

1. Ray-tracing is independent of the structure size. Thus, there is no limitation on the dimensions of the structure, not there any runtime overhead with respect to antenna frequency.

2. Ray-tracing is not memory intensive.
3. GTD/UTD produces accurate results when proper ray-tracing parameters are used (such as the tessellation frequency, and depth of tracing).
4. Optimizations to ray-tracing algorithms directly improve the method performance.

At present, diffraction coefficients for imperfect conductors and dielectrics are poorly determined.[28] Thus, and assumption is made here that all structures are perfect conductors. Available diffraction coefficients include:

1. Reflection off a plane or curved surface.
2. Diffraction off a wedges and corners.
3. Diffraction off a curved surface, the so-called ‘creeping waves’.

We end this discussion by a side-by-side comparison of the three models:

	Integral Equations	FDTD	GTD/UTD
Structure model	Wire-grid	Cells	Geometric
Perfect conductors modeling	Available	Available	Available
Dielectrics modeling	External models	Available	Not widely covered
Imperfect conductors modeling	Unavailable	Available	Unavailable
Same method for all structures	Yes	Yes	No
Impedance calculation	Available	Available	Unavailable
Matrices manipulation	Excessive	None	Almost none
Memory usage	Intensive	Intensive	Minimal
untime	Depends on the integral equation of the structure surface.	$O(N^3)$ in 2D [41]	Depends on the details of the tracing environment, tracing depth, and number of rays.
Accuracy	Best	Accurate	Accurate

Table 8.1: Comparison of electromagnetic modeling techniques.

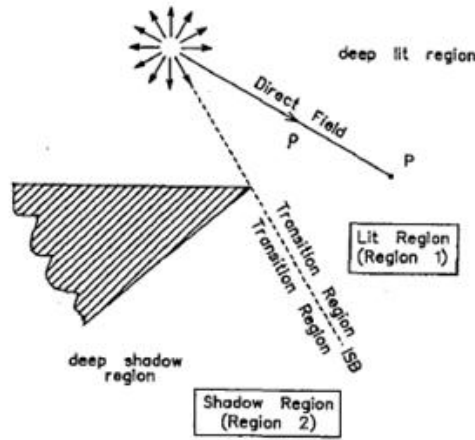


Figure 8.3: Creation of an incident shadow boundary.

8.2 Wedge Diffraction

8.2.1 Diffraction Model

A shadow region is the area that a GO ray can't reach due to the presence of obstacles in its path. A shadow boundary is a boundary that defines the shadow region.

There are two kinds of shadow regions [27]:

1. Shadow region for direct rays

It is the area that no direct rays can reach. The shadow boundaries associated with this kind of shadow region are called incident shadow boundaries (ISB).

1. Shadow region for reflected rays

It is the area that no reflected rays can reach. The shadow boundaries associated with this kind of shadow region are called reflected shadow boundaries (RSB).

The electric fields originating in the shadow regions are due to the diffraction of rays at different wedges along their paths. The GO fails to predict the electric fields at these regions. The GO electric field falls to zero in shadow regions, a thing that cannot occur in nature. Electric fields should vary smoothly and continuously at all regions.

Electric field at observation points in region 1 will compose of direct, reflected and diffracted electric fields. While electric field at observation points

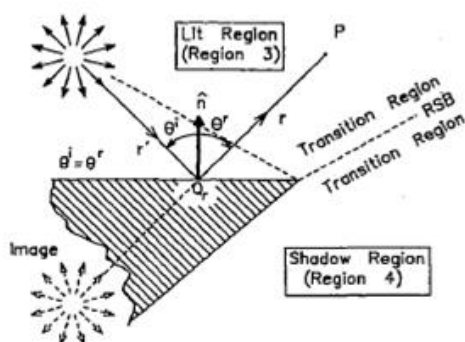


Figure 8.4: Creation of a reflected shadow boundary.

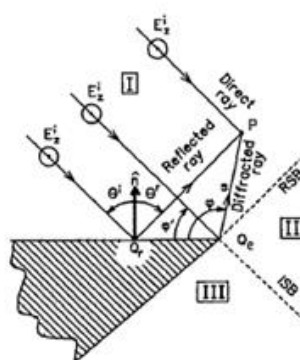


Figure 8.5: Different regions in the vicinity of a wedge.

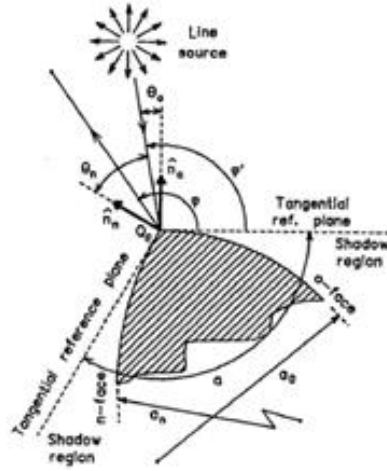


Figure 8.6: Wedge with curved faces.

in region 2 will compose of direct and diffracted electric fields. Finally electric field at observation points in region 3 will compose of diffracted electric fields only.

Thus it is essential to study the effect of waves' diffraction to obtain accurate electric fields in shadow regions. Our model uses the Uniform Geometrical Theory of Diffraction (UTD) to study wedge diffraction. UTD is used rather than GTD because the GTD fails to predict electric fields in transitions regions across the shadow boundaries. UTD assumed the wedges to be PEC surfaces, an assumption that is impractical for typical 3D environment. Several heuristic extensions have been made to UTD to allow the approximate treatment of non-PEC wedge diffraction. One of these heuristics is provided after the illustration of the UTD solution to PEC wedge diffraction.

Geometry of a Wedge

A wedge consists of two faces, O-face and N-face, and an edge. Each face has unit tangent and normal vectors. Tangents are directed away from the edge while normals are directed towards the outside of the wedge. The inner angle of the wedge is α .

Law of Diffraction

Keller's law of diffraction states that:

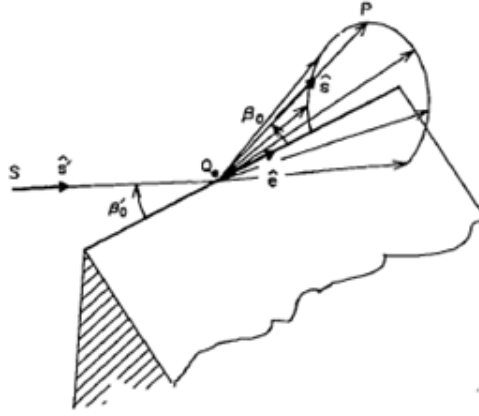


Figure 8.7: Cone of diffracted rays.

A diffracted ray and the corresponding incident ray make equal angles with the edge at the point of diffraction, provided they are in the same medium. They lie on opposite sides of the plane normal to the edge at the point of diffraction.

$$\sin \beta_0 = \left| \hat{s}' \times \hat{e} \right| = \left| \hat{s} \times \hat{e} \right| \quad (8.1)$$

Where:

\hat{s}' is the direction of the incident ray.

\hat{s} is the direction of the diffracted ray.

\hat{e} is the direction of the wedge's edge.

β_0 is the angle between the edge and the diffracted ray.

The plane of incidence is defined by \hat{s}' and \hat{e} , while the plane of diffraction is defined by \hat{s} and \hat{e} .

Edge-Fixed Coordinates

Similar to ray-fixed coordinates, the incident electric field is resolved into two components parallel ($\hat{\beta}_0$) and perpendicular ($\hat{\varphi}'$) to the plane of incidence.

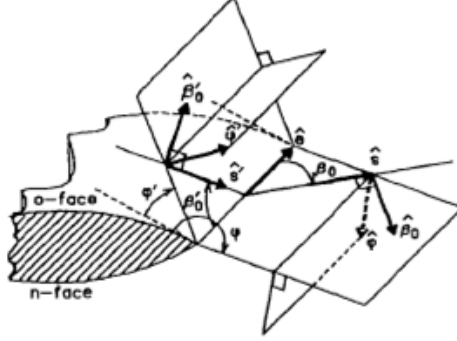


Figure 8.8: Edge-Fixed coordinate system.

The diffracted electric field is also resolved into two components parallel ($\widehat{\beta}$) and perpendicular ($\widehat{\varphi}$) to the plane of diffraction.

$$\widehat{\varphi}' = \frac{-\hat{e} \times \hat{s}'}{|\hat{e} \times \hat{s}'|} \quad (8.2)$$

$$\widehat{\beta}'_0 = \widehat{\varphi}' \times \hat{s}' \quad (8.3)$$

$$\widehat{\varphi} = \frac{\hat{e} \times \hat{s}}{|\hat{e} \times \hat{s}|} \quad (8.4)$$

$$\widehat{\beta}_0 = \widehat{\varphi} \times \hat{s} \quad (8.5)$$

The unit vector perpendicular to the edge in the plane of incidence is:

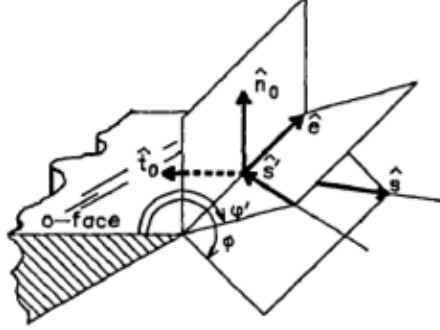
$$\hat{s}'_t = \frac{\hat{s}' - (\hat{s}' \cdot \hat{e}) \hat{e}}{|\hat{s}' - (\hat{s}' \cdot \hat{e}) \hat{e}|} \quad (8.6)$$

And the unit vector perpendicular to the edge in the plane of diffraction is:

$$\hat{s}_t = \frac{\hat{s} - (\hat{s} \cdot \hat{e}) \hat{e}}{|\hat{s} - (\hat{s} \cdot \hat{e}) \hat{e}|} \quad (8.7)$$

The angle φ' is given by:

$$\varphi' = \pi - \left[\pi - \cos^{-1} \left(-\hat{s}'_t \cdot \hat{t}_o \right) \right] \text{sgn} \left(-\hat{s}'_t \cdot \hat{n}_o \right) \quad (8.8)$$

Figure 8.9: Normal and tangential unit vectors on the o -face of a wedge

And the angle φ is given by

$$\varphi = \pi - \left[\pi - \cos^{-1}(\hat{s}_t \cdot \hat{t}_o) \right] \text{sgn}(\hat{s}_t \cdot \hat{n}_o) \quad (8.9)$$

Where:

$$\text{sgn}(x) = \begin{cases} -1 & \text{if } x < 0 \\ 1 & \text{if } x \geq 0 \end{cases} \quad (8.10)$$

The parameter n is related to the wedge angle α by

$$\alpha = (2 - n)\pi \quad (8.11)$$

Diffracted Electric Field

The incident electric field can be expressed as:

$$E^i = E_{\beta'_o}^i \hat{\beta}'_0 + E_{\varphi'}^i \hat{\varphi}' \quad (8.12)$$

And the diffracted electric field can be expressed as:

$$E^d = E_{\beta_0}^d \hat{\beta}_0 + E_{\varphi}^d \hat{\varphi} \quad (8.13)$$

Using matrix notation:

$$E^i = \begin{bmatrix} E_{\beta'_o}^i \\ E_{\varphi'}^i \end{bmatrix} \quad (8.14)$$

$$E^d = \begin{bmatrix} E_{\beta_0}^d \\ E_{\varphi}^d \end{bmatrix} \quad (8.15)$$

The diffracted electric field at a distance s on the path of the diffracted ray is given by:

$$E^d = D.E^i.A(s)e^{-jks} \quad (8.16)$$

Where :

D is the UTD diffraction coefficient

$$D = \begin{bmatrix} -D_s & 0 \\ 0 & -D_h \end{bmatrix} \quad (8.17)$$

$A(s)$ is the spreading factor defined by:

$$A(s) = \sqrt{\frac{\rho}{s(\rho + s)}} \quad (8.18)$$

Where ρ is the radius of curvature of the incident ray tube at the point of intersection with the edge.

UTD Diffraction Coefficients for PEC wedges

$$D_{s,h} \left(L^i, L^{ro}, L^{rn}, \varphi, \varphi', \beta_0, n \right) = D_1 + D_2 + R_{s,h}(D_3 + D_4) \quad (8.19)$$

Where $R_{s,h}$ are the reflection coefficients of the wedge at the edge. For a PEC surface $R_s = -1$ and $R_h = 1$.

The components of the diffraction coefficients are given by

$$D_1 = \frac{-e^{-j\frac{\pi}{4}}}{2n\sqrt{2\pi k}\sin\beta_0} \cot \left[\frac{\pi + (\varphi - \varphi')}{2n} \right] F \left[kL^i a^+(\varphi - \varphi') \right] \quad (8.20)$$

$$D_2 = \frac{-e^{-j\frac{\pi}{4}}}{2n\sqrt{2\pi k}\sin\beta_0} \cot \left[\frac{\pi - (\varphi - \varphi')}{2n} \right] F \left[kL^i a^-(\varphi - \varphi') \right] \quad (8.21)$$

$$D_3 = \frac{-e^{-j\frac{\pi}{4}}}{2n\sqrt{2\pi k}\sin\beta_0} \cot \left[\frac{\pi + (\varphi + \varphi')}{2n} \right] F \left[kL^{rn} a^+(\varphi + \varphi') \right] \quad (8.22)$$

$$D_4 = \frac{-e^{-j\frac{\pi}{4}}}{2n\sqrt{2\pi k}\sin\beta_0} \cot\left[\frac{\pi - (\varphi + \varphi')}{2n}\right] F\left[kL^{ro}a^-(\varphi + \varphi')\right] \quad (8.23)$$

The functions a^\pm are defined as:

$$a^\pm(\beta^\pm) = 2\cos^2\left(\frac{2n\pi N^\pm - \beta^\pm}{2}\right) \quad (8.24)$$

Where:

$$\beta^\pm = \varphi \pm \varphi' \quad (8.25)$$

And the integers N^\pm are the integers that most nearly satisfy the equations

$$2n\pi N^+ - \beta^\pm = \pi \quad (8.26)$$

$$2n\pi N^- - \beta^\pm = -\pi \quad (8.27)$$

L_i , L_{ro} , and L_{rn} are called distance parameters and they are associated with the incident and reflected shadow boundaries. Assuming incident spherical wave ray tubes, the distance parameters are calculated as follows:

$$L^i = \frac{s\rho}{s + \rho} \sin^2\beta_0 \quad (8.28)$$

$$L^{ro,n} = \frac{s\rho}{(\rho + s)} \sin^2\beta_0 \quad (8.29)$$

Where ρ is the principal radius of curvature of the incident ray tube at the point of intersection with the edge.

$F(x)$ is the transition function used by the UTD to cause the electric field to change continuously across the transition region surrounding the shadow boundaries.

UTD Diffraction Coefficients for non-PEC wedges

For a non PEC surface, the equation of the diffraction coefficients become [31]:

$$D_s \left(L^i, L^{ro}, L^{rn}, \varphi, \varphi', \beta_0, n \right) = D_1 + D_2 + \Gamma_{\parallel}^n D_3 + \Gamma_{\parallel}^o D_4 \quad (8.30)$$

$$D_h \left(L^i, L^{ro}, L^{rn}, \varphi, \varphi', \beta_0, n \right) = D_1 + D_2 + \Gamma_{\perp}^n D_3 + \Gamma_{\perp}^o D_4 \quad (8.31)$$

Where:

Γ_{\parallel}^n is Fresnel's reflection coefficient for parallel polarization of the n-Face.

Γ_{\parallel}^o is Fresnel's reflection coefficient for parallel polarization of the o-Face.

Γ_{\perp}^n is Fresnel's reflection coefficient for perpendicular polarization of the n-Face.

Γ_{\perp}^o is Fresnel's reflection coefficient for perpendicular polarization of the o-Face.

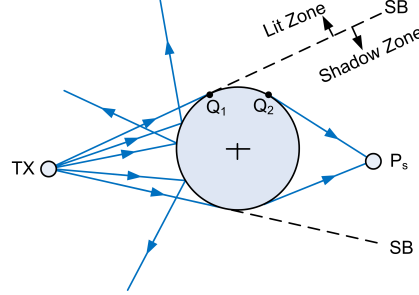


Figure 8.10: Geometrical configuration of the human shadowing problem.

8.3 Human Shadowing

In DfP, the relation between signal strength and distance is captured in a radio map. The radio map stores information about signal strength from different streams at different locations in the area of interest [4]. The radio map can be constructed either manually, that's by profiling the area by recording signal samples at each location, or automatically by simulating signal propagation in the environment.

In order to predict the human body-scattering effects in the indoor environment, a UTD-based propagation model is used. In the model, the human body is approximated with a perfect conducting circular cylinder of [42] radius 0.15 m, and height of 2 m. At microwave frequencies and higher, the human body constitutes a perfectly conducting and impassible reflector for electromagnetic waves [42].

In this section, we are going to explain the modeling concept of the human body-scattering effects using UTD.

8.3.1 Geometrical Configuration

An incident ray on a cylindrical surface may be either reflected or diffracted, according to the location of intersection between the ray and the cylindrical surface. A ray that falls tangential to the cylinder grazes the surface in the same plane of incidence. An extension of the incident ray beyond the point of grazing at the convex surface of the cylinder defines the Shadow Boundary (SB), which splits the space outside the surface into the lit and shadow regions [27].

Regions in the vicinity of the shadow boundary are called the transition regions. It is at the transition regions where the GO and GTD model fails as the incident field drops to zero, and the predicted field becomes infinite, and thus UTD was introduced [27]. Reflected rays from the cylinder falls in

the lit region, while grazing rays detach from the surface into diffracted rays and fall in the shadow zone, which is the non-illuminated exterior region of the cylinder. A grazing ray path is determined by the shortest distance from the ray source to an observation point P_s , and creeping on the cylindrical surface [27].

8.3.2 Reflection Off a Cylindrical Surface

Reflected Field

The UTD expression of the field reflected off a cylindrical surface from an incident electric field is given by [27]:

$$E^r(p) = E^i(Q_r) \cdot R_{s,h} \cdot A(s) \cdot e^{-jks^r} \quad (8.32)$$

Where:

$E^i(Q_r)$ is the electric field incident to the cylinder at Q_r .

$R_{s,h}$ are the soft and hard UTD reflection coefficients.

$A(s)$ is the 3-D spreading factor of reflection.

e^{-jks^r} is the phase shift of the reflected field.

s^r is the distance between reflection point and observation point.

UTD Reflection Coefficients

The soft and hard reflection coefficients are calculated from the following expression [27]:

$$R_{s,h} = -\sqrt{\frac{-4}{\xi}} \cdot e^{-j\pi/4} \cdot e^{-j\xi^3/12} \left[\frac{-F(X_p)}{2\xi\sqrt{\pi}} + \left\{ \begin{array}{c} p^*(\xi) \\ q^*(\xi) \end{array} \right\} \right] \quad (8.33)$$

Where:

$p^*(\xi)$ and $q^*(\xi)$ are the soft and hard Fock scattering functions.

$F(X_p)$ is the UTD reflection transition function which ensures that fields surrounding the transition regions remains bounded.

$X_p (\geq 0)$ is the transition function parameter, which is defined from [43]:

$$X_p = 2kL_p \cos^2(\theta^i) \quad (8.34)$$

$\xi (\leq 0)$ is the Fock parameter. It is defined from [43]:

$$\xi = -2m(Q_r) \cos(\theta^i) \quad (8.35)$$

$m(Q_r)$ is the curvature parameter at the reflection point. It is calculated as [27]:

$$m(Q_r) = \left[\frac{ka_t(Q_r)}{2} \right]^{1/3} \quad (8.36)$$

Where $a_t(Q_r)$ is the radius of curvature of the surface in the plane of incidence at Q_r .

Note that both the transition and the Fock scattering functions are computationally expensive. Computation-friendly expressions to calculate them can be found in [27], and [44]¹.

The 3-D Distance Parameter

L_p is the 3-D distance parameter, which is calculated from [43]:

$$L_p = \frac{\rho_1^i \rho_2^i}{(\rho_1^i + s^r)(\rho_2^i + s^r)} \cdot \frac{s^r(\rho_2^r + s^r)}{\rho_2^r} \quad (8.37)$$

Where:

ρ_1^i (ρ_2^i) is the radius of curvature of the incident wave in (transverse to) the plane of incidence.

ρ_2^r is the radius of curvature of the reflected wave transverse to the plane of reflection.

¹ At the time of writing this document, we could not reach the cited reference and we had to make our own assumptions to compute the Fock scattering functions.

Computing the Reflected Wave Radii

In our implementation, waves are assumed to be spherical. In that case, $\rho_1^i = \rho_2^i = s^i$ where s^i is the total unfolded distance from the transmitter to the point of reflection. The reflected wavefront radii of curvature are calculated from [27]:

$$\frac{1}{\rho_{1,2}^r} = \frac{1}{s^i} + \frac{1}{f_{1,2}} \quad (8.38)$$

Where:

$$f_{1,2} = \frac{1}{\cos(\theta^i)} \left[\frac{\sin^2(\theta_2)}{a_1} + \frac{\sin^2(\theta_1)}{a_2} \right] \pm \left[\frac{1}{\cos^2(\theta^i)} \left(\frac{\sin^2(\theta_2)}{a_1} + \frac{\sin^2(\theta_1)}{a_2} \right) - \frac{4}{a_1 a_2} \right]^{1/2} \quad (8.39)$$

The terms a_1 and a_2 are the principal radii of curvature of the surface at the incidence point. They measure how the surface bends by different amounts in different directions at a given point. In the case of a circular cylinder, $a_1 = \text{radius}$ and $a_2 = \text{infinity}$, hence the previous expression reduces to:

$$f_{1,2} = \frac{1}{\cos(\theta^i)} \left[\frac{\sin^2(\theta_2)}{a_1} \right] \pm \left[\frac{1}{\cos^2(\theta^i)} \left(\frac{\sin^2(\theta_2)}{a_1} \right) \right]^{1/2} \quad (8.40)$$

The quantities $\sin^2(\theta_1)$ and $\sin^2(\theta_2)$ are calculated from [27]:

$$\sin^2(\theta_1) = \cos^2(\alpha) + \sin^2(\alpha) \cos^2(\theta^i) \quad (8.41)$$

$$\sin^2(\theta_2) = \sin^2(\alpha) + \cos^2(\alpha) \cos^2(\theta^i) \quad (8.42)$$

Where α is the angle between the principal plane of the surface at the point of incidence and the plane of incidence as shown in Figure 8.11.

The value of α is calculated from [43]:

$$t_1 = -\hat{s}^i \cdot \hat{U}_1 \quad (8.43)$$

$$t_2 = -\hat{s}^i \cdot \hat{U}_2 \quad (8.44)$$

$$\alpha = \left| \tan^{-1} \frac{t_1}{t_2} \right| \quad (8.45)$$

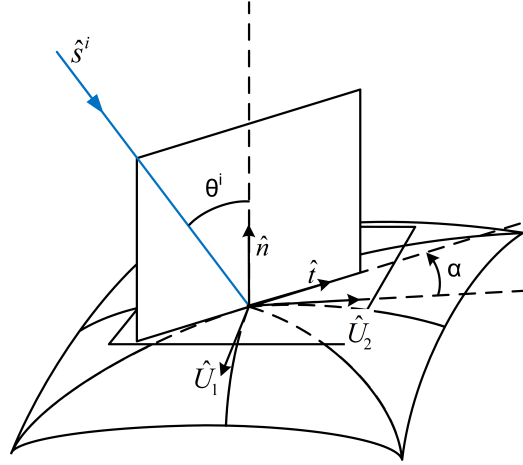


Figure 8.11: Principal directions at the point of incidence.

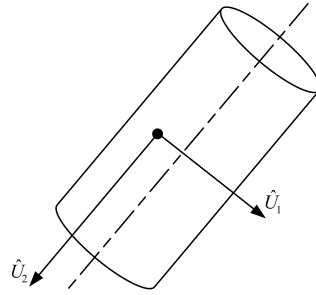


Figure 8.12: Principal directions at the point of incidence of a cylindrical surface.

Where \hat{U}_1 and \hat{U}_2 are the principal directions of the surface at the point of incidence. In the case of a cylindrical surface, \hat{U}_2 is parallel to the cylinder generator, and \hat{U}_1 is perpendicular to \hat{U}_2 , as shown in Figure 8.12.

Finally, the reflected spherical wave front radii are calculated as:

$$\rho_{1,2}^r = \frac{\rho_1^r + \rho_2^r}{2} \quad (8.46)$$

The 3-D Spreading Factor of Reflection

When an incident field reflects from a cylindrical surface, the reflected field amplitude varies from that of the incident field. The 3-D spreading factor governs the amplitude variation of the reflected field in 3D. It is calculated

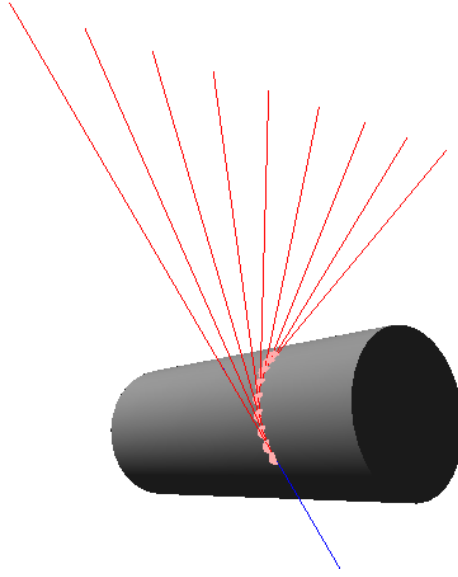


Figure 8.13: Diffraction by Sampling the Shadow Region in the Plane of Incidence.

from [43]:

$$A(s) = \sqrt{\frac{\rho_1^r \rho_2^r}{(\rho_1^r + s^r)(\rho_2^r + s^r)}} \quad (8.47)$$

8.3.3 Diffraction Off a Cylindrical Surface

An incident tangential ray at Q_1 creeps the cylinder surface and detaches at Q_2 . The location of Q_2 depends on the location of the observation point so that the total distance from the point of incidence to the observation point, including the creeping distance, is minimal.

In our implementation, the shadow region is sampled into observation points, and then the minimum tangential distance (in the plane of incidence) from each observation point to the cylinder is computed, and Q_2 is determined. The following figure illustrates a set of diffracted rays from a tangential incident ray to the cylinder:

After computing the diffracted rays origins and directions, the UTD diffraction model is applied, which we will address in the following subsections.

The UTD Equation

The field diffracted from a cylindrical surface is given by [43]:

$$E^d(p) = E^i(Q_1) \cdot T_{s,h} \cdot EC \cdot A(s) \cdot e^{-jks^r} \quad (8.48)$$

Where:

$E^i(Q_1)$ is the incident field on the cylinder at Q_1 .

$T_{s,h}$ are the soft and hard UTD diffraction coefficient.

$A(s) = \sqrt{\frac{\rho_2^r}{s^r(\rho_2^r + s^r)}}$ is the 3-D spreading factor of diffraction.

$EC = \sqrt{\frac{\rho_2^i}{\rho_2^i + t}}$ is the conservation of energy term in the case of spherical waves, where t is the creep distance along the surface from Q_1 to Q_2 .

The UTD Diffraction Coefficients

The soft and hard UTD diffraction coefficients are given by [43]:

$$T_{s,h} = -\sqrt{m(Q_1)m(Q_2)} \cdot \sqrt{\frac{2}{k}} \cdot e^{-j\pi/4} \cdot e^{-jk} \left[\frac{-F(X_d)}{2\xi\sqrt{\pi}} + \left\{ \begin{array}{c} p^*(\xi) \\ q^*(\xi) \end{array} \right\} \right] \quad (8.49)$$

Where:

$F(X_d)$ is the diffraction transition function.

$X_d = \frac{kL_d\xi^2}{2m(Q_1)m(Q_2)}$ is the transition function argument.

L_d is the 3-D distance parameter.

$\xi = \int_t \frac{m(Q_t)}{a_t}$ is the Fock parameter.

Transition and Fock functions are computed as described in the previous section.

Computing the Diffracted Wave Radii

The two radii of curvature of the diffracted wave at the observation point are calculated from [43]:

$$\rho_1^r = \rho_b^i + s^r + t\rho_2^r = s^r \quad (8.50)$$

Where:

t is the creeping distance.

s^r is the distance between the observation point and the detachment point Q_2 .

ρ_b^i is the radius of curvature of the incident wave in the plane transverse to the incident plane, which is calculated from [43]:

$$\frac{1}{\rho_b^i} = \frac{\sin^2(\alpha)}{\rho_1^i} + \frac{\cos^2(\alpha)}{\rho_2^i} \quad (8.51)$$

As we assume spherical waves, that is $\rho_1^i = \rho_2^i = s^i$, the previous equation reduces to:

$$\rho_b^i = \rho_1^i = \rho_2^i \quad (8.52)$$

The final radii of curvature of the diffracted ray are then calculated as the avg. of its two radii of curvature.

Chapter 9

Validation

9.1 Experiment Design

Modeling results were compared with empirical measurements to validate the modeling technique. The experiment was conducted in a typical environment, where obstacles such as furniture participate in the RF propagation. Figure 9.1 illustrates the layout of the experiment environment.

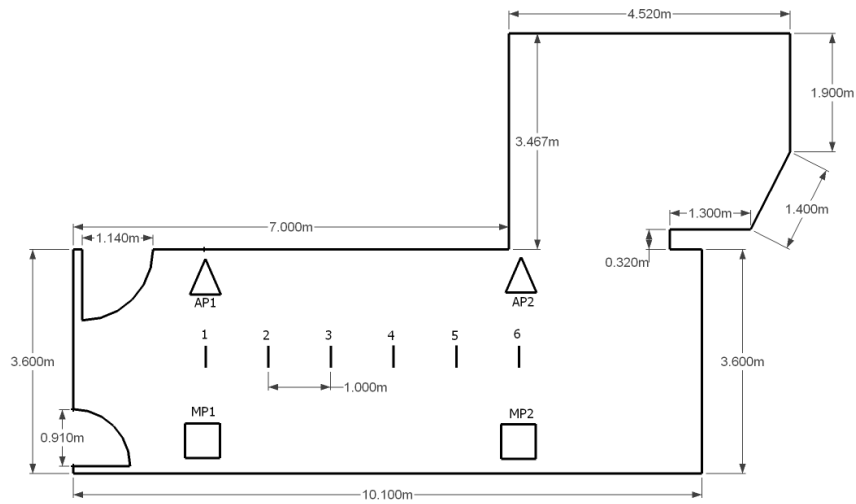


Figure 9.1: Environment layout of the conducted experiment.

All access points (AP) and monitoring points (MP) are placed at a height of 60 cm. The environment has many materials such as walls, concrete, wood, and glass. A refractive index for each material at microwave frequency was used in the simulation. Also, the same AP and MP configurations are used in the simulation, yet both the transmitters and receivers antennas are assumed

to be isotropic. A human was positioned at each of the indicated locations, 1 to 6.

9.2 Validation Results

The measured vs. simulated results are illustrated in figures 9.2, and 9.3.

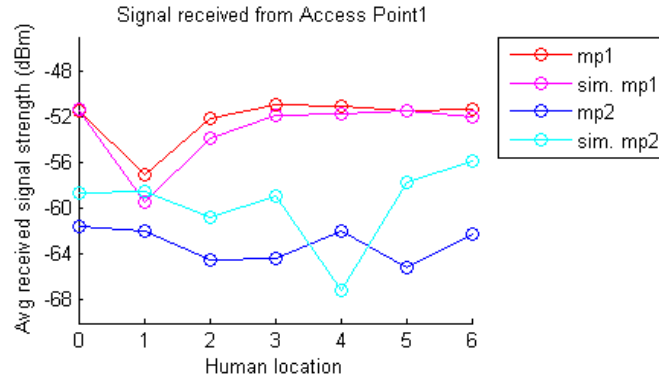


Figure 9.2: Signal received from AP1

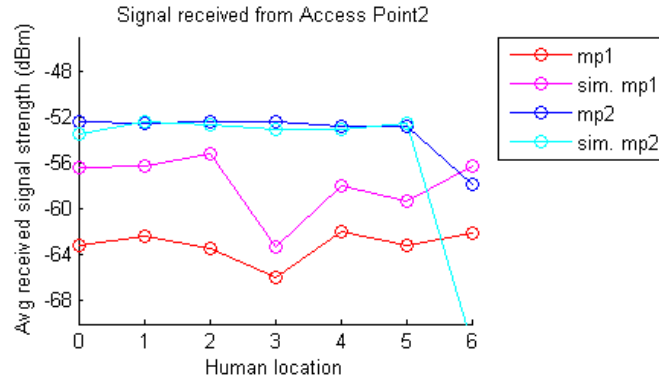


Figure 9.3: Signal received from AP2

Note that location 0 describes the received signal strength in the absence of the human body.

Table 9.2 summarizes the correlation coefficient and the RMSE of each MP-AP pair.

Comparison between measured and simulated results shows that at the simulated results, in general, compares favorably with measurements. At shorter distances between a receiver and a transmitter, the predicted values

		AP1	AP2
MP1	Corr.	0.9819	0.7689
	RMSE	1.2	5.6
MP2	Corr.	-0.1712	0.9928
	RMSE	5.17	5.3

Table 9.1: Measured vs. Simulated Results

are real close to measured values. At longer distances, the difference between predicted and measured values increases. At some locations (such as location 4) predicted values are not representative of reality.

Differences between measured and simulated results can be due to the following:

1. Level of details of the environment model. As the experiment environment had a lot of obstacles and furniture which were not taken into account by the 3D model that was used in the simulation.
2. UTD assumes diffraction off perfect conductors, yet the environment had much of dielectrics.
3. The direction of transmitters and receivers antennas.
4. Orientation of the human body at the time of the experiment.
5. Operating power and gain configurations of each antenna may differ from what is stated in their datasheets.
6. The missing region of the Fock scattering function affects the UTD model one way or another. We could not quantify that effect, though.
7. Refractive indices of the materials may not be representative of reality.

Part IV

The DFP System

Chapter 10

The *DfP* System

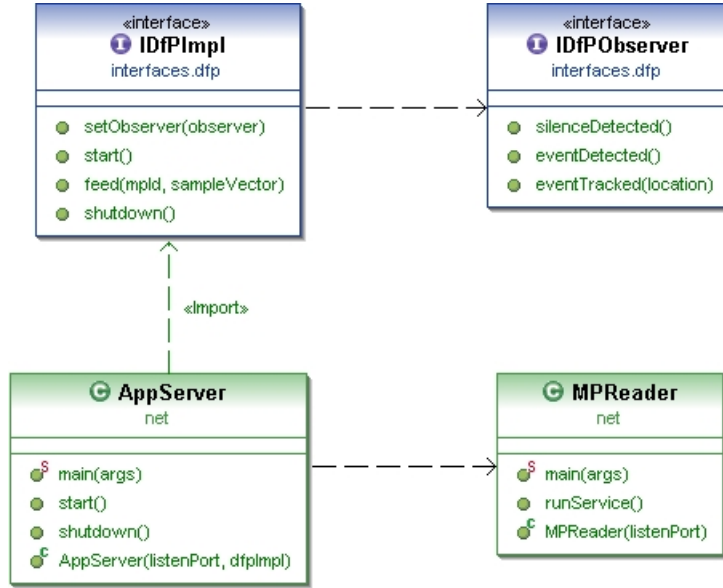
In this chapter, we describe the design we used to realize our *DfP* system. Then, we describe the operation of the implemented *DfP* system.

10.1 System Architecture

The design we present realizes all the techniques we discussed in the previous chapters. First, we present the architecture of the *DfP* system. Second, we describe how the data is represented and stored. Third, we describe the test architecture we used to evaluate the performance of the proposed techniques. Finally, we describe the implementation of the tracking and detection algorithms, in addition to the site planning and RF prediction techniques.

10.1.1 High Level Components

Figure 10.1 illustrates the main components of the *DfP* system. Each MP starts an instance of the *MPServer* and waits for requests. The AS starts an instance of the *AppServer* and periodically requests each MP to perform a scan and return the collected signals. The AS feeds these scans to an instance of the *IDfPImpl* interface that implements the required DfP functionalities. This object is responsible for running the required algorithms and updating an instance of *IDfPObserver* with the current state of the system. For example, in an intrusion detection application, the observer can be alerted if an intruder was detected inside the area of interest. Another example, in a smart home scenario, the observer would receive updates of the current user location which can be used for providing a variety of services such as light and temperature control.

Figure 10.1: Main components of the *DfP* system.

10.1.2 Data Representation, Acquisition and Storage

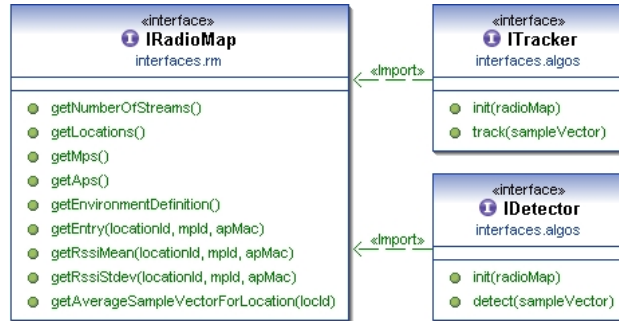


Figure 10.2: Radio-map is used by all algorithms.

Radio maps are the unified data container for the whole *DfP* system. The radio map defines a standard interface for retrieving information about the underlying environment. This information is organized into a three dimensional table-like structure that maps each tuple of $(location, MP, AP)$ to the corresponding entry. There is no restriction on the contents of these entries. Each algorithm will require specific information in order to operate. A radio map is created and filled with the required information and passed to the algorithm before it can be used. Figure 10.2 illustrates the *IRadioMap* interface and how the algorithms access the required information through the

exposed methods. Figure 10.3 shows the different types of radio map entries available in the current implementation.

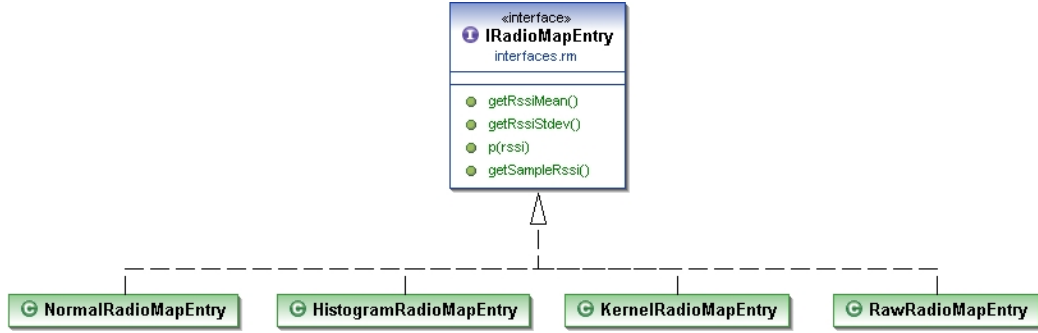


Figure 10.3: The different types of radio-map entries.

Each MP performs an active scan operation to get the RSSI for each stream. These values are collected by the *AppServer* as we showed earlier.

A radio-map is stored in the file system in a certain directory structure that is described in the system documentation. All information about locations, MPs and APs is stored in addition to the radio-map entries. The system does not depend on the exact format or structure of this storage. The subroutines that store and read the radio map can easily be replaced as needed.

10.1.3 Tracking Algorithms

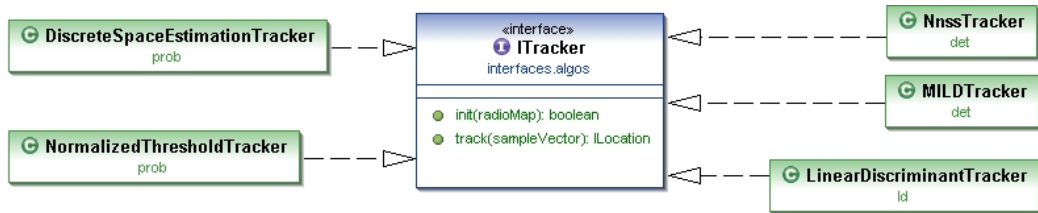


Figure 10.4: The implemented tracking algorithms i.e. trackers.

We implemented a variety of tracking algorithms. As explained in Chapter 3, a tracking algorithm is basically a classifier. All tracking algorithms implement the *ITracker* as shown in figure 10.4. A tracking algorithm is initialized with a radio-map. Given a sample vector that contains signal strength readings from each stream, the tracking algorithm matches this sample vector to a predefined radio-map location, which is then returned to the caller of the *track* method.

We implemented distance-based and probabilistic tracking algorithms. We describe each of these algorithms briefly:

1. *DiscreteSpaceEstimationTracker*

This method was explained in subsection 3.3.2.

2. *NormalizedThresholdTracker*

This method was explained in subsection 4.2.2.

3. *NnssTracker*

This method was explained in subsection 3.3.1.

4. *KNNTracker*

This method is explained in Appendix B.1.

5. *MILDTracker*

This method is explained in Appendix B.1.

6. *LinearDiscriminantTracker*

This method is explained in Appendix B.1.

10.1.4 Detection Algorithms

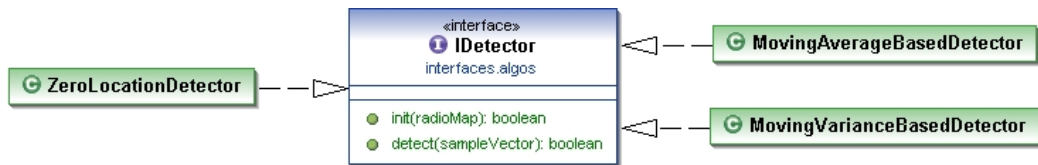


Figure 10.5: The implemented detection algorithms i.e. detectors.

As explained in Chapter 4, we consider two approaches to the detection problem: a signal processing based approach and a classification based approach. Both approaches were implemented through the following classes as illustrated in figure 10.5:

1. *MovingAverageBasedDetector*

This method was explained in [1].

2. *MovingVarianceBasedDetector*

This method was explained in [1].

3. *ZeroLocationDetector*

This method was explained in subsection 4.2.1.

An instance of *IDetector* is also initialized with a radio-map. Calling the *detect* method with a given input sample vector the algorithm returns *true* if an event was detected, other wise, the algorithm returns *false*.

10.1.5 Test Architecture

Our work relies heavily on testing. We collected a number of data sets to evaluate the performance of the different algorithms we propose. In order to support the required test tasks and enable great flexibility in designing and running complex tests, we designed and implemented the test architecture we describe next.

Test Interfaces

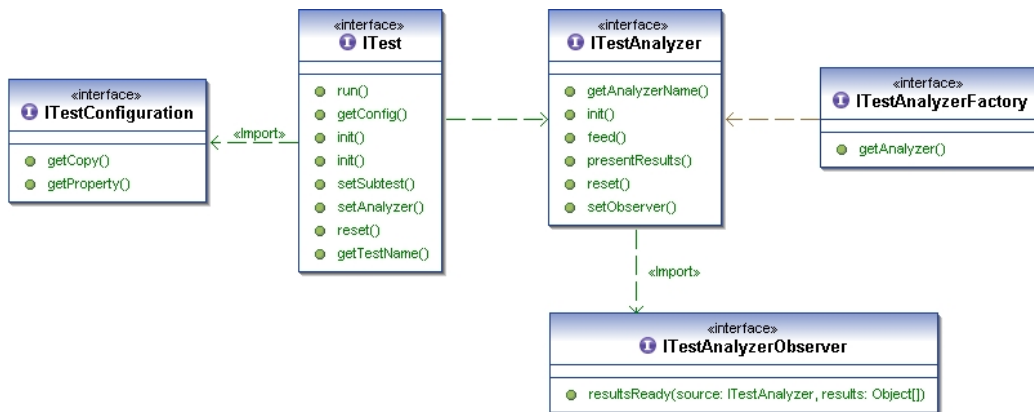


Figure 10.6: Test Interfaces

Figure 10.6 illustrates the test interfaces we use. These interfaces summarize the life cycle of all tests. Test objects that implement the *ITest*

interface use an instance of *ITestConfiguration* to store and manipulate their test configurations. The actual testing is performed at the test analyzer that implements the *ITestAnalyzer* interface. The test analyzer can access the test configuration of its parent test. When the test is initialized, it creates an instance of the desired analyzer through the *ITestAnalyzerFactory* in its configuration. When the test is started it feeds the analyzer with test sample vectors. The analyzer uses these sample vectors to run the algorithms it was designed to analyze. The analyzer processes the output of these algorithms and by the end of the test contains the results required for analyzing the performance of the algorithms in question. To allow for arbitrary processing of the final test results, the analyzer is passed an instance of *ITestAnalyzerObserver* that gets called when the test is over and allowed access to the analyzer result objects.

Basic Test Classes

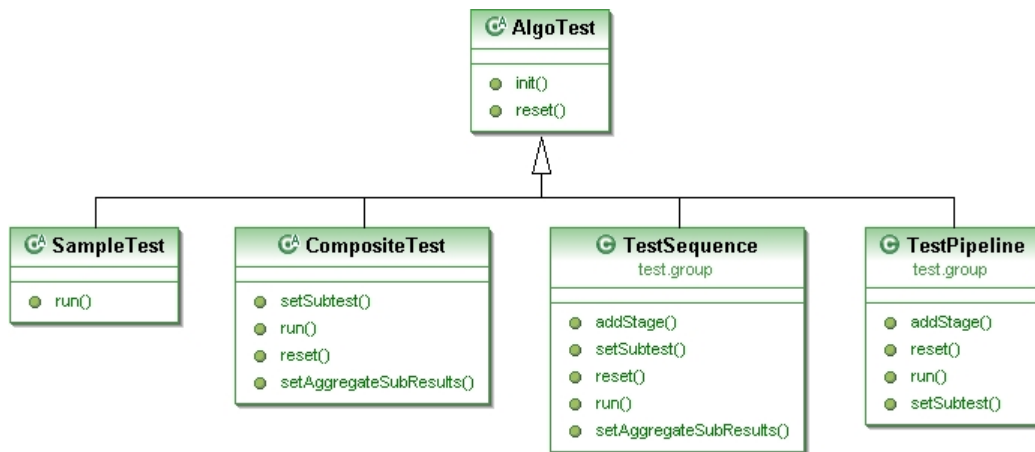


Figure 10.7: Basic Test Classes

To enable the creation and composition of complex test scenarios, the class hierarchy in figure 10.7 was designed. The class *AlgoTest* implements the basic and common test functionalities, like initializing the test, instantiating the analyzer, building the radio-maps and initializing the algorithms. Subclasses of *AlgoTest* move a step forward to specialize into four classes. Each of these subclasses is responsible for the following:

1. *SampleTest*

This class is responsible for generating the test sample vectors. It is

subclassed further to support the different methods of generating these test sample vectors as will be explained shortly.

2. *CompositeTest*

This class enables the composition of nested tests. Instances of these class have a subtest of type *ITest*. Their role is to manipulate the test configuration before running this subtest, which in turn might be a composite test too. Usually, the final level in the test hierarchy is an instance of one of the subclasses of *SampleTest*.

3. *TestSequence*

This class holds a number of *ITest* objects and runs them in sequence. A notable usage of this class is in the *RepeatedKFoldCrossValidationTest* which is essential when comparing algorithms.

4. *TestPipeline*

This class holds a number of *ITest* objects where the first test object is the parent of the next test object etc.

Sample Test Classes

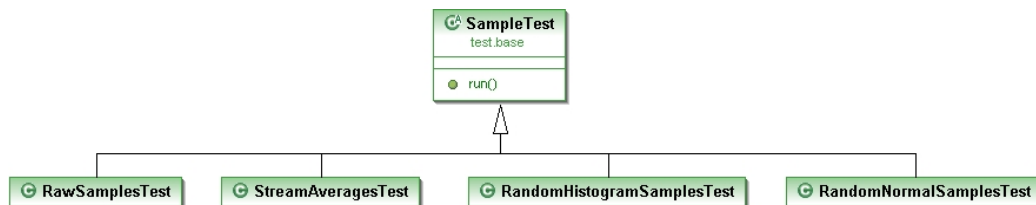


Figure 10.8: Sample Test Classes

As mentioned before, the *SampleTest* is responsible for the generation of the test sample vectors. It is subclassed to provide four method for generating these test sample vectors, as shown in figure 10.8. Each of these subclasses operates as follows:

1. *RawSamplesTest*

Creates test sample vectors from the samples recorded during the experiment.

2. *StreamAveragesTest*

Creates test sample vectors by averaging the sample values of each stream.

3. *RandomHistogramSamplesTest*

Generates a random test sample vector by generating a random value for each stream using the stored stream histogram.

4. *RandomNormalSamplesTest*

Generates a random test sample vector by generating a random value for each stream using the stored stream Gaussian distribution.

Composite Test Classes

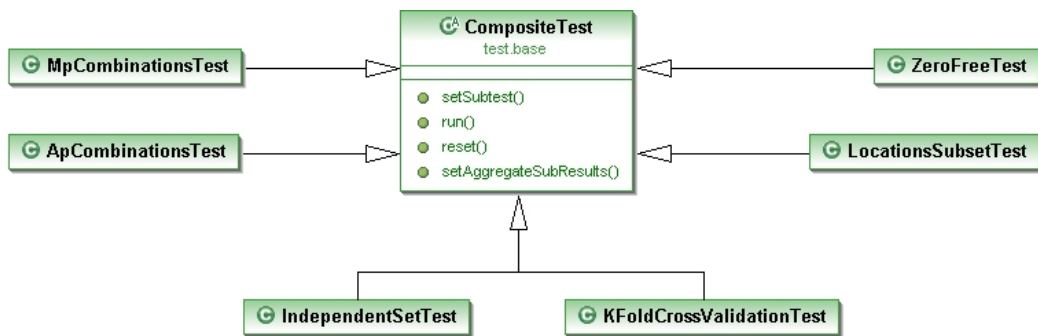


Figure 10.9: Composite Test Classes

Subclasses of *CompositeTest* implement various methods for manipulating test data, as shown in figure 10.9. Each of these subclasses manipulates the test data in the following way:

1. *MPCombinationsTest*

Manipulates the radio-map to simulate the effect of changing the streams being used by generating all combinations of MPs.

2. *APCombinationsTest*

Manipulates the radio-map to simulate the effect of changing the streams being used by generating all combinations of APs.

3. *ZeroFreeTest*

Manipulates the radio-map by removing location zero, i.e. the silence state. This was necessary to evaluate the performance of tracking algorithms given only the tracking problem, without mixing it with the detection problem.

4. *LocationSubsetTest*

Manipulates the radio-map to simulate the effect of changing the possible locations to include a specified set of locations.

5. *IndependentSetTest*

Trains the system using a data set then tests it with a different data set.

6. *KFoldCrossValidationTest*

Given a data set, this tests divides the data into k-folds then, each fold is used for testing and the remaining folds are used for training.

Test Analyzers

Numerous analyzers were implemented to collect different information about the tests being run. This is a brief description of the most frequently used analyzer:

1. *BinaryErrorAnalyzer*

Calculates the total error ratio.

2. *DistanceErrorAnalyzer*

Calculates the average distance error.

3. *DistanceErrorCdfAnalyzer*

Calculates the distance error CDF.

4. *LocationConfusionAnalyzer*

Creates a confusion matrix for true and predicted locations.

5. *DetectionConfusionAnalyzer*

Creates a confusion matrix for true and predicted event and silence states.

10.1.6 RF Prediction

The Transmitter and the Receiver classes extend `jme.scene.Sphere` class. Each transmitter contains a `TransmitterModel` object that encapsulates the functionality of a ray tracing source. Similarly, each receiver contains a `ReceiverModel` object that encapsulates the functionality of a ray tracing receive. Each transmitter or receiver model encapsulates an antenna object that stores all the properties of the antenna.

The Antenna class is abstract, the reason behind this to allow the definition of more types antennas while maintaining the same interface. At the moment, there are two types of antennas defined in the system, `IsotropicAntenna` and `HalfWaveDipoleAntenna`.

The `model.propagation` package contains the classes needed for modeling an electromagnetic wave. Two models are implemented, the power model and the electric field model.

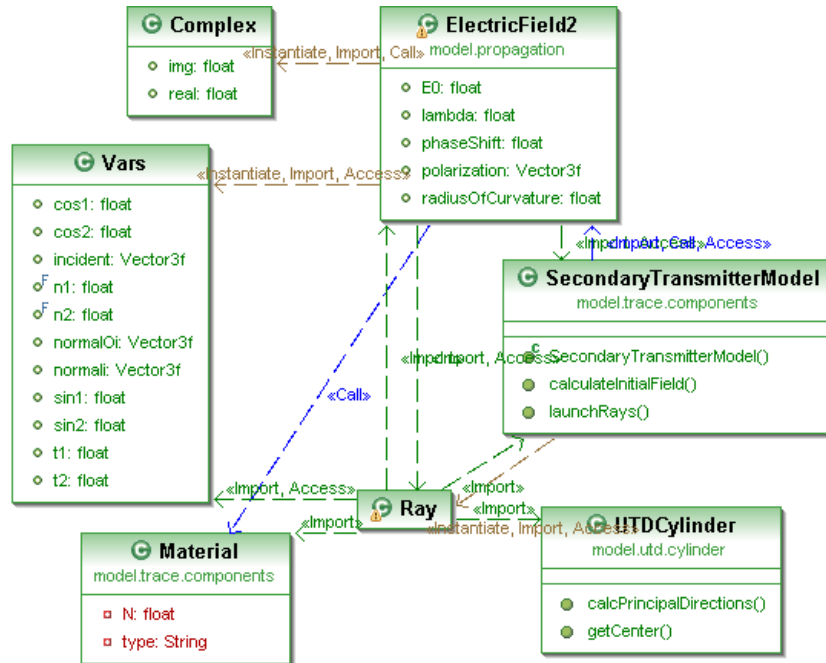


Figure 10.10: `model.math` associations.

The ElectricField2 class contains all the methods necessary for handling the electric field of a ray, like calculating the reflecting, transmitting and diffracting electric fields.

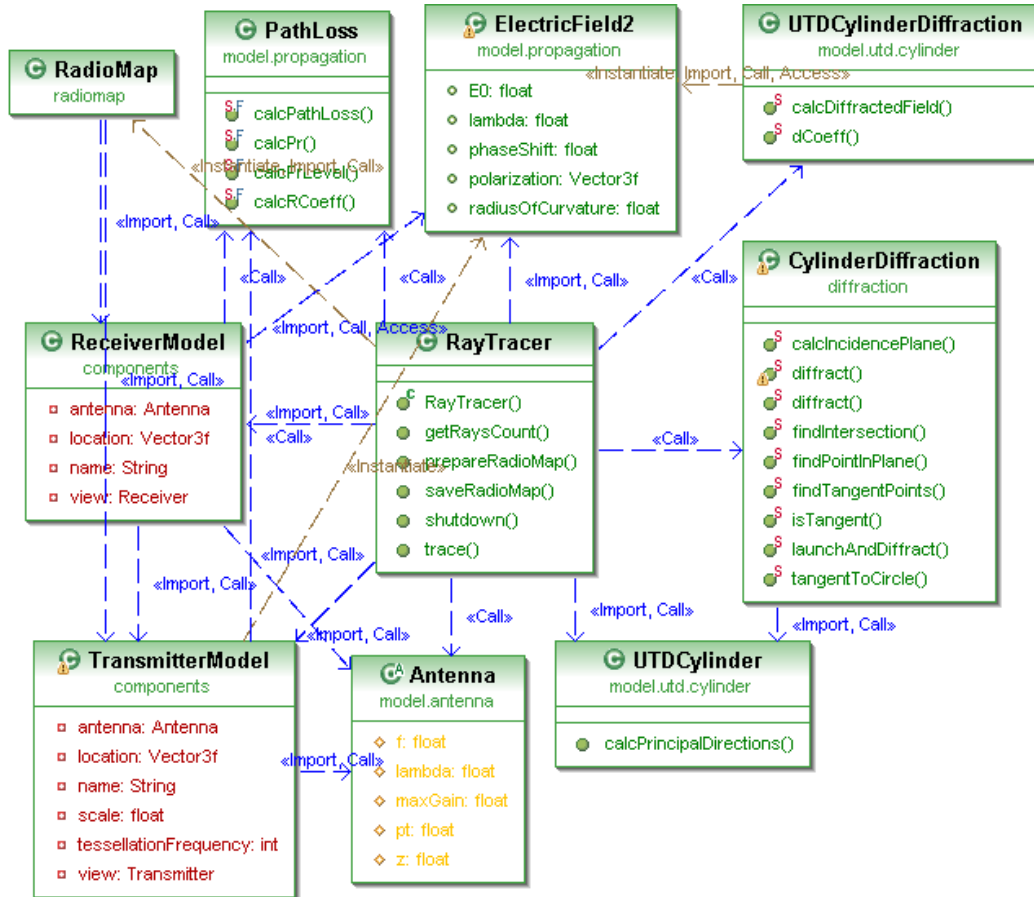


Figure 10.11: Ray Tracer.

The Ray class extends `jme.math.Ray` and adds ray tracing specific attributes and methods to it. These attributes includes, the reference electric field of the ray, the gain, and the power coefficient associated with the ray.

The RayTracer class performs the ray tracing algorithm. It is given a 3D model node, a set of TransmitterModels, and a set of RecieverModels. It runs the ray tracing algorithm and outputs the received signal strength at each of the receiver models.

10.2 System Operation

In this section, we summarize how the system operates both in the offline and online phases.

10.2.1 Offline Phase

In the offline phase, the *AppServer* constructs the radio map by collecting samples from the monitoring points. The *AppServer* has a location profile for each location where it stores the samples being collected for that location. The offline operation can be controlled by two parameters: number of samples per second and total number of samples required for each location. These samples are stored as described in 10.1.2.

When using RF prediction instead of the manual sampling the process should be much easier. First, the building model is acquired and entered to the program. Second, the radio-map locations are selected inside the tool. Finally, the RF prediction is performed and the generated radio-map is stored in the same format.

10.2.2 Online Phase

In the online phase, the *AppServer* collects RSSI readings from each MP and feed it to the *IDfPIimpl*. The *IDfPIimpl* is responsible for running the algorithms and updating the registered instance of *IDfPObserver* with the current state of the system.

Part V

Conclusions and Future Work

Chapter 11

Conclusions and Future Work

In this chapter, we summarize the results of our work in the *DfP* system. Then, we present the challenges that will be considered in the future.

11.1 Conclusions

Through our study of the *DfP* system, we have got to the following results:

- **Tracking:**

We presented deterministic and probabilistic *DfP* tracking algorithms and evaluated their accuracy. The results showed that the probabilistic techniques performed better than the deterministic one. They also showed that the non-parametric probabilistic technique performed better than the parametric one. Through experiments, we identified some of the challenges against the accuracy of *DfP* tracking systems in real environment like temporal variation and user orientation.

- **Detection:**

We presented two *DfP* detection algorithms: Location-Zero algorithm and Normalized Threshold algorithm. The first solves the problem as a classification problem by adding an entry for silence state to the radio map. The second puts some constraints on the results of the algorithms used for tracking. We evaluated the two algorithms through experiments. The results shows that Location-Zero algorithm acted better in the cross-validation case. However, in the case of an independent test set, both algorithms resulted in the same accuracy.

- **Site Planning:**

We studied the effect of site planning on both *DfP* detection and tracking. We presented a hypothesis about APs and MPs placement and

radio map location set selection in *DfP* environments to enhance the accuracy. We also presented an experimental study to validate the hypothesis. We argued that site planning affects the accuracy of the system significantly and showed the effect of different layouts on the accuracy of the *DfP* system.

- **Wave Propagation Prediction:**

Our objective was to construct a tool for RF prediction in the presence of human bodies in indoor environments. Our tool will be used in conjunction with the *DfP* system to generate the radio map required for the operation of the *DfP* system. Our model included the human shadowing effect that is required for the generation of the radio map. Also, the tool helps in quantifying the effect of multiple humans on the channel, something that is hard to be done empirically.

The results of our simulation compared favorably with measurement. The difference between the simulated and measured results is mainly due to the imperfect representation of the real environment by the 3D model. The accuracy of the tool has been demonstrated through this report, and we showed that received signal strength has been predicted with a RMSE of less than 6 dB over 6 locations.

11.2 Future Work

In this section, we present some possible plans for our future work:

- Studying large-scale deployments of the *DfP* system.
- Developing solutions for multi-person tracking and detection.
- Devising a robust method for APs and MPs placement in a *DfP* environment.
- Developing solutions against the problem of temporal variation.
- Support of wave propagation prediction in multi-floor buildings.
- Support of outdoor wave propagation prediction.
- Better handling of 3D models.
- Improving the accuracy of propagation prediction.
- Conducting more experiments in a large typical environment.

- Improving the user interface of the prediction tool to be more user-friendly.

Part VI

Appendices

Appendix A

IEEE 802.11

This appendix provides a brief overview of the IEEE 802.11 standard. We describe the physical and MAC (Medium Access Control) layers as defined by the IEEE 802.11 Standard. Then, we describe the extensions to the IEEE 802.11 Standard. We will not cover the security aspects of this protocol as it is currently not relevant to the study of the feasibility of *DfP* localization.

A.1 History of 802.11

In 1985, the Federal Communications Commission (FCC) authorizing the public use of the Industrial, Scientific, and Medical (ISM) bands, which spans frequencies between 902 MHz and 5.85 GHz, just above the cellular phone operating frequencies. This was the fundamental factor that led to the widespread of the 802.11 Wireless LANs, as it does not require any license. However, no standard was available at that time.

A couple of years later, the Institute of Electrical and Electronics Engineers, Inc. (IEEE) 802 working Group, which is responsible for the development of LAN standards, started developing standards for wireless LANs. The IEEE 802.11 Working Group developed the Wireless LAN Medium Access Control and Physical Layer specifications. The IEEE Standards Board approved the standard on June 26, 1997, and the standard was published on November 18, 1997.

A.2 802.11 WLANs

A typical 802.11 WLAN is composed of a number of wireless stations associated with Access Points (APs). This setup is called the infrastructure mode of operation. An AP is a special station that has two interfaces: one interface

on the WLAN and the other on a wired interface. The AP is responsible for bridging 802.11 frames from the WLAN, by changing packet headers, to the wired network and vice versa.

When a station first enters the area covered by a set of APs, it sends out probe messages. APs that cover the new area respond to this probe message, and the station decides to associate with one of these APs, based on factors such as signal strength and noise level. If the station is moved outside the area covered by its associated AP, it will send probe messages again to associate with a different AP in a procedure called a handoff. The 802.11 provides an ad-hoc mode that we will not cover here.

A.3 The Physical Layer

A communication channel is a range of electromagnetic frequencies over which data is transmitted. A carrier wave is used to carry the data through modulation. The modulated carrier is received and demodulated at the destination. IEEE 802.11 specifies a number of encoding schemes that support data rates of 1Mbps, 2Mbps, 5.5Mbps, and 11Mbps.

The carrier signal is spread across channels using specified techniques. The techniques employed in 802.11 are Direct Sequence Spread Spectrum (DSSS) and Frequency Hopping Spread Spectrum (FHSS). The first uses a single channel and spreads the carrier in one wide channel, while the second uses several channels for spreading the carrier signal. Spreading the signal provides a degree of immunity against jamming and decreases the error probability. The 802.11b standard, with high rates of 2Mbps and above, uses the DSSS exclusively, i.e. uses a single channel.

The 802.11 standard provides half duplex communication i.e. a station can only send or receive data at the any time. This allows the same hardware to switch between reception and transmission

A.4 The MAC Layer

The MAC protocol specifies when a station can access the medium to send data. The MAC protocol can run either a distributed algorithm or a centralized algorithm to decide who can send data. The 802.11 standard defines both centralized (Point Coordination Function) and distributed algorithms (Distributed Coordination Function) for medium access.

The PHY layer in an 802.11 station implements all the modulation, transmission, and carrier sensing. Carrier sensing reports to the MAC layer the

current state of the channel. The MAC uses this to decide when to send data. As the 802.11 allows only for half-duplex communication the medium access can only be controlled by collision avoidance (CSMA/CA).

A.5 802.11x

A.5.1 a

The 802.11a standard specifies operating in the 5GHz band using orthogonal frequency division multiplexing (OFDM). 802.11a supports data rates up to 54Mbps. It is also referred to as Wi-Fi5.

A.5.2 b

802.11b enhances the initial 802.11 DSSS PHY to include 5.5Mbps and 11Mbps data rates. This is possible through a more efficient use of the radio spectrum through a CCK (Complementary Code Keying) modulation. The majority WLAN deployments today comply with 802.11b, which is also the basis for WiFi certification from the Wireless Ethernet Compatibility Alliance (WECA).

A.5.3 c

802.11c enables proper bridge operations.

A.5.4 d

802.11d pays special attention to satisfying regulatory outside U.S., Europe, and Japan. This is especially important for operation in the 5GHz bands because the use of these frequencies differ widely from one country to another.

A.5.5 e

802.11e refines the 802.11 MAC to improve quality of service (QoS) to make it more suitable for audio and video applications.

A.5.6 f

802.11f specifies an inter access point protocol that provides the necessary information to support the 802.11 distribution system functions, e.g. roaming.

A.5.7 g

802.11g aims at developing a higher speed extension to the 802.11b PHY in the 2.4GHz band. The enhanced data rates are up to 54Mbps.

A.5.8 h

802.11h addresses the requirements of European regulatory. Mainly, it provides dynamic channel selection (DCS) and transmit power control (TPC) in the 5GHz band (802.11a). In Europe, 802.11a can interfere with satellite communications, which have *primary use* designations while most countries authorize WLANs for *secondary use* only. Through DCS and TPC, 802.11h can avoid interference in a way similar to HiperLAN/2, the European competitor to 802.11a.

A.5.9 i

802.11i enhances the security of the MAC Layer to compensate for the shortcomings of the WEP encryption protocol. 802.11i incorporates stronger encryption techniques, such as AES (Advanced Encryption Standard).

Appendix B

Tracking Performance For Different Classifiers

This appendix shows the tracking performance using other classifiers in addition to algorithms mentioned in Chapter 3.

B.1 Other Classifiers

1. KNN Classifier

This method stores all the training samples. Using *Euclidean Distance*, The input sample vector is compared to each of these stored samples to find the k -nearest neighbors. The input sample vector is matched to one of the locations using a majority vote algorithm. A simple majority vote algorithm returns the location with the highest number of samples in the k -nearest neighbors. A better majority vote algorithm would consider the distance between the input sample vector and the neighbor instead of only counting their number.

2. MICD Classifier

This method is similar to the NNSS tracking algorithm explained in 3.3.1. The only difference is that it uses the *Generalized-Euclidean or Mahalanobis Distance* instead of the *Euclidean Distance*. To calculate the generalized distance, the method considers the covariance between each pair of streams. Given k data streams, a $k \times k$ covariance matrix (S) stores the covariance between each pair (i, j) of these streams at $S_{i,j}$. The covariance matrix is symmetric and invertible. Given N

sample vectors (x_1, x_2, \dots, x_N) , the covariance matrix is calculated as:

$$m = \frac{1}{N} \sum_{i=1}^N x_i \quad (\text{B.1})$$

$$S = \frac{1}{(N-1)} \sum_{i=1}^N (x_i - m)(x_i - m)^T \quad (\text{B.2})$$

The equation for calculating the *Generalized-Euclidean Distance* between two vectors x_1 and x_2 is:

$$D(x_1, x_2) = ((x_1 - x_2)^T S^{-1} (x_1 - x_2))^{1/2} \quad (\text{B.3})$$

3. Linear Discriminant Classifier

We also implemented linear discriminants classifiers that can be trained using the Reward-Punishment Perceptron algorithm or the HoKashyap algorithm. However, due to the overlapped properties of locations in signal space, they are generally not linearly seperable. As a result, this classifier failed to perform well on this problem.

B.2 Comparing All Classifiers

The next table shows the tracking performance for different deterministic and probabilistic algorithms under 10-times repeated 10-fold cross-validation:

Algorithm	Average Distance Error	Error Probability
MED (NNSS) Classifier	0.214m	0.0874
MICD Classifier	0.258m	0.11
KNN Classifier (K=20)	0.37	0.16
Bayes Classifier (Gaussian Distribution)	0.201m	0.0835
Bayes Classifier (Histogram)	0.176m	0.0727
Bayes Classifier (Gaussian Kernel)	0.175m	0.0723

Table B.1: Cross-Validation tracking results for different classification algorithms for Experiment 1.

The above table shows that the probabilistic algorithms performed better than the other deterministic algorithms

Appendix C

Spherical Coordinates

“Spherical coordinates are a system of curvilinear coordinates that are natural for describing positions on a sphere.”

Define

1. ϑ to be the zenith angle measured from the z-axis, where

$$0 \leq \vartheta \leq \pi \quad (\text{C.1})$$

2. φ to be the azimuth angle in the x-y plane measured from the x-axis, where

$$0 \leq \varphi \leq 2\pi \quad (\text{C.2})$$

3. r to be the distance to the origin

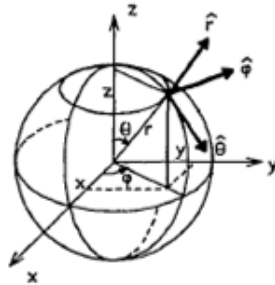


Figure C.1: Spherical Coordinates.

The spherical coordinates are related to the Cartesian coordinates by

$$r = \sqrt{x^2 + y^2 + z^2} \quad (\text{C.3})$$

$$\theta = \cos^{-1}(z/r) \quad (\text{C.4})$$

$$\varphi = \tan^{-1}(y/z) \quad (\text{C.5})$$

The three perpendicular unit vectors are given by

$$\hat{r} = \cos \varphi \sin \theta \hat{x} + \sin \varphi \sin \theta \hat{y} + \cos \theta \hat{z} \quad (\text{C.6})$$

$$\hat{\theta} = \cos \varphi \cos \theta \hat{x} + \sin \varphi \cos \theta \hat{y} - \sin \theta \hat{z} \quad (\text{C.7})$$

$$\hat{\varphi} = -\sin \varphi \hat{x} + \cos \varphi \hat{y} \quad (\text{C.8})$$

Appendix D

Edge Detection

The 3D model is represented by meshes of triangles. These triangles need not be connected. This causes the process of detecting edges more difficult.

The algorithm of detecting edges in a mesh is divided into four stages [45]

1. Extract the mesh's triangles.
2. For each edge found in the triangles, extract the triangles where it resides.
3. Calculate a weight for each edge.
4. Apply a filtration strategy to extract feature edges using the weights calculated.

The feature edges are the actual edges in the 3D model.

Calculating Weights

One possible strategy for calculating a weight to represent each edge is to calculate the largest angle between two triangles attached to it. If the edge has only one triangle attached, then it is definitely an edge. A large constant is then assigned as a weight to it.

Feature Edges Extraction

The filtration strategy is defined using a hysteresis function. Two thresholds are used as an upper and lower bounds of the hysteresis. If the weight of the edge is greater than the upper threshold, then the edges is directly declared a feature edge. If the weight of the edge is lower than the lower threshold, then the edge is discarded. Values between the upper and lower bounds are treated in a different manner. An edge with a weight lying in the middle region is declared a feature edge, only if it neighbors another feature edge.

An advantage in this filtration strategy is that it is generic; any thresholds can be set to allow different degrees of freedom in the selection of edges.

Appendix E

Diffraction Around a Cylinder

At first, the two tangent points of the incident ray to the cylinder body are calculated. A tangent point is located by projecting the cylinder on the X-Y plane, finding a tangent point there, and projecting the tangent point back on the plane of incidence.

Tangent points are found as follows:

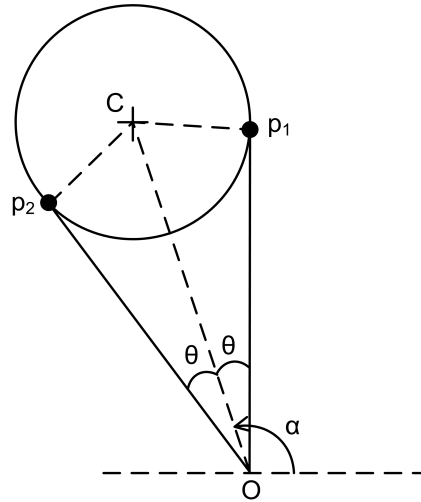


Figure E.1: Tangent points off a circle from an exterior point.

$$\hat{d} = \frac{C - O}{|C - O|}$$

$$l = |C - O|$$

$$\begin{aligned}
\alpha &= \tan^{-1} \frac{d.x}{d.y} \\
t &= \sqrt{l^2 + r^2} \\
\theta &= \sin^{-1} \frac{r}{l} \\
\theta_{1,2} &= \alpha \mp \theta \\
\hat{d}_{1,2} &= \langle \cos \theta_{1,2}, \sin \theta_{1,2}, 0 \rangle \\
p_{1,2} &= O + t * \hat{d}_{1,2}
\end{aligned}$$

The two points are then projected back on the incident plane. The incident plane is defined by the ray origin O , and a normal vector n as follows:

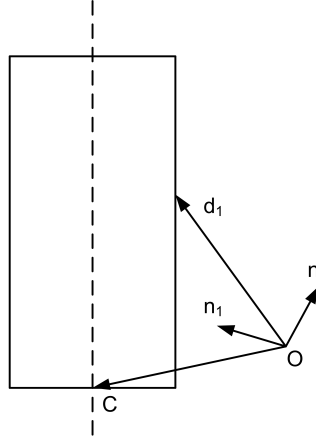


Figure E.2: Plane of incidence is defined by O and n .

$$\begin{aligned}
\hat{d}_2 &= \frac{C - O}{|C - O|} \\
\hat{n} &= \frac{\hat{d}_1 \times (\hat{d}_1 \times \hat{d}_2)}{|\hat{d}_1 \times (\hat{d}_1 \times \hat{d}_2)|}
\end{aligned}$$

After finding the two tangent points, two rays are casted from the incident ray origin, and towards the environment model, passing by each tangent point. The intersection between those two rays and the environment model are then calculated, and the shadow region is defined.

The shadow region is then sampled, and the previous routine is applied on each sampling point to find its corresponding tangent point on the surface of the cylinder, and the detachment point of the diffracted ray is located.

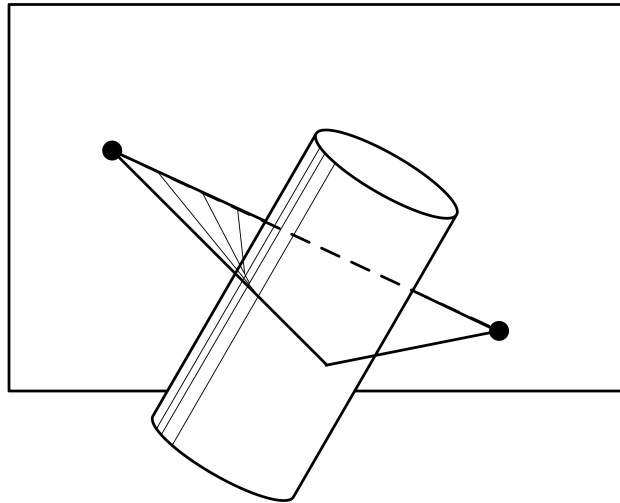


Figure E.3: Sampling the shadow region.

Appendix F

Sampling of Signal Strength

In order to draw the power map over the simulation floor, we need to compute the received power level at every single location of the floor. To do that, we create a data grid (something like the `datagrid` command in MATLAB), and fill each cell with the corresponding power level.

In this chapter, we are going to address how the sampling grid is created and interpolated across the floor area.

F.1 Sampling Grid

To sample the signal power level P_r (dBm) across the floor, we create a sampling grid. The sampling grid basically constitutes of a 2-D matrix, where each cell stores $P_r(x, y)$ – the received power level at x, y location of the floor.

To populate the grid, a canonical receiver (receiver with a default isotropic antenna) is placed at each cell location. A reception sphere is created and centered at each receiver, and the traced rays are received accordingly.

Sampling cells are separated by a fixed step in both directions. The step is calculated from the input resolution.

Note that locations outside the floor can be ignored in order to reduce the number of sampling points. A point-in-polygon check can be done on each point, provided a collision map is available. Otherwise, a ray-plane intersection with each triangle of the model floor can be performed.

Figure F.1 illustrates a sampled floor area.

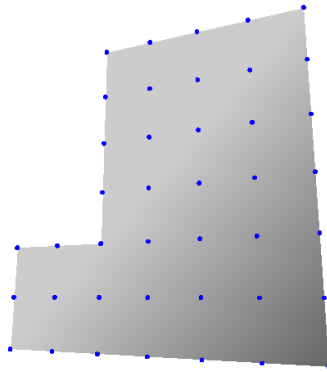


Figure F.1: Sampling Grid of A Sample Floor Area.

F.2 Interpolating Across the Floor Area

In OpenGL, device coordinates are all normalized [46]. They are then transformed and scaled by the viewport into window coordinates. To see how that is really beneficial, consider a model with coordinates of differing values; say one side is measured in meters, while another is in centimeters. OpenGL lets you specify your geometry with coordinates of differing values. OpenGL's ModelView matrix can then scale these different coordinate systems into the same eye coordinate space [46].

Figure F.2 illustrates the process of coloring the floor area.

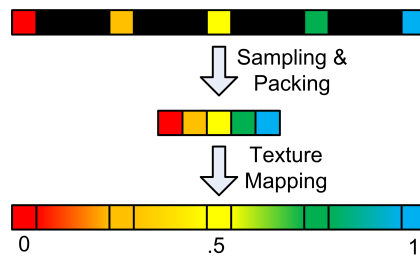


Figure F.2: Sampling, Packing, and Texture Mapping.

At first, the area is sampled using a fixed step, and sampling points are packed into an image of N pixels, where N is the number of sampling instances. The packed image is then used to texture the original area by texture mapping, and the separation steps are colored implicitly in the texturing process using bilinear image interpolation techniques.

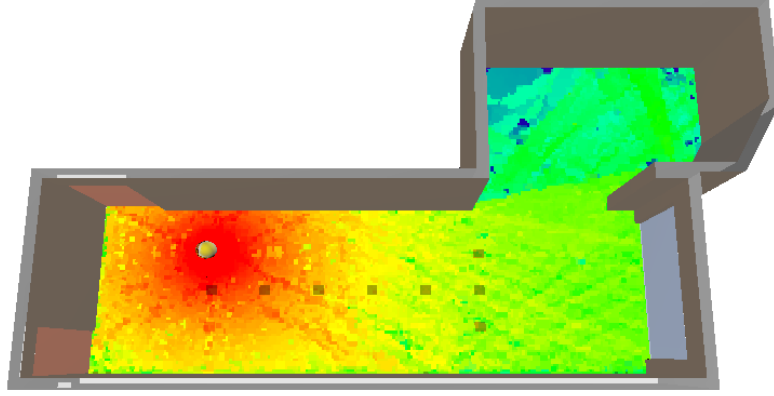


Figure F.3: A Floor Model after Sampling.

The no. of sampling instances N is calculated from:

$$N = S * W * H \quad (\text{F.1})$$

Where W and H are the width and height of the floor area, respectively. The term S is the sampling step, which is calculated from:

$$S = \frac{1}{R} \quad (\text{F.2})$$

Where R is the sampling resolution (input from the user).

For each vertex V of the floor, texture coordinates are calculated from:

$$T(x, y) = \left(\frac{V_x}{W}, \frac{V_y}{H} \right) \quad (\text{F.3})$$

Where V_x and V_y are the X, Y coordinates of the vertex.

An example of the final sampling result is shown in Figure F.3.

Bibliography

- [1] M. Youssef, M. Mah, and A. Agrawala, “Challenges: Device-free Passive Localization for Wireless Environments,” in *MobiCom '07: Proceedings of the 13th annual ACM international conference on Mobile computing and networking*. ACM, 2007, pp. 222–229. 1.1, 1.3, 2.2, 3.4.3, 1, 2
- [2] P. Enge and P. Misra, “Special Issue on Global Positioning System,” in *Proceedings of the IEEE*, January 1999, pp. 3–172. 1.2, 2.1.2
- [3] R. Want, A. Hopper, V. Falcao, and J. Gibbons, “The Active Badge Location System.” *ACM Trans. Inf. Syst.*, vol. 10, no. 1, pp. 91–102, 1992. 1.2, 2.1.2
- [4] M. A. Youssef and A. Agrawala, “The Horus WLAN Location Determination System,” in *Communication Networks and Distributed Systems Modeling and Simulation Conference*, 2005, pp. 205–218. 1.2, 2.1.2, 3.2, 8.3
- [5] M. Barahim, M. Doomun, and N. Joomun, “Low-cost bluetooth mobile positioning for location-based application,” in *Internet, 2007. ICI 2007. 3rd IEEE/IFIP International Conference in Central Asia on*, Sept. 2007, pp. 1–4. 1.2, 2.1.2
- [6] Y. Zhao, “Mobile phone location determination and its impact on intelligent transportation systems,” *Intelligent Transportation Systems, IEEE Transactions on*, vol. 1, no. 1, pp. 55–64, Mar 2000. 1.2, 2.1.2
- [7] S. S. Ram, Y. Li, A. Lin, and H. Ling, “Human Tracking Using Doppler Processing and Spatial Beamforming.” IEEE 2007 Radar Conference, 2007. 1.2, 2.1.1, 2.1.3
- [8] J. Krumm, S. Harris, B. Meyers, B. L. Brumitt, M. Hale, and S. A. Shafer, “Multi-Camera Multi-Person Tracking for Easyliving,” in *Proceedings of the Third IEEE International Workshop on Visual Surveillance*, 2000, pp. 3–10. 1.2, 2.1.3

- [9] R. J. Orr and G. D. Abowd, "The Smart Floor: A Mechanism for Natural User Identification and Tracking," in *Proceedings of ACM CHI 2000 Conference on Human Factors in Computing Systems*, ser. Short talks: multimodal interaction, vol. 2, 2000, pp. 275–276. 1.2, 2.1.3
- [10] K. Kaemarungsi and P. Krishnamurthy, "Modeling of indoor positioning systems based on location fingerprinting," in *INFOCOM 2004. Twenty-third Annual Joint Conference of the IEEE Computer and Communications Societies*, vol. 2, March 2004, pp. 1012–1022 vol.2. 2.1.1
- [11] M. Youssef and A. Agrawala, "Small-scale Compensation for WLAN Location Determination Systems," in *WCNC 2003*, vol. 3, 2003, pp. 1974–1978. 2.1.1, 3.2
- [12] N. B. Priyantha, A. Chakraborty, and H. Balakrishnan, "The Cricket Location-Support System," in *MobiCom '00: Proceedings of the 6th annual international conference on Mobile computing and networking*. New York, NY, USA: ACM Press, 2000, pp. 32–43. 2.1.2
- [13] J. Wilson and N. Patwari, "Radio Tomographic Imaging with Wireless Networks." 2.1.3
- [14] L. Nagy and L. Farkas, "Indoor base station location optimization using genetic algorithms," in *Personal, Indoor and Mobile Radio Communications, 2000. PIMRC 2000. The 11th IEEE International Symposium on*, vol. 2, 2000, pp. 843–846 vol.2. 2.3.1
- [15] A. Hills, "Large-scale wireless lan design," *Communications Magazine, IEEE*, vol. 39, no. 11, pp. 98–107, Nov 2001. 2.3.1
- [16] M. Wright, "Optimization methods for base station placement in wireless applications," in *Vehicular Technology Conference, 1998. VTC 98. 48th IEEE*, vol. 1, May 1998, pp. 387–391 vol.1. 2.3.1
- [17] M. Kamenetsky and M. Unbehaun, "Coverage planning for outdoor wireless lan systems," in *Broadband Communications, 2002. Access, Transmission, Networking. 2002 International Zurich Seminar on*, 2002, pp. 49–1–49–6. 2.3.1
- [18] A. Molina, G. Athanasiadou, and A. Nix, "The automatic location of base-stations for optimised cellular coverage: a new combinatorial approach," in *Vehicular Technology Conference, 1999 IEEE 49th*, vol. 1, Jul 1999, pp. 606–610 vol.1. 2.3.1

- [19] Y. Chen and H. Kobayashi, "Signal strength based indoor geolocation," in *Communications, 2002. ICC 2002. IEEE International Conference on*, vol. 1, 2002, pp. 436–439. 2.3.2
- [20] R. Battiti, M. Brunato, and A. Delai, "Optimal wireless access point placement for location-dependent services," Tech. Rep., 2003. 2.3.2
- [21] S. T.K., Z. Ji, K. Kim, M. A., and S.-P. M., "A Survey of Various Propagation Model for Mobile Communication," in *IEEE Antennas and Propagation Magazine*, vol. 45, 2003, pp. 52–82. 2.4, 6.3, 6.3
- [22] P. Bahl and V. N. Padmanabhan, "RADAR: An In-Building RF-based User Location and Tracking System," in *IEEE INFOCOM 2000*, vol. 2. IEEE, March 2000, pp. 775–784. 3.2
- [23] B. W. Silverman, *Density Estimation for Statistics and Data Analysis*. Chapman & Hall/CRC, April 1986. 3.3.2, 3.3.2
- [24] R. R. Bouckaert, "Choosing between Two Learning Algorithms Based on Calibrated Tests," in *ICML03*. Morgan Kaufmann, 2003, pp. 51–58. 3.4.3
- [25] R. R. Bouckaert and E. Frank, "Evaluating the Replicability of Significance Tests for Comparing Learning Algorithms," in *PAKDD*. Springer, 2004, pp. 3–12. 3.4.3
- [26] Balanis and C. A., *Antenna Theory: Analysis and Design*. Wiley, 1996. 6.2.1, 6.2.1, 6.2.2, 6.2.2, 7.1.4
- [27] D. A. McNamara, C. W. I. Pistorius, and J. A. G. Malherbe, *Introduction to the Uniform Geometrical Theory of Diffraction (Artech House Microwave Library (Hardcover))*. Artech House Publishers. [Online]. Available: <http://www.worldcat.org/isbn/089006301X> 6.2.1, 6.2.1, 7.2.2, 7.2.3, 7.2.4, 7.2.5, 8.1.3, 8.2.1, 8.3.1, 8.3.1, 8.3.2, 8.3.2, 8.3.2, 8.3.2, 8.3.2, 8.3.2
- [28] P. K. Pathak, Y. T. Lo, and S. W. lee, *Techniques for High-Frequency Problems*. Van Nostrand Reinhold Company, 1988, ch. 5. 6.2.2, 8.1, 8.1.3
- [29] W. L. Stutzman and G. A. Thiele, *Antenna Theory and Design*, 2nd ed. John Wiley and Sons, 1998. 2

- [30] D. G., P. N., and R. T. S., “An Advanced 3d Ray Launching Method for Wireless Propagation Prediction,” in *IEEE Vehicular Technology Conference 47th*, 1997. 6.4, 6.4, 6.4, 6.4, 6.5
- [31] Y. Wang, “Site-Specific Modeling of Indoor Radio Wave Propagation,” Ph.D. dissertation, Waterloo, Ontario, Canada, 2000. 6.4, 8.2.1
- [32] S. Seidel and T. Rappaport, “Site-Specific Propagation Prediction for Wireless In-Building Personal Communication System Design,” in *IEEE Trans. Vehicular Technology*, vol. 43, no. 4, 1994, pp. 879–891. 6.5, 7.1.1, 7.1.3, 7.1.3
- [33] Parsons and J. D., *The Mobile Radio Propagation Channel*. Wiley and Sons, 2000. 7.1.1
- [34] M. Born and E. Wolf, *Principles of Optics: Electromagnetic Theory of Propagation, Interference and Diffraction of Light (7th Edition)*, 7th ed. Cambridge University Press, 1999. 7.1.1, 7.1.1, 7.2.5
- [35] G. Perkins and D. Souvaine, “Efficient Radio Wave Front Propagation for Wireless Radio Signal Prediction,” DIMACS, Tech. Rep., 1999. 7.1.2
- [36] T. K. Sarkar, Z. Ji, K. Kim, A. Medouri, and M. Salazar-Palma, “A Survey of Various Propagation Models for Mobile Communication,” in *IEEE Antennas and Propagation Magazine*, vol. 45, no. 3. Syracuse University, 2003. 7.1.3
- [37] Osburn and J. D., “Emc Antenna Parameters and Their Relationships,” Online. [Online]. Available: <http://65.36.174.210/ArchivedArticles/Antennas/I96art24.htm> 7.2.1
- [38] Poggio, J. G. Burke, and A. J., “Numerical Electromagnetic Code (nec) - Method of Moments Parts i, ii and iii,” Lawrence Livermore National Laboratory, Tech. Rep., 1981. 8.1.1
- [39] Cox and J. W. R., “Comparison of Predicted Aircraft Wire Antenna terminal Impedance (using NEC) with Measurement in the HF Band,” in *IEEE Conference on Antennas and Propagation*, vol. 2, 1991, pp. 717–720. 8.1.1
- [40] A. Taflov and S. C. Hagness, *Computational Electrodynamics: The Finite-difference Time-domain Method*, 2nd ed. Artech House, 2000. 8.1.2

- [41] M. Xu, P. Thulasiraman, and R. K. Thulasiram, “Cell Processing for Two Scientific Kernels,” Online, 2008. 8.1.3
- [42] M. Ghaddar, L. Talbi, T. Denid, and A. Charbonneau, “Modeling Human Body Effects for Indoor Radio Channel using UTD.” IEEE, 2004. 8.3
- [43] P. P.H, B. W.D, and M. R.J., “A Uniform Gtd Analysis of the Diffraction of Electromagnetic waves by a Smooth Convex Surface,” in *IEEE Trans. Antennas Propagat*, vol. AP-28. IEEE, 1980, pp. 631–642. 8.3.2, 8.3.2, 8.3.2, 8.3.2, 8.3.2, 8.3.3, 8.3.3, 8.3.3, 8.3.3
- [44] W. Burnside, R. Marhefka, and N. Wang, “Computer Programs, Subroutines and Functions for the Short Course on the Modern Geometrical Theory of Diffraction.” Ohio State University. 8.3.2
- [45] H. A., M. K., and G. M., “Mesh Edge Detection,” Swiss Federal Institute of Technology, Tech. Rep. 351, 2000. D
- [46] “Opengl Faq / 9 Transformations,” Online, 2006. [Online]. Available: <http://www.opengl.org/resources/faq/technical/transformations.htm> F.2